Targeting the mitochondrial lysophosphatidic acid-producing enzyme glycerol-3-phosphate acyltransferase 1 in ovarian cancer using a stable knockdown system and the small molecule inhibitor FSG67

Dissertation

zur Erlangung des akademischen Grades des Doktors der Naturwissenschaften (Dr. rer. nat.) an der Fakultät für Chemie und Chemische Biologie der Technischen Universität Dortmund

vorgelegt von

Manuel Alvarez de las Heras (M.Sc.)

Dortmund 2026

1. Gutachter: Prof. Dr. Jan G. Hengstler

2. Gutachter: Prof. Dr. Christoph van Thriel

Veröffentlicht als Dissertationsschrift zur Erlangung des akademischen Grades des Doktors der Naturwissenschaften (Dr. rer. nat.) an der Fakultät für Chemie und Chemische Biologie der Technischen Universität Dortmund

Promotionsort und Jahr: Dortmund 2026

Abstract

Ovarian cancer is one of the most commonly detected cancers in women. The lack of efficient screening methods complicates early disease detection and thus ovarian cancer is often diagnosed at later stages when more severe symptoms due to metastasis are present and the five-year relative survival rate is only 29%. Recently lysophosphatidic acid (LPA) was reported to play an important role in different diseases, including ovarian cancer. So far, mainly the role of extracellular LPA as a signaling lipid has been studied; however, LPA is also produced intracellularly, and as opposed to extracellular LPA, little is known of its role as a signaling lipid. Intracellular LPA can be produced by several metabolic pathways and enzymes, including the glycerol-3-phosphate acyltransferase (GPAT) enzymes. The glycerol-3-phosphate acyltransferase 1, mitochondrial (GPAM) has been linked to several diseases, including metabolic disorders and cancer. For example, GPAM expression was associated with worse outcome in human ovarian cancer patients, and its silencing reduced tumor growth in a subcutaneous xenograft mouse model. However, the contribution of GPAM to ovarian cancer metastasis has not yet been studied in vivo. Thus, in this PhD thesis, the effect of silencing GPAM with a stable knockdown system, appropriate for in vivo studies, as well as pharmacologically inhibiting its enzymatic activity with the small molecule inhibitor FSG67 was evaluated both in vitro and in vivo.

Luciferase-expressing ES-2 ovarian cancer cell lines were generated to be used for in vivo imaging of peritoneal metastasis. The most promising luciferase-expressing ovarian cancer cell line was then chosen to generate stable GPAM knockdown cell lines, suitable for in vivo studies. The stable GPAM knockdown was first evaluated in vitro, revealing that silencing GPAM decreased collective cell migration and the number of colonies formed, but had no effect on colony size nor anoikis resistance, and did not strongly influence individual cell migration. In a subsequent experiment using an in vivo model of peritoneal metastasis, stable GPAM knockdown in ES-2 cells slowed tumor growth suggesting a possible role for GPAM in ovarian cancer metastasis. Moreover, the effect of inhibiting GPAM with the small molecule GPAT inhibitor FSG67 was also evaluated, demonstrating that FSG67 altered the formation of colonies and reduced individual cell migration, collective cell migration and resistance to anoikis in ovarian cancer cells. Additionally, toxicology and pharmacokinetic studies of FSG67 in vivo revealed the compound to be suitable for future in vivo studies, such as antitumor efficacy studies of the compound.

To gain further insight into the mechanism behind GPAM's role in the observed cancer cell phenotypes, its enzymatic product, LPA was studied as a possible autocrine and/or paracrine signaling molecule using mass spectrometry-based measurements of labeled LPA, demonstrating that intracellular LPA was not transported into the extracellular space. In addition, intracellular binding partners of LPA were evaluated on the protein level. Therefore, an LPA-protein pull-down assay was established and subsequently used with sequential window acquisition of all theoretical fragment ion mass spectra (SWATH-MS) based proteomics, identifying S100 calcium-binding protein A7 (S100A7), BPI fold-containing family B member 1 (BPIFB1), suprabasin (SBSN) and actin (ACTB/ACTG) as intracellular LPA-binding protein candidates.

In summary, this work shows that silencing GPAM or inhibiting GPAM with FSG67 hinders cancer-relevant processes and that both approaches are suitable for in vivo studies of ovarian cancer metastasis. Furthermore, it identified intracellular LPA-binding protein candidates to be followed up in future studies.

Zusammenfassung

Das Ovarialkarzinom gehört zu den am häufigsten diagnostizierten Arten von Krebserkrankungen bei Frauen. Das Fehlen effizienter Screening-Methoden erschwert die frühe Diagnose der Erkrankung, daher wird das Ovarialkarzinom häufig erst in späteren Stadien diagnostiziert, wenn es bereits durch Metastasierung zu schwereren Symptomen geführt hat und die relative Fünf-Jahres-Überlebensrate nur noch 29% beträgt. Kürzlich wurde gezeigt, dass die Lysophosphatidsäure (LPA) eine wichtige Rolle bei verschiedenen Erkrankungen spielt, so auch beim Ovarialkarzinom. Bisher wurde vor allem die Rolle von extrazellulärem LPA als Signallipid untersucht; allerdings wird LPA auch intrazellulär produziert. Im Gegensatz zum extrazellulären LPA ist wenig über die Rolle von intrazellulärem LPA als Signallipid bekannt. Intrazelluläres LPA kann durch verschiedene Stoffwechselwege und Enzyme produziert werden, einschließlich der Glycerol-3-phosphat-Acyltransferasen (GPAT). Das mitochondriale Enzym Glycerol-3-phosphat-Acyltransferase 1 (GPAM) wurde mit mehreren Erkrankungen in Verbindung gebracht, darunter Stoffwechselstörungen und Krebserkrankungen. Beispielsweise war die Expression von GPAM bei Patientinnen mit humanem Ovarialkarzinom mit einem schlechteren Outcome assoziiert, und GPAM-Silencing reduzierte das Tumorwachstum in einem subkutanen Xenograft-Mausmodell. Allerdings wurde der Einfluss von GPAM auf die Metastasierung des Ovarialkarzinoms bisher noch nicht in vivo untersucht. Daher wurden in dieser Dissertation der Effekt des GPAM-Silencings mithilfe eines stabilen Knockdown-Systems, das für In-vivo-Studien geeignet ist, sowie die pharmakologische Inhibierung seiner Enzymaktivität durch den kleinmolekularen Inhibitor FSG67 sowohl in vitro als auch in vivo evaluiert.

Es wurden Luciferase-exprimierende ES-2 Ovarialkarzinom-Zelllinien für die In-vivo-Bildgebung von Peritonealmetastasen generiert. Dann wurde die vielversprechendste Luciferase-exprimierende Ovarialkarzinom-Zelllinie ausgewählt, um stabile GPAM-Knockdown-Zelllinien zu generieren, die für In-vivo-Studien geeignet sind. Der stabile GPAM-Knockdown wurde zunächst in vitro untersucht, wobei sich zeigte, dass das Silencing von GPAM die kollektive Zellmigration und die Anzahl der entstandenen Kolonien reduzierte, aber weder die Koloniegröße noch die Anoikis-Resistenz beeinflusste und auch keinen starken Einfluss auf die individuelle Zellmigration hatte. In einem nachfolgenden Experiment mit einem In-vivo-Modell für Peritonealmetastasen verlangsamte der stabile GPAM-Knockdown in ES-2-Zellen das Tumorwachstum, was auf eine mögliche Rolle von GPAM bei der Metastasierung des Ovarialkarzinoms hindeutet. Weiterhin wurde der Effekt der Inhibierung von

GPAM mit dem kleinmolekularen GPAT-Inhibitor FSG67 untersucht, wobei gezeigt wurde, dass FSG67 die Entstehung von Kolonien beeinflusste und die individuelle Zellmigration, die kollektive Zellmigration sowie die Anoikis-Resistenz von Ovarialkarzinom-Zellen reduzierte. Darüber hinaus zeigten toxikologische und pharmakokinetische Studien von FSG67 in vivo, dass die Substanz für zukünftige In-vivo-Studien, wie etwa zur Antitumorwirksamkeit, geeignet ist.

Um einen genaueren Einblick in den Mechanismus hinter der Rolle von GPAM bei den beobachteten Krebszell-Phänotypen zu gewinnen, wurde sein enzymatisches Produkt LPA als potenzielles autokrines und/oder parakrines Signalmolekül untersucht. Mittels Massenspektrometrie-basierter Messungen von markiertem LPA konnte gezeigt werden, dass intrazelluläres LPA nicht in den extrazellulären Raum transportiert wurde. Zusätzlich wurden die intrazellulären Bindungspartner von LPA auf Proteinebene untersucht. Dafür wurde ein LPA-Protein-Pull-Down-Assay etabliert und anschließend in Kombination mit „sequential window acquisition of all theoretical fragment ion mass spectra“ (SWATH-MS)-basierter Proteomik genutzt. Dabei ließen sich „S100 calcium-binding protein A7“ (S100A7), „BPI fold-containing family B member 1“ (BPIFB1), „suprabasin“ (SBSN) und Aktin (ACTB/ACTG) als potenzielle intrazelluläre LPA-Bindungspartner identifizieren.

Zusammenfassend zeigt diese Arbeit, dass sowohl das Silencing von GPAM als auch die Inhibierung von GPAM mittels FSG67 krebsrelevante Prozesse beeinträchtigen und dass beide Ansätze für In-vivo-Studien zur Metastasierung des Ovarialkarzinoms geeignet sind. Weiterhin wurden in dieser Arbeit potenzielle intrazelluläre LPA-Bindungspartner identifiziert, die in zukünftigen Studien weiterverfolgt werden sollen.

Eidesstattliche Versicherung (Affidavit)

Name, Vorname
(Surname, first name)

Matrikel-Nr.
(Enrolment number)

Belehrung:

Wer vorsätzlich gegen eine die Täuschung über Prüfungsleistungen betreffende Regelung einer Hochschulprüfungsordnung verstößt, handelt ordnungswidrig. Die Ordnungswidrigkeit kann mit einer Geldbuße von bis zu 50.000,00 € geahndet werden. Zuständige Verwaltungsbehörde für die Verfolgung und Ahndung von Ordnungswidrigkeiten ist der Kanzler/die Kanzlerin der Technischen Universität Dortmund. Im Falle eines mehrfachen oder sonstigen schwerwiegenden Täuschungsversuches kann der Prüfling zudem exmatrikuliert werden, § 63 Abs. 5 Hochschulgesetz NRW.

Die Abgabe einer falschen Versicherung an Eides statt ist strafbar.

Wer vorsätzlich eine falsche Versicherung an Eides statt abgibt, kann mit einer Freiheitsstrafe bis zu drei Jahren oder mit Geldstrafe bestraft werden, § 156 StGB. Die fahrlässige Abgabe einer falschen Versicherung an Eides statt kann mit einer Freiheitsstrafe bis zu einem Jahr oder Geldstrafe bestraft werden, § 161 StGB.

Die oben stehende Belehrung habe ich zur Kenntnis genommen:

Official notification:

Any person who intentionally breaches any regulation of university examination regulations relating to deception in examination performance is acting improperly. This offence can be punished with a fine of up to EUR 50,000.00. The competent administrative authority for the pursuit and prosecution of offences of this type is the chancellor of the TU Dortmund University. In the case of multiple or other serious attempts at deception, the candidate can also be unenrolled, Section 63, paragraph 5 of the Universities Act of North Rhine-Westphalia.

The submission of a false affidavit is punishable.

Any person who intentionally submits a false affidavit can be punished with a prison sentence of up to three years or a fine, Section 156 of the Criminal Code. The negligent submission of a false affidavit can be punished with a prison sentence of up to one year or a fine, Section 161 of the Criminal Code.

I have taken note of the above official notification.

Ort, Datum
(Place, date)

Unterschrift
(Signature)

Titel der Dissertation:
(Title of the thesis):

Ich versichere hiermit an Eides statt, dass ich die vorliegende Dissertation mit dem Titel selbstständig und ohne unzulässige fremde Hilfe angefertigt habe. Ich habe keine anderen als die angegebenen Quellen und Hilfsmittel benutzt sowie wörtliche und sinngemäße Zitate kenntlich gemacht.
Die Arbeit hat in gegenwärtiger oder in einer anderen Fassung weder der TU Dortmund noch einer anderen Hochschule im Zusammenhang mit einer staatlichen oder akademischen Prüfung vorgelegen.

I hereby swear that I have completed the present dissertation independently and without inadmissible external support. I have not used any sources or tools other than those indicated and have identified literal and analogous quotations.

The thesis in its current version or another version has not been presented to the TU Dortmund University or another university in connection with a state or academic examination.*

*Please be aware that solely the German version of the affidavit ("Eidesstattliche Versicherung") for the PhD thesis is the official and legally binding version.

Ort, Datum
(Place, date)

Unterschrift
(Signature)

Acknowledgements

I wish to show my sincere gratitude to all people who contributed in the present work. Without them, you could not read this document, as you are doing at this moment.

I am grateful to Prof. Dr. Jan G. Hengstler for giving to me the opportunity of belonging to the Toxicology Department as well as for his suggestions to guide this work. My special gratitude goes to Dr. Rosemarie Marchan and Dr. Karolina Edlund for their experience, advice and support. Without their help, this study would not have been realized. I will be always grateful with them for sharing their insight with me.

Moreover, I thank all the members of the Cell Metabolism group, the Bioanalytics department, as well as other researchers who provided their experience, time and other resources to complete this work.

And finally, I would like to thank my family and friends who always believed in me.

Table of contents

List of figures

List of tables

Abbreviations

AGK	acylglycerol kinase
AGPAT	acylglycerol-3-phosphate acyltransferase
ATX	autotaxin
BCA	bicinchoninic acid
bLOD	below limit of detection
BPIFB1	BPI fold-containing family B member 1
BSA	bovine serum albumin
CARS	coherent anti-Stokes Raman scattering
CCOC	clear cell ovarian cancer
cDNA	complementary DNA
CDX	cell line-derived xenograft
CHO	Chinese hamster ovary
DAG	diacylglycerol
DAGK	diacylglycerol kinase
DAGT	diacylglycerol acyltransferase
dLPA	1-palmitoyl-d_9 lysophosphatidic acid
EMT	epithelial-to-mesenchymal transition
ENOC	endometrioid ovarian cancer
ESI	electrospray ionization
FASP	filter aided sample preparation
FIGO	Fédération Internationale de Gynécologie et d'Obstétrique
FM	full medium
G3P	glycerol-3-phosphate
GPAM	glycerol-3-phosphate acyltransferase 1, mitochondrial
GPAT	glycerol-3-phosphate acyltransferase
GPCR	G protein-coupled receptor
HGSOC	high-grade serous ovarian cancer
HRP	horseradish peroxidase
IC	inhibitory concentration
IP	intraperitoneal, intraperitoneally
LC	liquid chromatography
LGSOC	low-grade serous ovarian cancer

LPA	lysophosphatidic acid
LPAR	lysophosphatidic acid receptor
MAG	monoacylglycerol
MALFD	metabolic dysfunction-associated fatty liver disease
MASH	metabolic dysfunction-associated steatohepatitis
MOC	mucinous ovarian cancer
MOI	multiplicity of infection
MRM	multiple reaction monitoring
MS	mass spectrometry
MTD	maximum tolerated dose
PA	phosphatidic acid
PAGE	polyacrylamide gel electrophoresis
PARP	poly(ADP-ribose) polymerase
PEG	polyethylene glycol
pHEMA	poly(2-hydroxyethyl methacrylate)
PI3K	phosphatidylinositol 3-kinase
PL	phospholipase
PPAR	peroxisome proliferator-activated receptor
qRT-PCR	quantitative real time-polymerase chain reaction
RDT	repeated dose toxicity
RIPA	radioimmunoprecipitation assay
SBSN	suprabasin
SDS	sodium dodecyl sulfate
shRNA	short harpin RNA
SWATH-MS	sequential window acquisition of all theoretical fragment ion mass spectra
TAG	triacylglycerol
VEGF	vascular endothelial growth factor

1 Introduction

1.1 Ovarian cancer

Ovarian cancer is one of the most common types of cancers among women, being the seventh most detected cancer in the female population (Reid, Permuth, and Sellers 2017). A woman has a 1 in 75 probability of developing ovarian cancer during her lifetime, and a probability of 1 in 100 of dying from this disease (Reid, Permuth, and Sellers 2017). This cancer type normally presents with severe symptoms at later stages of the disease, in which the five-year relative survival rate is just 29% (Reid, Permuth, and Sellers 2017) and to date there are no established tests to detect the disease before the symptoms appear (Berek et al. 2021).

According to the cell type from which the tumors presumably originate, ovarian cancers can be classified as epithelial, stromal or germ cell derived ovarian cancer (Reid, Permuth, and Sellers 2017). Epithelial ovarian cancer, the predominant type, can be further classified into five histological subtypes which are distinct with regard to the origin of the cancer, risk factors or prognosis. Specifically, these are high-grade serous (HGSOC, 70%), clear cell (CCOC, 10%), endometrioid (ENOC, 10%), mucinous (MOC, 3%), and low-grade serous ovarian cancer (LGSOC, < 5%) (McCluggage 2011). Endometriosis is believed to be one of the precursors of ENOC and CCOC (Banz et al. 2010; Prowse et al. 2006), whereas epithelial cells from the fallopian tubes might be one of the precursors of HGSOC (Gilks et al. 2015; Kindelberger et al. 2007; Labidi-Galy et al. 2017). HGSOC exhibits a high genetic instability due to its high number of accumulated mutations (Haverty et al. 2009; Kuo et al. 2009). Furthermore, ENOC, CCOC, MOC, and LGSOC are believed to progress from tumor of low malignant potential to well-differentiated cancers following specific phases and are classified as Type I (Shih Ie and Kurman 2004). On the other hand, HGSOC are fast growing and metastasizing tumors; and it is classified as Type II (Shih Ie and Kurman 2004). In addition, Type I and II tumors have characteristic mutations that are often present in one type but not the other. For example, Type I LGSOC tumors frequently have mutations in *BRAF* and *KRAS* (70%), Type I MOC tumors have mutations in *KRAS* (> 60%), and *PTEN* is mutated in Type I ENOC tumors (20%); whereas Type II HGSOC tumors usually do not present mutations in these mentioned genes, but instead frequently in *TP53* (50 – 80%) (Shih Ie and Kurman 2004).

Several factors are associated with the risk of developing ovarian cancer. Reproductive and hormonal factors such as parity and oral contraceptives may reduce the probability of devel-

oping ovarian cancer, whereas others such as endometriosis, aging, and obesity may increase the probability (Reid, Permuth, and Sellers 2017). Nevertheless, genetics plays a considerable role in the development of ovarian cancer, for example, immediate family members of probands have three to seven times higher probability of developing ovarian cancer, especially if there are already several cases in the family (Parazzini et al. 1992; Stratton et al. 1998). Moreover, specific mutations in *BRCA1* and *BRCA2* have been related to the development of ovarian cancer (Lynch et al. 2009; Malander et al. 2004).

The spread of the tumoral cells, which is defined as the disease stage, is usually determined by surgery and radiology. The most common staging system for ovarian cancer is the FIGO (Fédération Internationale de Gynécologie et d'Obstétrique, French name for International Federation of Gynecology and Obstetrics) system, for which there are four stages. In Stage I the tumor is confined to the ovaries (one or both of them). In Stage II the tumor is present in the ovaries (one or both of them) and has also invaded the surrounding pelvic organs (below the pelvic brim). In Stage III the tumor is additionally detected outside the pelvis in adjacent organs such as the intestines or diaphragm. Finally, stage IV tumors are those that are additionally found beyond the abdomino-pelvic cavity (Berek et al. 2021).

1.1.1 Metastasis

Metastatic spread in ovarian cancer can occur via the transcoelomic, hematogenous, or lymphogenous route (Figure 1), with the transcoelomic route being the most common (Lengyel 2010). Transcoelomic refers to spread through a cavity in the body, in this case the peritoneal cavity (Lengyel 2010). Before metastasizing, ovarian cancer cells often undergo epithelial-to-mesenchymal transition (EMT), which reduces the intercellular adhesions between the ovarian cancer cells resulting in the characteristic motile and invasive phenotype of mesenchymal cells (Lengyel 2010). An important protein responsible for these adhesions in epithelial cells is E-cadherin (Huber, Kraut, and Beug 2005), which is connected to the actin microfilaments within the cytoplasm via α- and β-catenin, thus anchoring epithelial cells to one another. The loss of E-cadherin in ovarian cancer cells is often related to EMT and the development of the ability of these cells to invade other tissues (Kalluri and Weinberg 2009). Ovarian cancer cells in the peritoneal fluid and metastatic niches have reduced expression of E-cadherin compared to the original tumor; and, ovarian cancer cells with lower E-cadherin levels have a more invasive phenotype (Veatch, Carson, and Ramakrishnan 1994). In contrast, the expression of other cadherins is up-regulated, such as N-cadherin or P-cadherin (Lengyel 2010). This

change in the cadherin expression pattern during EMT is known as the cadherin switch (Assidi 2022).

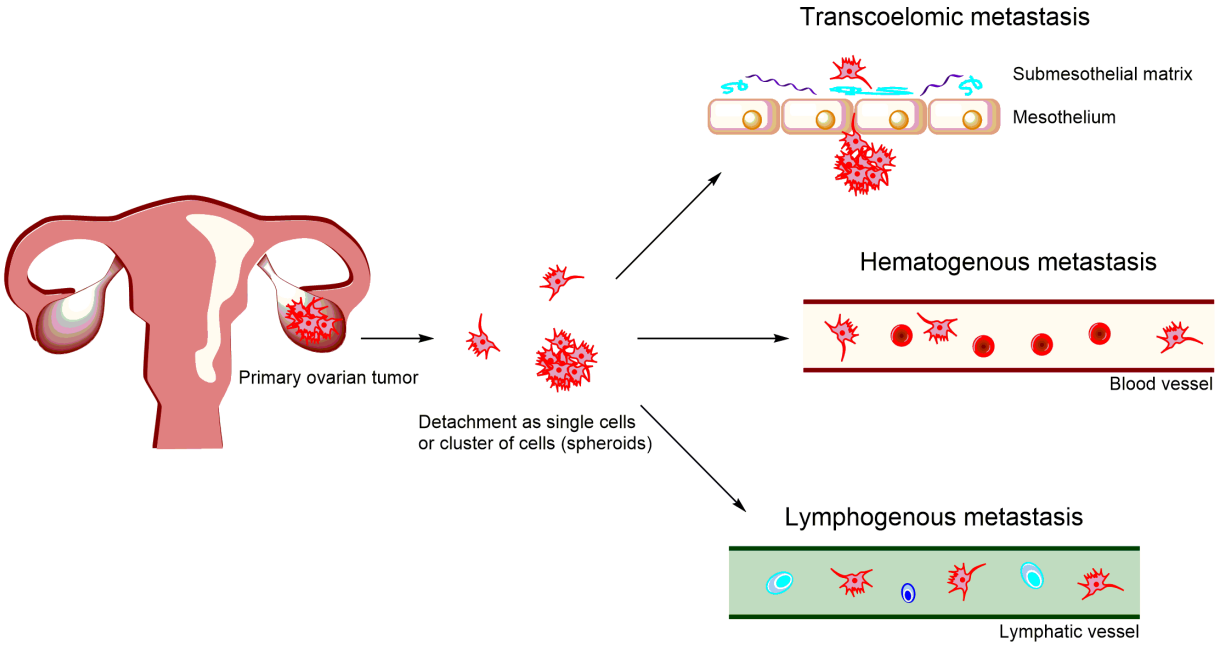

Figure 1 Main routes of ovarian cancer metastasis. Once the ovarian cancer cells detach from the primary ovarian tumor, they may disseminate to other organs crossing the peritoneal cavity across the mesothelium (transcoelomic route), via the circulatory system (hematogenous route) or the lymphatic system (lymphogenous route).

Having reduced their intercellular connections, ovarian cancer cells detach from the primary ovarian tumor and become suspended in the peritoneal fluid as single cells or spheroids (cluster of cells) (Lengyel 2010). It is speculated that the natural movement of the peritoneal fluid helps the separated cells to reach their sites of metastasis (Lengyel 2010). Ascites, the buildup of fluid in the abdomen, is a common symptom of more advanced ovarian cancer (Lengyel 2010), and can develop due to several reasons. For example, ovarian cancer cells can block lymphatic channels in their surroundings, which reduces the absorption of peritoneal fluid and thus increases its volume (Lengyel 2010). Furthermore, the production of vascular endothelial growth factors (VEGFs) by ovarian cancer cells increases the movement of fluid across the blood vessels, which contributes to the development of ascites (Lengyel 2010). Finally, ascites is rich in soluble molecules, for example cytokines, chemokines and growth factors, as well as different types of cells, such as immune, mesothelial, and cancer stem cells (Ahmed and Stenvers 2013). It has thus been proposed that the new niche created by ascites promotes the development of the ovarian cancer metastasis (Kim, Kim, and Song 2016).

The most common site of ovarian cancer metastasis is the peritoneum, more specifically the parietal and visceral peritoneum and omentum (Dvoretsky et al. 1988; Reed et al. 2000). The peritoneum is a membrane that lines the abdominal cavity and is primarily composed of mesothelium, which refers to a monolayer of mesothelial cells attached to a basement membrane (Lengyel 2010). A special part of the peritoneum is the omentum, a layer of fatty tissue that covers the organs in the lower abdomen (Lengyel 2010). When ovarian cancer cells arrive at the site of metastasis, they begin attaching to the mesothelium via membrane receptors that recognize their respective ligands on the cells of the mesothelium to enable adhesion. Examples of interacting receptor:ligand pairs are CA125:mesothelin (Gubbels et al. 2006) and CD44:hyaluronic acid (Cannistra et al. 1993; Strobel, Swanson, and Cannistra 1997). Next, the ovarian cancer cells disrupt the single layer of mesothelial cells and invade the submesothelial matrix, where they adhere preferentially to type I collagen (Moser et al. 1996). Once the cancer cells are implanted at the secondary site, they transform the site of metastasis in order to facilitate their proliferation, for example by promoting the development of new blood vessels to support their growth through the secretion of VEGFs, such as VEGF A, B and C (Lengyel 2010).

1.1.2 Diagnosis and treatment

The stage at which ovarian cancer is diagnosed greatly influences prognosis. For example, if the cancer is detected at Stage II the prognosis is often promising, because a 5-year survival rate of 70% can be reached (Elias, Guo, and Bast 2018). Nevertheless, roughly 70% of epithelial ovarian cancers are first detected at Stage III or IV, when metastasis has already formed (Berek et al. 2021). A major reason why ovarian cancer is often discovered at these late stages is that the symptoms at the initial stages are subtle and easily confused with other less serious diseases, and only at the advanced stages do these symptoms worsen and the disease becomes more evident (Berek et al. 2021). This is often the case for the predominant histological subtype of epithelial ovarian cancer, HGSOC, with an aggressive phenotype and fast metastasis (Berek et al. 2021). Symptoms include mild abdominal discomfort, menstrual irregularities, or digestive alterations (Trimbos et al. 2003; Zanetta et al. 1997). As the disease progresses, the formation of ascites contributes to the development of pain in the abdominal region, as well as respiratory complications (Berek et al. 2021). For diagnosis, radiography should be carried out to determine the spread of the cancer, as well as the analysis of tumor markers in blood including CA125 and carcinoembryonic antigen (Berek et al. 2021). Nevertheless, CA125 blood level is not used to screen for ovarian cancer since it can be increased by other condi-

tions, such as pregnancy or endometriosis (Hu et al. 2019). In contrast, it is often used to monitor the progression of the disease (Hu et al. 2019).

After a positive diagnosis of ovarian cancer, the next step is usually to visually examine the inside of the abdominal cavity and remove tissue or organs for further analysis and determination of the stage of the disease (Berek et al. 2021). Since many of the ovarian cancer patients are in Stage III or IV, typically cytoreductive (debulking) surgery followed by chemotherapy are performed (Berek et al. 2021). For chemotherapy, the standard course of treatment is six cycles of chemotherapy, where a platinum-containing drug (cisplatin or carboplatin) is used in combination with a taxane (docetaxel or paclitaxel). Currently, more patients are being treated with neoadjuvant chemotherapy before the debulking surgery, although there is not a consensus regarding its benefits (Berek et al. 2021). Almost 80% of patients who initially respond to chemotherapy will eventually relapse (Berek et al. 2021), resulting in an increasing use of maintenance therapy with poly(ADP-ribose) polymerase (PARP) inhibitors, even though its benefit is not conclusive (Coleman et al. 2017; Gonzalez-Martin et al. 2019; Moore et al. 2018). Moreover, several studies have shown beneficial results with the addition of the anti-VEGF A antibody bevacizumab to the chemotherapeutical treatments (Berek et al. 2021).

Despite the methodologies explained above for the treatment of ovarian cancer, curing ovarian cancer is still extremely challenging. Chemotherapy is often most effective at the beginning of treatment. Nevertheless, with time chemotherapy becomes less effective, recurrence is more frequent and finally the cancer turns chemoresistant, which makes it incurable (Goldie and Coldman 1979; Matulonis et al. 2016). Evidence suggests that ovarian cancer metastasis contains cancer stem cells, which are chemoresistant and allow the cancer to self-renew (Curley et al. 2011; Zhang et al. 2008). Furthermore, advanced peritoneal metastases may block the intestines of the patient (Gadducci et al. 2001). In summary, the mechanisms underlying ovarian cancer development and metastasis requires further study to find novel treatment targets.

1.1.3 Lysophosphatidic acid in ovarian cancer

In the last decades, the bioactive phospholipid lysophosphatidic acid (LPA) has received increasing attention in ovarian cancer research due to its multiple roles in the disease. For example, some studies reported a high concentration of LPA in the blood plasma and ascites of ovarian cancer patients, independently of the stage of the disease, and thus suggesting that

LPA may be used as a diagnostic tool (Bese et al. 2010; Xu et al. 1998). Nevertheless, to date LPA is not used as a clinical biomarker, although many detection techniques have been developed with great progress in the field (Li, Chen, et al. 2020). Several studies have shown that LPA treatment increased the expression and secretion of interleukin-8, a cytokine present in the ascites of ovarian cancer patients that increases the invasiveness of ovarian cancer cells (Fang et al. 2004; Schwartz et al. 2001; So et al. 2004). Additionally, some studies reported a higher expression of the LPA receptors LPAR2 and LPAR3 in ovarian cancer cells compared to noncancerous ovarian cells (Goetzl et al. 1999; Si et al. 2015), and silencing these receptors decreased cell migration and invasiveness of the ovarian cancer cells (Yu et al. 2008). Furthermore, Mukherjee and coworkers demonstrated that LPA enhanced glycolysis through the induction of hexokinase II, which increased proliferation in ovarian cancer cells (Mukherjee et al. 2015). Another study showed that LPA produced by human peritoneal mesothelial cells increased migration, invasion and adhesion of ovarian cancer cells (Ren et al. 2006). In addition, Hu et al. showed that LPA stimulated the production of the inductors of angiogenesis, VEGFs in ovarian cancer cells, activating the transcription factors c-Jun and c-Fox (Hu et al. 2001). Nevertheless, most of the studies so far investigating LPA and ovarian cancer focused on LPA in the extracellular space, but since LPA is also found in the intracellular space, the role of intracellular LPA in ovarian cancer deserves further attention.

1.2 Lysophosphatidic acid

1.2.1 Lysophosphatidic acid, a family of glycerophospholipids

Lysophosphatidic acid (LPA) is a glycerophospholipid with functions in cellular signaling and as a structural lipid (Yung, Stoddard, and Chun 2014). Importantly, LPA is not a single molecule but rather refers to a family of molecules that all contain a glycerol backbone, hydrocarbon chain and phosphate group (Figure 2). While the latter group is found at position 3 of the glycerol backbone, the hydrocarbon chain can be either at position 1 with an acyl, alkyl or alkenyl linkage, or at position 2 that is acyl-linked (Yung, Stoddard, and Chun 2014). Within the LPA family, the major components are the 1-acyl-2-hydroxy-sn-glycerol-3-phosphate, where the hydrocarbon chain is at position 1 with an acyl linkage, and thus the substituent at position 1 is a fatty acid (Yung, Stoddard, and Chun 2014). The fatty acid chain can vary in length and saturation, having LPA molecules with a saturated fatty acid chain (16:0, 18:0) and with an unsaturated fatty acid chain (16:1, 18:1, 18:2, 20:4) (Yung, Stoddard, and Chun 2014). The fatty acid chain influences the recognition of the specific LPA molecule

by different LPA receptors, and thus the different LPA molecules trigger distinct biological activities (Aikawa et al. 2015; Hayashi et al. 2001). The most studied LPA molecule is oleoyl-LPA (also known as 18:1 LPA; LPA with oleic acid in an acyl linkage at position 1) (Yung, Stoddard, and Chun 2014). LPA is present in all eukaryotic tissues and blood plasma (Moolenaar, van Meeteren, and Giepmans 2004; Tokumura 2004), both intracellularly and extracellularly (Geraldo et al. 2021) and while the role of intracellular LPA is not well understood, most of the literature so far has focused on the role of LPA in the extracellular environment.

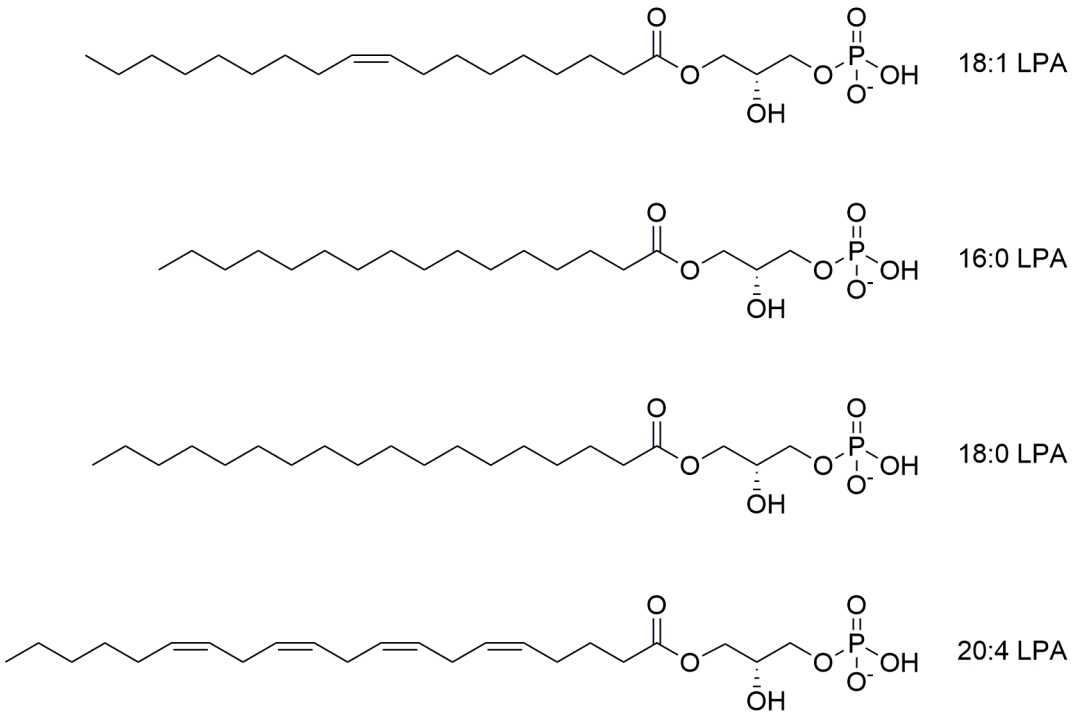

Figure 2 Main LPA molecules. The most abundant LPA molecules of mammals are illustrated above. All contain a saturated or unsaturated fatty acid of different length at position 1 of the glycerol backbone, as well as a phosphate group at position 3.

1.2.2 Extracellular LPA: metabolism and signaling

LPA is found extracellularly in all eukaryotic tissues and fluids, under both physiological and pathological conditions (Geraldo et al. 2021). Examples include neural tissue, saliva, aqueous humor and blood (Choi et al. 2010; Yung, Stoddard, and Chun 2014). Physiological LPA concentrations are also quite broad. For example, LPA concentration in the plasma ranges from 0.7 to 80 nM, while it can be as high as 10 µM in serum (Gustin, Van Steenbrugge, and Raes 2008; Valdés-Rives and González-Arenas 2017).

To date, two main pathways have been identified for the production of extracellular LPA, both of which are based on the degradation of membrane phospholipids (Figure 3). In the first

pathway, phospholipase A1 or phospholipase A2 (PLA_1 or PLA_2) hydrolyzes one of the ester bonds of membrane phospholipids. PLA_1 hydrolyzes the 1-acyl position and thus produces 2-acyl-species, whereas PLA_2 hydrolyzes the 2-acyl position to produce 1-acyl-species. If the substrates for these enzymes are phosphatidylcholine, phosphatidylserine or phosphatidylethanolamine, then lysophosphatidylcholine, lysophosphatidylserine or lysophosphatidylethanolamine are produced, respectively. In the subsequent enzymatic step, autotaxin (ATX), an enzyme with lysophospholipase D activity, removes the phosphate head-group of these lysophospholipids leading to the production of LPA (Yung, Stoddard, and Chun 2014). In the second pathway, phospholipase D removes the phosphate head-group of phospholipids resulting in phosphatidic acid (PA). Then, either PLA_1 or PLA_2 removes one of the fatty acid chains of PA leading to the production of LPA (Aoki, Inoue, and Okudaira 2008). Thus, the substituent at position 1 of LPA can be any of the fatty acids present in mammalian cells, which explains the diversity of the LPA molecule with respect to length and saturation of the hydrocarbon chain (Bandoh et al. 2000).

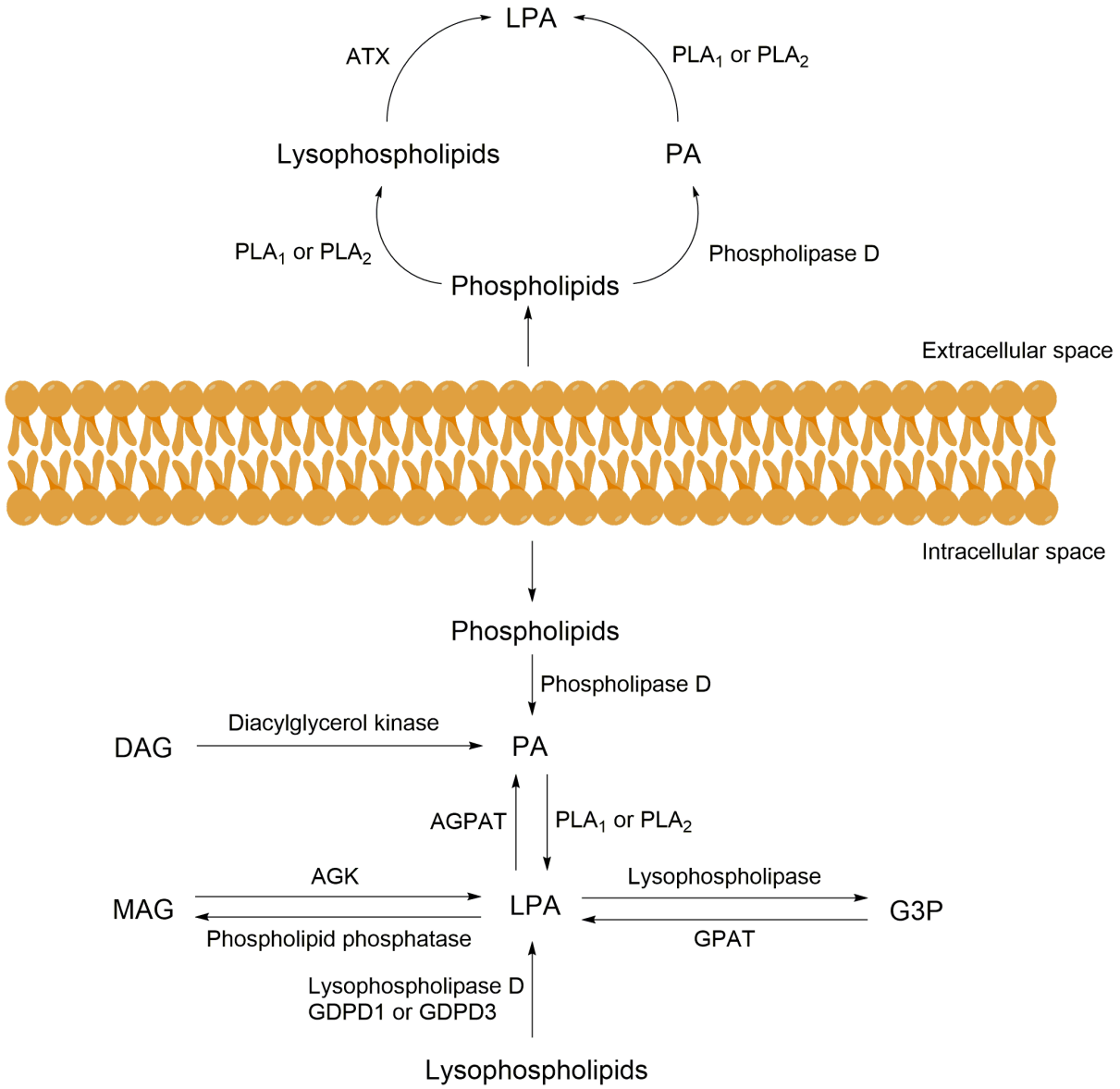

Figure 3 Metabolism of extracellular and intracellular LPA. Extracellular LPA can be produced by at least two different pathways, both based on a sequential degradation of membrane phospholipids until producing LPA. In this sequential degradation, either first acts the enzyme phospholipase A1 or A2 (PLA_1 or PLA_2) and later autotaxin (ATX) (left branch of the pathway), or first acts phospholipase D and then PLA_1 or PLA_2 (right branch of the pathway). Intracellular LPA can be produced by at least four pathways, for example via the enzymatic action of acylglycerol kinase (AGK), phospholipases A1 or A2 (PLA_1 or PLA_2), a glycerol-3-phosphate acyltransferase (GPAT) or the lysophospholipase activity of GDPD1 or GDPD3. Moreover, it can be further metabolized at least via three pathways based on the action of a phospholipid phosphatase, an acylglycerol-3-phosphate acyltransferase (AGPAT) or lysophospholipase activity.

LPA is the smallest known lipid with biological activity which signals mainly through G protein-coupled receptors (GPCRs), triggering important cellular responses, such as cell proliferation, migration and cytoskeletal organization (Choi et al. 2010; Stoddard and Chun 2015; Yung, Stoddard, and Chun 2014). At least nine receptors are known to interact with LPA: eight GPCRs (LPAR1 – 6, GPR87 and P2Y10) and one Ca^{2+} channel receptor (TRPV1) (Figure 4) (Geraldo et al. 2021). The receptors are widely expressed in many organs, for example

brain, testis, lung, heart, prostate and ovary (Geraldo et al. 2021). Furthermore, several studies have linked extracellular LPA and its receptors to pathological conditions such as cancer (Geraldo et al. 2021). For example, LPAR1 and LPAR4 have been associated with cancer cell migration and invasiveness (Li et al. 2009; Shida et al. 2004; Takahashi et al. 2017), and both LPAR3 and LPAR6 have been linked to tumor proliferation, invasiveness and aggressiveness of different cancers (Altman et al. 2010; Kato et al. 2012; Younis and Rashid 2017; Yu et al. 2008). Furthermore, LPA-LPAR signaling has been shown to promote EMT, a process that is essential for cancer cells invasive and metastatic properties (Burkhalter et al. 2015; Ha et al. 2016; Hashimoto et al. 2016).

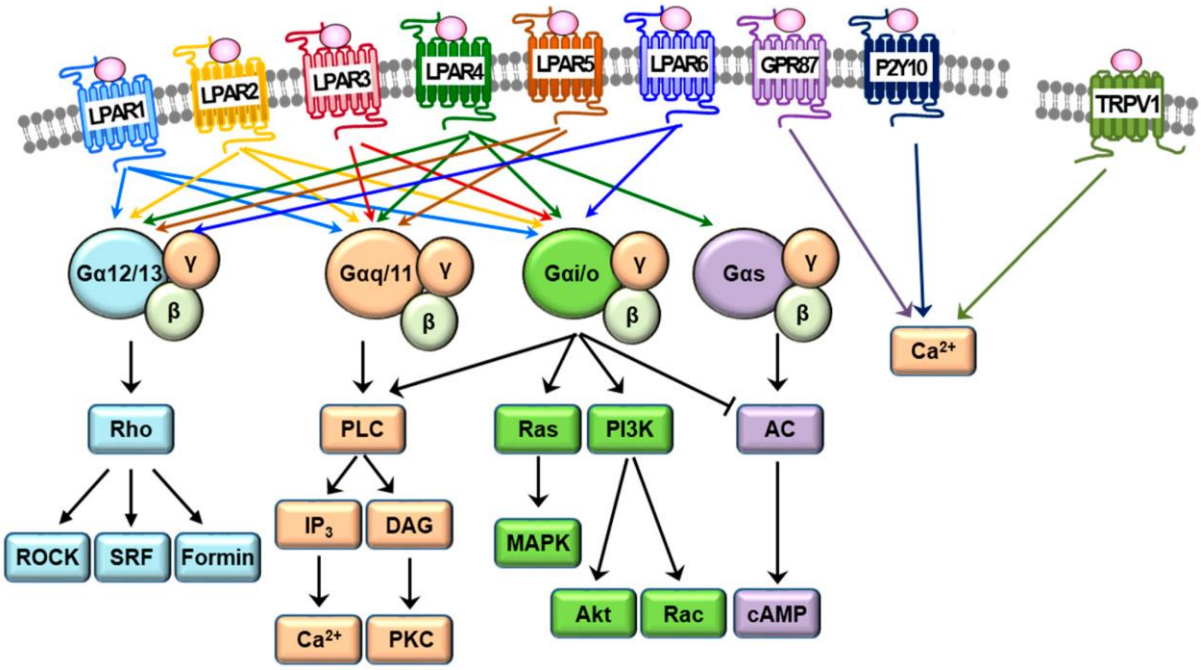

Figure 4 Extracellular LPA signaling. Extracellular LPA interacts with at least eight G protein-coupled receptors (GPCRs) (LPAR 1 – 6, GPR87 and P2Y10) and one Ca^{2+} channel receptor (TRPV1), which activates different signaling cascades, ending in cellular responses such as cytoskeletal reorganization and cell proliferation. Adapted (Lee et al. 2019).

1.2.3 Intracellular LPA: metabolism and signaling

To date, at least four pathways have been identified for the intracellular production of LPA (Figure 3). The first pathway is based on the phosphorylation of monoacylglycerol (MAG) by the enzyme acylglycerol kinase (AGK), producing LPA (Pagès et al. 2001); the second pathway via the breakdown of PA that is produced from either the hydrolysis of phospholipids by phospholipase D or the phosphorylation of diacylglycerol (DAG) by diacylglycerol kinase (DAGK). Subsequently, PLA_1 or PLA_2 catalyzes the hydrolysis of one ester bond in PA resulting in LPA (Aoki, Inoue, and Okudaira 2008). The third pathway is mediated by the glyc-

erol-3-phosphate acyltransferase (GPAT) enzymes, that catalyze the first reaction in the novo production of glycerophospholipids and triglycerides. Specifically, glycerol-3-phosphate (G3P) is acylated by GPATs using acyl-CoA to synthesize LPA (Vancura and Haldar 1994). Recently a fourth pathway was identified based on the removal of the phosphate head-group of lysophospholipids by two glycerophosphodiester phosphodiesterases with lysophospholipase activity, namely GDPD1 (also known as GDE4) and GDPD3 (also known as GDE7) (Ohshima et al. 2015; Tserendavga et al. 2022).

In addition to its production, LPA can also be further metabolized via three possible pathways (Figure 3). In the first pathway, the family of phospholipid phosphatase enzymes dephosphorylates LPA to MAG (Vanderbend et al. 1992). In the second pathway, the members of the acylglycerol-3-phosphate acyltransferase (AGPAT) enzyme family esterifies LPA to PA (Bishop and Bell 1988). Finally, there is evidence showing that an enzyme with lysophospholipase activity, patatin-like phospholipase domain-containing protein 7, is able to hydrolyze the ester bond of LPA to produce G3P (Baker and Chang 1999; Kienesberger et al. 2008; Thompson and Clark 1994).

In contrast to extracellular LPA, there is little known about the function of intracellular LPA. In addition to its role as a metabolic intermediate in phospholipid metabolism, there are studies demonstrating that LPA can act as an intracellular signaling molecule, for example LPA has been shown to interact with cytoskeletal proteins such as gelsolin (Meerschaert et al. 1998) and villin (Tomar et al. 2009). Additionally, Chemin and colleagues showed that the K^+ channels TREK-1, TREK-2 and TRAAK were opened by intracellular LPA, providing a link between lipid status and cellular electrogenesis (Chemin et al. 2005), although the mechanism is unclear. TREK-1, TREK-2 and TRAAK respond to mechanical stimuli, and thus a possible mechanism may be that LPA influences the shape of the membrane, which is strongly influenced by cytoskeletal proteins. Interestingly, in pancreatic ductal adenocarcinoma BxPC-3 cells, hyperpolarization of the membrane via the TREK-1-specific activator BL1249 was found to inhibit migration (Sauter et al. 2016), which the authors attributed to changes in the shape of the membrane. Moreover, intracellular LPA was also reported to be related to mitochondrial dynamics. For example, it was previously shown that accumulation of intracellular LPA rescued the mitochondrial fragmentation phenotype of *C. elegans* mutants (Ohba et al. 2013). LPA was also shown to promote mitochondrial fusion via the mitochondrial carrier homologue 2 (Labbé et al. 2021), a mechanism that was supported in recent work describing a

role for mitofusin 2 in this process (Goldman et al. 2024). Furthermore, McIntyre and coworkers demonstrated that LPA was able to directly bind to the peroxisome proliferator-activated receptor gamma (PPARγ) and activate the expression of a PPAR-responsive element reporter (McIntyre et al. 2003). Interestingly, subsequent work on PPARγ and the enzyme glycerol-3-phosphate acyltransferase 1 (GPAT1) showed that not only the levels of LPA, but also the activity of PPARγ and the expression of CD36, a PPARγ target, were increased in Chinese hamster ovary (CHO) cells upon the overexpression of GPAT1, which produces LPA (Stapleton et al. 2011).

1.3 Glycerol-3-phosphate acyltransferase 1, mitochondrial (GPAM)

1.3.1 Glycerol-3-phosphate acyltransferases (GPATs)

Glycerol-3-phosphate acyltransferases (GPATs) catalyze the first step in de novo glycerophospholipid and triacylglycerol (TAG) synthesis, namely the acylation of glycerol-3-phosphate (G3P) with long-chain acyl-CoA to produce LPA (Figure 5). Furthermore, GPATs are also the rate-limiting enzymes for such syntheses (Yamashita, Hayashi, Matsumoto, et al. 2014). After the production of LPA, the molecule is further acylated by an acylglycerol-3-phosphate acyltransferase (AGPAT) to phosphatidic acid (PA), which is then dephosphorylated by the phosphatidate phosphatase LPIN (also known as lipin) to diacylglycerol (DAG). PA and DAG are important molecules for the synthesis of glycerophospholipids (Yamashita, Hayashi, Matsumoto, et al. 2014). Finally, DAG is acylated to produce TAG by diacylglycerol acyltransferase (DAGT). TAG can be stored in lipids droplets or further metabolized (Takeuchi and Reue 2009), making GPATs key regulators in the synthesis of glycerophospholipids and triacylglycerols.

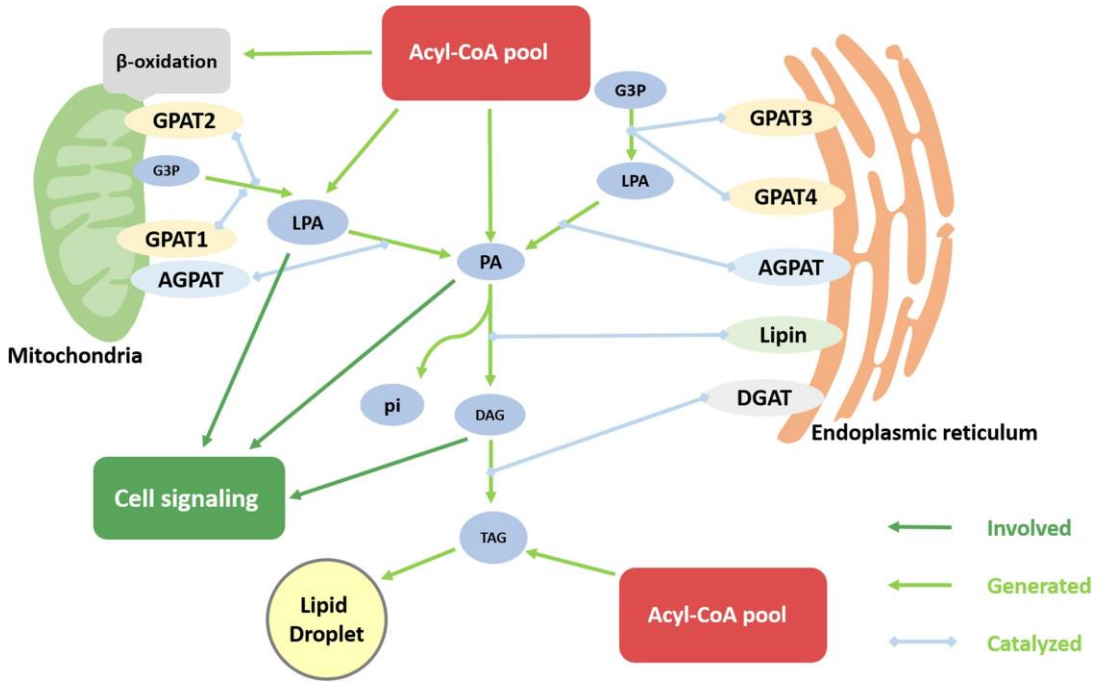

Figure 5 De novo glycerophospholipid and triacylglycerol synthesis. The glycerol-3-phosphate acyltransferases (GPATs) of the mitochondria GPAT1 and GPAT2, and the endoplasmic reticulum GPAT3 and GPAT4 catalyze the first step in the de novo synthesis of glycerophospholipid and triacylglycerol, namely the addition of an acyl group to glycerol-3-phosphate (G3P) producing lysophosphatidic acid (LPA). Next, LPA is acylated by an acyl-glycerol-3-phosphate acyltransferase (AGPAT), producing phosphatidic acid (PA), which is dephosphorylated by a phosphatidate phosphatase LPIN (lipin) to diacylglycerol (DAG) and inorganic phosphate (pi). PA and DAG are important precursors for the synthesis of glycerophospholipids. DAG can be acylated by diacylglycerol acyltransferase (DGAT) to form triacylglycerol (TAG), which can be stored in lipid droplets (Yu et al. 2018).

To date, four isoforms of GPATs have been identified in mammals. They all have four conserved acyltransferase motifs (Karasawa et al. 2019), but differ with respect to subcellular localization, size, substrate preferences, resistance to inactivation by N-ethylmaleimide (a sulfhydryl agent that irreversibly binds and modifies free sulfhydryl (-SH) groups on cysteine residues in proteins often leading to protein inactivity), physiological and pathological roles (Yu et al. 2018); what is discussed in further detail in the following paragraphs. According to their subcellular localization, these isoforms can be divided into two groups: the mitochondrial GPATs, GPAT1 and GPAT2 that are inserted into the outer membrane of the mitochondria, and the endoplasmic reticulum GPATs, GPAT3 and GPAT4 that are found in the membrane of the endoplasmic reticulum (Wendel, Lewin, and Coleman 2009).

The mitochondrial GPAT1, also known as glycerol-3-phosphate acyltransferase 1, mitochondrial (GPAM), has 828 amino acids and a molecular weight of 94 kDa (Karasawa et al. 2019). GPAM preferentially uses saturated acyl-CoAs for the acylation of G3P, and selectively acylates the position 1 of G3P (Yamashita, Hayashi, Nemoto-Sasaki, et al. 2014). Furthermore, it is the only isoform known to be resistant to inactivation by N-ethylmaleimide (Yu et al.

2018). GPAM has an important role in the glycerophospholipid and triacylglycerol synthesis, which is in line with previous studies revealing that it is responsible for a considerable fraction of the total GPAT activity in metabolically-active organs, such as heart (roughly 30% of the GPAT activity) (Lewin et al. 2008) and liver (30 – 50% of the GPAT activity) (Coleman and Mashek 2011). Due to its importance in the liver and heart and links to glycerophospholipid and triacylglycerol synthesis, extensive research has been carried out on the role of this enzyme in a variety of diseases, including metabolic disorders and cancer, which is explored in more detail in the later sections.

GPAT2, also found in the mitochondria, is made up of 801 amino acids and has a molecular weight of 89 kDa (Karasawa et al. 2019). This isoform prefers arachidonoyl-CoA for the acylation of G3P (Cattaneo et al. 2012). While GPAM is resistant, GPAT2 is susceptible to inactivation by N-ethylmaleimide (Yu et al. 2018). GPAT2 seems not to be related to lipid metabolism. For example, Wang and coworkers showed that GPAT2 expression remained the same in the liver of fasted rats and fasted rats that were subsequently refed their normal diets, suggesting that GPAT2 may not be related to triacylglycerol production or accumulation of energy in the liver (Wang et al. 2007). GPAT2 is principally expressed in spermatocytes in the early stages of development and may perform its enzymatic activity mainly in the testis (Cattaneo et al. 2012). Garcia-Fabiani and coworkers showed that the transcription of *GPAT2* was upregulated, and the content of triacylglycerol increased in testis during the development of the genitalia in mice (Garcia-Fabiani et al. 2015), suggesting that GPAT2 may be related to the development of the reproductive system. Furthermore, another study showed that GPAT2 is related to preserving the integrity of DNA, cell cycle dynamics and epigenetics (Fratta et al. 2011), as well as tumorigenesis. For example, using publicly-available microarray gene expression databases, a compiled sample set of data from different types of cancers was established, where prostate, lung, melanoma, and breast cancer presented a significantly larger proportion of samples with ‘high *GPAT2* expression’, based on a three-quantile division of the *GPAT2* expression values (Pellon-Maison et al. 2014). Furthermore, the group showed that *GPAT2* expression correlated with a higher histological grade in breast cancer and in concordance, *GPAT2* knockdown in the triple-negative breast cancer cell line MDA-MB-231 reduced cell proliferation, migration and tumorigenicity (Pellon-Maison et al. 2014).

The endoplasmic reticulum GPAT3 contains 434 amino acids and has a molecular weight of 49 kDa (Karasawa et al. 2019). Additionally to the acylation of G3P to produce LPA, this

isoenzyme also acylates LPA to PA, and is thus also known as GPAT3/AGPAT10 (Cao et al. 2006; Sukumaran et al. 2009). GPAT3 acylates its substrates using a number of saturated and unsaturated acyl-CoAs, with oleoyl-CoA being the most used (Sukumaran et al. 2009). This isoform is susceptible to inactivation by N-ethylmaleimide (Yu et al. 2018) and as the other isoforms, GPAT3 has been studied in relation to lipid metabolism. GPAT3-knockout mice showed a total GPAT activity decrease by 80% in the white adipose tissue, while the total GPAT activity in the liver was not altered (Cao et al. 2014), indicating that GPAT3 may be more relevant in lipid metabolism in adipocytes compared to the liver. Furthermore, Shan and coworkers showed that the stable knockdown of GPAT3 in 3T3-L1 adipocytes triggered a drop in their GPAT activity, a large reduction in the storage of lipids and a decrease in the expression of several adipogenic markers during differentiation into adipocytes (Shan et al. 2010). Taken together, GPAT3 seems to play an important role in the GPAT activity of adipose tissue. GPAT3 was also reported to be important in cancer. Zhou and coworkers showed a significant increase in the expression of GPAT3 in the multikinase inhibitor sorafenib resistant hepatocellular carcinoma cells compared to the control parental cells. Accordingly, the knockdown of GPAT3 reduced the resistance to sorafenib, while the overexpression of GPAT3 in the hepatocellular carcinoma cell lines MHCC97H and Hep3B promoted resistance to sorafenib (Zhou et al. 2024). Additionally, Wang et al. observed that GPAT3 confers chemoresistance in colorectal cancer through lipid droplet accumulation (Wang et al. 2024).

The endoplasmic reticulum GPAT4 contains 456 amino acids and has a molecular weight of 52 kDa (Karasawa et al. 2019). GPAT4 has catalytic activity with saturated and unsaturated acyl-CoAs, for example palmitoyl- or linoleoyl-CoA (Chen et al. 2008). It is also susceptible to inactivation by N-ethylmaleimide (Chen et al. 2008), and has also been shown to be important for lipid metabolism. GPAT4 relocalizes from the endoplasmic reticulum to a subset of forming lipids droplets during oleate loading, where it becomes stably associated with the droplets to enlarge those forming lipid droplets (Wilfling et al. 2013). Furthermore, Beigneux and coworkers showed that the knockout of GPAT4 in mice led to defects in the lactation, by producing milk with a low content of lipids and the atrophy of the mammary tissue (Beigneux et al. 2006). GPAT4 has also been linked to cancer, with one study demostrating a significant association between *GPAT4* expression with shorter overall survival in high-grade serous ovarian cancer patients (Meng, Sun, and Liu 2023).

1.3.2 GPAM in metabolic disorders and the development of FSG67

As mentioned in Section 1.3.1 above, GPAM has been related to several diseases, including metabolic disorders and cancer. Insulin resistance has been linked to excessive amount of lipids in locations outside the body fat, such as skeletal muscle or liver (Kim et al. 2001). And since in the liver a considerable part of the GPAT activity is due to GPAM (Coleman and Mashek 2011), GPAM might contribute to insulin resistance through hepatic lipid accumulation. For instance, it was reported that overexpressing GPAM in the liver of rats produced an overaccumulation of lipids in the liver and insulin resistance without having an obese phenotype nor supplying a diet with fat-enriched content (Nagle et al. 2007). Additionally, Zhang and colleagues showed that the overexpression of GPAM triggered a decreased repression of gluconeogenesis due to insulin, and a decrease in the activity of mTORC2, leading to insulin resistance (Zhang et al. 2012; Zhang et al. 2014). A more recent study reported that the combination of elevated levels of palmitic acid and GPAM activity hindered the insulin suppression of glucose in primary mouse hepatocytes (Zhang et al. 2024).

Besides insulin resistance, alterations in GPAM have been shown to lead to several hepatic diseases. Metabolic dysfunction-associated fatty liver disease (MALFD) refers to a chronic liver disease in which there is an accumulation of fat in the liver independent of alcohol consumption (Rinella et al. 2023). MALFD may progress to more severe phenotypes, such as metabolic dysfunction-associated steatohepatitis (MASH) that is accompanied by symptoms such as hepatocyte injury, inflammation and fibrosis, which may then progress to liver cirrhosis and liver cancer (Bence and Birnbaum 2021). Importantly, GPAM has been suggested to be relevant at the different stages of this progression. For example, in a recent study several sequence variants not previously associated with fatty liver disease were identified; among them, the researchers observed a significant increase in genetic variants related to lipid metabolism and found a strong correlation between the variants rs2792751 in *GPAM* and rs429358 in *APOE* and fatty liver disease (Jamialahmadi et al. 2021). Smith and coworkers showed that the deletion of *GPAM* protected mice from diet-induced hepatic steatosis (Smith et al. 2024). The authors also observed a reduction in liver fat accumulation in the genetically obese, leptin-deficient *ob/ob* mice with a hepatocyte-specific deletion of *GPAM*. Consistently, the deletion of *GPAM* prevented mice from developing diet-induced MASH. Moreover, Hakim and coworkers performed genome-wide association studies and found the genetic variant rs10787429 in *GPAM* to be associated with biochemical markers of liver cirrhosis (Hakim et al. 2021).

Based on the metabolic disorders in which GPAM seems to be implicated, Wydysh and coworkers suggested that a small direct inhibitor of this enzyme could be a therapeutic agent to address health problems related to an excess of lipids, such as MALFD or diabetes (Wydysh et al. 2009). Therefore, several compounds were synthesized with a series of benzoic and phosphonic acids to target GPAM, and from these, FSG67 (2-(nonylsulfonamido) benzoic acid) was the most promising as it exhibited the highest GPAT inhibitory activity (Wydysh et al. 2009; Wydysh et al. 2010). Interestingly, FSG67 was shown to not only inhibit GPAM, but rather inhibits general mitochondrial GPAT activity (Kuhajda et al. 2011; Wydysh et al. 2009), and more recently, the enzymatic activity of GPAT3 (Fan et al. 2023).

FSG67 has been researched both in vitro and in vivo. One of the earliest reports showed that FSG67 suppressed lipid synthesis in 3T3-L1 adipocytes (Kuhajda et al. 2011). Moreover, McFadden and coworkers showed that FSG67 enhanced fatty acid oxidation, increased ATP levels, inactivated AMP activated protein kinase and increased reactive oxygen species production in hypothalamic neurons in vitro (McFadden et al. 2014). A more recent study reported that blocking GPAT3 with FSG67 inhibited lipopolysaccharide-induced Kupffer cells inflammation, which can promote inflammatory liver injury (Fan et al. 2023). In vivo, FSG67 was shown to reduce body weight and decrease energy intake in lean and diet-induced mice without conditioned taste aversion, as well as reduce body weight, specifically from the fat mass (Kuhajda et al. 2011). During repeated treatment with a low amount of FSG67, diet-induced obese mice reduced their fatty tissue content and increased the oxidation of fatty acids during the entire experiment (Kuhajda et al. 2011). In addition, the researchers observed lower serum leptin levels, a decrease in the accumulation of lipids in the liver, and smaller white adipocytes in the diet-induced obese mice chronically treated with FSG67 (Kuhajda et al. 2011).

Observing the promising results of FSG67, recent studies focused on the effect of using the compound to inhibit the synthesis of LPA, the product of the GPAT enzymatic activity. Simic and colleagues showed that the inhibition of LPA production in the bone marrow by FSG67 lessened the increase of the bone-derived hormone FGF23 (Simic et al. 2020). FGF23 controls blood phosphate levels and its dysregulation is associated with significant morbidity and mortality (Simic et al. 2020). In addition, a more recent study demonstrated that the inhibition of LPA synthesis by FSG67 led to mitochondrial fragmentation with complete penetrance,

which was reversible after washing out the inhibitor (Goldman et al. 2024). Therefore, the published work thus far suggests that FSG67 may be effective in the treatment of obesity, diabetes, and other conditions associated with increased lipid accumulation.

1.3.3 GPAM in cancer

To date, there is relatively little published about GPAM in cancer. One of the first studies showed that knocking down GPAM in the cancer cell lines MCF7 (estrogen receptor positive, erb-b2 receptor tyrosine kinase 2 (ERBB2; HER2) negative breast cancer), MDA-MB-231 (triple negative breast cancer), and HeLa (cervical cancer) decreased cell migration (Marchan et al. 2017). Furthermore, silencing GPAM led to a reduction of 16:0 and 18:1 LPA in MCF7 cells (Marchan et al. 2017). Thus, to determine if intracellular LPA has an effect on cell migration, LPA was transfected into MCF7 cells, which significantly increased migration (Marchan et al. 2017). Moreover, it was confirmed that LPA-transfected cells that migrated faster also contained a higher amount of intracellular LPA than the non-LPA-transfected cells (Marchan et al. 2017). Taken together, these results suggest that intracellular LPA may be an important factor in cancer cell migration.

Since increased cancer cell migration in vitro can be associated with increased aggressiveness of the cancer, propensity to metastasize and therefore worse disease outcome, public microarray gene expression data of different types of cancer, such as ovarian, breast, colon and lung cancer, were analyzed, and revealed that an increased *GPAM* expression was significantly associated with reduced overall survival in ovarian cancer patients (Marchan et al. 2017). Having made this observation, the researchers knocked down GPAM in ES-2 clear cell ovarian cancer cells and the migration of these cells was decreased (Marchan et al. 2017), an important fact since cell migration can enhance tumor development and metastasis (Horwitz and Webb 2003). Finally, an in vivo model was established by injecting ES-2 cells subcutaneously into mice. Using this model, it was shown that the knockdown of GPAM in ES-2 cells led to reduced tumor volume in vivo compared with the controls (Marchan et al. 2017).

Another early study investigated how the loss of GPAM influences susceptibility to develop liver cancer (Ellis et al. 2012). After treatment with diethylnitrosamine, a hepatocarcinogen, together with phenobarbital, a tumor promoter, male GPAM-knockout mice had fewer macroscopically visible masses in the liver compared with wild-type control mice. Microscopically, the knockout mice had less malignant liver neoplasms than the control mice (Ellis et al.

2012). More recent work demonstrated a role for GPAM in bile duct cancer, whereby GPAM knockdown reduced the proliferation and invasion of the cholangiocarcinoma cells HuCCT1 and TFK1 (Zhang et al. 2022). Additionally, recent findings from our research group have also shown that the downregulation of GPAM expression decreased cancer cell migration in the high-grade serous ovarian cancer (HGSOC) cells COV318, Kuramochi, OAW28, OVCAR4 and OVCAR8, as well as altered spheroid formation and outgrowth in OVCAR8 cells (Gonscharow 2025). The above studies all contrast with one of the first studies on GPAM in cancer, which reported that higher *GPAM* expression was associated with a longer overall survival in breast cancer, as well as increased phospholipid synthesis (Brockmöller et al. 2012).

The studies described thus far all used genetic interventions to reduce GPAM expression. Two recent studies employed the GPAT inhibitor FSG67 to show antitumor activity in some types of cancer. In one study, metabolomics profiling was performed on pancreatic ductal adenocarcinoma from patient-derived tumor xenografts to determine if there was an association between levels of specific metabolites and characteristics such as the overall survival of the patients, resistance to chemotherapeutic agents and the features of the tumor (Kaoutari et al. 2021). Indeed, from their analysis, the authors observed several metabolites to be associated with resistance to chemotherapeutic agents, for example glycerophospholipid-content positively correlated to chemotherapy resistance (Kaoutari et al. 2021). To study if targeting the synthesis of these metabolites could impact the response to anticancer drugs, the authors treated primary pancreatic ductal adenocarcinoma-derived cells with the chemotherapeutic agents oxaliplatin, gemcitabine or 5-FU in combination with FSG67 or alone. As a result, an increased sensitivity to the three cytotoxic drugs in presence of FSG67 was achieved (Kaoutari et al. 2021). Another recent study showed that low-glycerol-3-phosphate dehydrogenase expressing kidney cancer cells were more sensitive to FSG67, both in vitro and in vivo (Yao et al. 2023). Finally, Irifune and collaborators evaluated the mRNA expression of the four GPAT isoforms in acute myeloid leukemia cells, and the researchers found *GPAM* to be the highest expressed among the four GPAT isoforms (Irifune et al. 2023). Next, the activity of GPAM was inhibited by several methods, including knockdown and the use of FSG67 (Irifune et al. 2023). In vitro, it was shown that FSG67 reduced the viability of acute myeloid leukemia cells without affecting normal hematopoietic cells. Interestingly, when the researchers supplemented exogenously LPA to culture media, the viability of the acute myeloid leukemia cells treated with FSG67 improved. Furthermore, FSG67 inhibited the accumulation of

lipid droplets (Irifune et al. 2023). In vivo, xenotransplanted mice treated with FSG67 had a significantly longer survival compared with the control mice (Irifune et al. 2023). Taken together, silencing GPAM or inhibiting GPAM with the GPAT inhibitor FSG67 are promising strategies to treat cancers where the glycerophospholipid metabolism is implicated, such as ovarian cancer.

1.4 Aim of the PhD thesis

Ovarian cancer is one of the most common types of cancers in women (Reid, Permuth, and Sellers 2017). The absence of effective screening methods complicates the detection of ovarian cancer at earlier stages (Berek et al. 2021), and since symptoms often manifest themselves at later stages of the disease, the 5-year relative survival rate is only 29% (Reid, Permuth, and Sellers 2017). In the last decades, lysophosphatidic acid (LPA) has emerged as an important factor in a number of different diseases, including cancer. To date, most of the research on LPA has focused on extracellular LPA, while little is known regarding intracellularly-produced LPA in cancer. Expression of the intracellular LPA-producing enzyme GPAM was shown to be associated with worse prognosis in human ovarian cancer, and experimentally downregulating GPAM expression in breast, endometrioid and ovarian cancer cell lines decreased cancer cell migration in vitro. Furthermore, silencing GPAM also reduced subcutaneous tumor growth in a xenograft mouse model, but the role of GPAM in cancer metastasis has not been investigated in vivo. Thus, the first aim of this PhD thesis was to determine the effect of downregulating GPAM expression with a stable knockdown system, suitable for in vivo studies, as well as pharmacologically inhibiting GPAM's enzymatic activity with the GPAT inhibitor FSG67, using in vitro and in vivo ovarian cancer models. The second aim was to understand the mechanism by which GPAM's enzymatic product, LPA, may influence ovarian cancer cell processes, focusing on autocrine and/or paracrine signaling as well as the identification of possible intracellular protein binding partners.

2 Materials and methods

2.1 Technical equipment

Table 1 Technical equipment used in this study.

Equipment	Supplier
Autoclave 5075 ELV	Tuttenauer
Autoclave VX-150	Systec
Autosampler MPS-2	Gerstel
Blot imager Vilber Fusion Fx7	Vilber
Cell counter Casy TT	OMNI Life Science
Centrifuge 3-30K	Sigma
Centrifuge 400R	Heraeus
Centrifuge 5415R	Eppendorf
Centrifuge Megafuge 1.0R	Heraeus
Centrifuge MiniSpin	Eppendorf
Centrifuge MiniSpin plus	Eppendorf
Changing station ARIA	Tecniplast
CO_2 incubator	Binder
Compact portable balance CS 200	Ohaus
Confocal laser scanning microscope TCS SP8	Leica Microsystems GmbH
Electrophoresis unit Mini-PROTEAN®	BioRad
Fume hood	Waldner
Ice flake machine AF 100	Scotsman
Isoflurane vaporizer	Northern Vaporisers
IVIS Spectrum in vivo imaging system	Revvity
Laminar flow hood HERAsafe	Heraeus
Magnetic stirrer	IKA
Micro scales	EW, Kern
Micropipettes (2, 10, 20, 100, 200, 1000, 5000 µl)	Eppendorf
Microscope BZ-X810	Keyence

Microscope eclipse TS100 inverted	Nikon
Milli-Q® IQ water purification system	Millipore
Mini vortex mixer	Thermo Fisher Scientific
Multichannel pipette (300 µl)	Eppendorf
Nalgene Mr. Frosty™ freezing container	Thermo Fisher Scientific
NanoDrop One	Thermo Fisher Scientific
Nimbus pipetting robot	Hamilton
pH meter	Schott Instruments
picoEmerald IR laser system	APE GmbH
Plate reader infinite M200 Pro	Tecan
Power pack HC	BioRad
Power pack P25T	Biometra
Precision balance EW150-3M	Kern
Precision balance ME235P	Sartorius
QuantStudio™ 3 Real-Time PCR System	Applied Biosystems
Raman microscope WITec alpha300 R	Oxford Instruments
RAS-4 rodent anesthesia system	Revvity
Rocking platform	VWR
Rotating wheel	VWR
Shaker KS 260 basic	IKA
Smart Flow IVC Air Handling Unit	Tecniplast
Sonicator sonoplus mini	Bandelin
Surgical instruments	Fine Science Tools
Thermal cycler T3000	Biometra
Thermo shaker	Peqlab
Thermo shaker PHMT Grant-bio	Keison
Thermomixer	Eppendorf
Trans-Blot® SD semi-dry transfer cell	BioRad
Vacuum pump	Vacuubrand
Vortex-Genie2	Bender & Hobein
Water bath	GLF

2.2 Consumables

Table 2 Consumables used in this study.

Consumable	Supplier
4 – 20% Mini-PROTEAN® TGX™ Precast Protein Gels, 10-well, 50 µl	BioRad
Beads, control agarose P-B000	Echelon Biosciences
Beads, LPA-coated agarose L-6101	Echelon Biosciences
CASY cups	OMNI Life Science
Cell culture dishes (10, 15 cm)	Sarstedt
Cell culture flasks (T25, T75, T175)	Sarstedt
Cell culture inserts 24-well 8.0 µm pore	SABEU
Cell culture multiwell plates (6-, 12-, 24-, 96-well)	Sarstedt
Cryogenic vials	Sarstedt
Extra thick blot papers	BioRad
Falcon tubes (15, 50 ml)	Sarstedt
Filter tips (2.5, 10, 100, 200, 1000 µl)	Sarstedt
Glass bottom microwell dish 35 mm	MatTek
Glass pasteur pipettes	BRAND GmbH + Co
MicroAmp™ optical 96-well reaction plate	Thermo Fisher Scientific
MicroAmp™ optical adhesive film	Thermo Fisher Scientific
Microplates 96-well black	Greiner Bio-One
Microplates 96-well Nunc white	Thermo Fisher Scientific
Minisart® syringe filters (0.2 µm)	Sartorius
Pipette tips (10, 200, 1000, 5000 µl)	Sarstedt
PVDF transfer membrane	Thermo Fisher Scientific
Reaction tubes (0.5, 1.5, 2, 5 ml)	Sarstedt
Serological pipettes (5, 10, 25, 50 ml)	Sarstedt
Syringe (1, 10, 30, 50 ml)	B.Braun
Syringe needle 20G	B.Braun
Syringe needle 30G	BD Bioscience

2.3 Chemical reagents

Table 3 Chemical reagents used in this study.

Reagent	**Supplier**
16:0 LPA (U-13C)	Avanti Research
1-palmitoyl-d_9 lysophosphatidic acid	Cayman Chemical
Ammonium persulfate	Sigma-Aldrich
Bovine serum albumin	Carl Roth
Crystal violet	Sigma-Aldrich
Dimethyl sulfoxide	Sigma-Aldrich
D-luciferin potassium salt	Revvity
Ethanol, absolute	Carl Roth
FSG67	Focus Biomolecules
Glycine	Carl Roth
Isoflurane	CP-Pharma
Methanol, HPLC grade	Carl Roth
Milk powder	Carl Roth
NP-40	Roche
Poly(2-hydroxyethyl methacrylate)	Sigma-Aldrich
Polybrene	Merck Millipore
Ponceau S	Carl Roth
Potassium chloride	Carl Roth
Potassium dihydrogen phosphate	Carl Roth
SDS pellets	Carl Roth
Sodium chloride	AppliChem
Sodium deoxycholate	Carl Roth
Sodium hydrogen phosphate	Sigma-Aldrich
Tetramethylethylendiamine	Carl Roth
TopFluor® Lyso PA	Avanti Research
Tris	Carl Roth
TritonX-100	Sigma-Aldrich
Tween20	AppliChem
β-mercaptoethanol	Carl Roth

2.4 Molecular biology reagents

Table 4 QuantiTect Primer Assays from Qiagen used in this study.

Target gene	Catalog number
ACTB	QT00095431
GPAM	QT01668408

Table 5 Plasmids used in this study.

Plasmid	Supplier
pGL4.51[luc2/CMV/Neo]	Promega

Table 6 Lentivirus short hairpin RNA (shRNA) knockdown vectors used in this study. All of them were acquired from VectorBuilder.

Catalog number	Description
LVC(VB010000-9532axg)-b	pLV[shRNA]-mCherry/Puro-U6>Scramble_shRNA (VB010000-9532axg)
LVS(VB250130-1189kqe)	pLV[shRNA]-mCherry:T2A:Puro-U6>hGPAM[shRNA#1]
LVS(VB250130-1186yet)	pLV[shRNA]-mCherry:T2A:Puro-U6>(hGPAM[shRNA#2])
LVS(VB250130-1187fxy)	pLV[shRNA]-mCherry:T2A:Puro-U6>(hGPAM[shRNA#3])

Table 7 Primary antibodies used in this study.

Antibody	Source	Catalog number, supplier
Anti-GPAM	Mouse	sc-398135, Santa Cruz Biotechnology
Anti-LPA	Mouse	Z-P200, Echelon Biosciences
Anti-β-actin	Mouse	A2228, Sigma-Aldrich

Table 8 Secondary antibodies used in this study.

Antibody	Source	Catalog number, supplier
Anti-mouse horseradish peroxidase (HRP) linked	Horse	7076S, Cell Signaling

2.5 Solutions, buffers, media and kits

Table 9 Commercial solutions, buffers and media used in this study.

Solution/buffer/medium	Supplier
Acrylamide (30% (v/v))	Carl Roth
Buffer concentrate A	Carl Roth
Buffer concentrate K	Carl Roth
CASY ton	OMNI Life Science
Diethylpyrocarbonate treated water	Thermo Fisher Scientific
Geneticin disulfate (G418) solution	Carl Roth
Gibco™ Fetal Bovine Serum	Thermo Fisher Scientific
Gibco™ Opti-MEM™ I Reduced Serum Medium	Thermo Fisher Scientific
Loading buffer 4X	BioRad
Phosphatase inhibitor cocktails II & III	Sigma-Aldrich
Precision Plus Protein™ Dual Colour Standard	BioRad
Protease inhibitor cocktail I	Sigma-Aldrich
PURECL™ Dura	Vilber
Puromycin	Thermo Fisher Scientific
RPMI 1640	PAN Biotech
Tris/Glycine/SDS Buffer (10X)	BioRad
Trypsin / EDTA 0.05% / 0.02% in PBS	PAN Biotech

Table 10 Prepared solutions and buffers in this study.

Solution/buffer	Description
Anode buffer	10% (v/v) buffer concentrate A 20% (v/v) methanol in ultrapure water
APS solution	10% (w/v) ammonium persulfate in ultrapure water

Cathode buffer	10% (v/v) buffer concentrate K 20% (v/v) methanol in ultrapure water
Crystal violet fixation solution	0.5% (w/v) crystal violet 20% (v/v) methanol in ultrapure water
Lysis/binding buffer	10% (v/v) glycerol 100 mM NaCl 1% (v/v) Triton X-100 1% Protease-/Phosphatase-Inhibitor-Cocktail 1 mM DTT 20 mM Tris-HCl pH 7.4
Milk blocking solution	5% (w/v) milk powder in 1X TBS-T
Radioimmunoprecipitation assay (RIPA) buffer	50 mM Tris-HCl (pH 7.5) 150 mM NaCl 1% NP-40 0.5% sodium deoxycholate 0.5% SDS 1% Protease-/Phosphatase-Inhibitor-Cocktail
SDS solution	10% (w/v) SDS in ultrapure water
Separation buffer	3 M Tris in ultrapure water pH 8.8
Stacking buffer	0.47 M Tris in ultrapure water pH 6.8
Stripping buffer	0.2 M glycine 0.1% (w/v) SDS 1% (v/v) Tween20 in ultrapure water pH 2.2

TBS-T	10% (v/v) TBS (10X) 0.1% (v/v) Tween20
Tris buffered saline (TBS 10X)	0.5 M Tris 1.5 M NaCl in ultrapure water pH 7.4

Table 11 Commercial kits used in this study.

Kit	**Supplier**
BCA protein assay	Thermo Fisher Scientific
CellTiter-Blue® assay	Promega
High-Capacity cDNA Reverse Transcription Kit	Thermo Fisher Scientific
Lipofectamine™ 3000 Reagent	Thermo Fisher Scientific
ONE-Glo™ Luciferase Assay System	Promega
Pierce™ Silver Stain for Mass Spectrometry	Thermo Fisher Scientific
QuantiFast® SYBR® Green PCR kit	Qiagen
RNase-Free DNase Set	Qiagen
RNeasy Mini kit	Qiagen
ServaPurple Protein Quantification assay	SERVA GmbH
SimplyBlue™ SafeStain	Thermo Fisher Scientific

2.6 Cell lines

Table 12 Commercially available cell lines used in this study.

Cell line	**Description**
COV318	HGSOC cell line. Purchased from Sigma Aldrich
ES-2	CCOC cell line. Purchased from the ATCC
HOSE17-1	Immortalized human ovarian epithelial cell line. Received from Prof. Viola Heinzelmann-Schwarz (University of Basel)

HOSE6-3	Immortalized human ovarian epithelial cell line. Received from Prof. Viola Heinzelmann-Schwarz (University of Basel)
I64-hTERT	Immortalized human ovarian epithelial cell line. Received from Prof. Marina Bagnoli (Fondazione IRCCS Istituto Nazionale dei Tumori)
OVCAR4	HGSOC cell line. Received from Prof. Viola Heinzelmann-Schwarz (University of Basel)
OVCAR8	HGSOC cell line. Received from Prof. Viola Heinzelmann-Schwarz (University of Basel)

Table 13 Cell lines created in this study.

Cell line	**Description**
ES-2_luc	Stably luciferase-expressing ES-2 cell line created by transfection of ES-2 cells with the plasmid pGL4.51. Three clones were isolated, named ES-2_luc_c1, ES-2_luc_c2 and ES-2_luc_c3. Herein ES-2_luc_c3 was extensively studied
ES-2_luc shNEG	Stably luciferase-expressing ES-2 cell line created by transduction of ES-2_luc cells with LVC(VB010000-9532axg)-b, with stable expression of non-targeting scrambled shRNA and the fluorescent marker mCherry. Generated with multiplicities of infection (MOIs) of three, five and eight. Herein the MOI three was extensively studied
ES-2_luc shGPAM1	Stably luciferase-expressing ES-2 cell line created by transduction of ES-2_luc cells with LVS(VB250130-1189kqe), with stable knockdown of *GPAM* and expressing the fluorescent marker mCherry. Generated with MOIs of three, five and eight. Herein the MOI three was extensively studied

ES-2_luc shGPAM2	Stably luciferase-expressing ES-2 cell line created by transduction of ES-2_luc cells with LVS(VB250130-1186yet), with stable knockdown of *GPAM* and expressing the fluorescent marker mCherry. Generated with MOIs of three, five and eight. Herein the MOI five was extensively studied
ES-2_luc shGPAM3	Stably luciferase-expressing ES-2 cell line created by transduction of ES-2_luc cells with LVS(VB250130-1187fxy), with stable knockdown of *GPAM* and expressing the fluorescent marker mCherry. Generated with MOIs of three, five and eight. Herein the MOI three was extensively studied

2.7 Laboratory mice

Table 14 Laboratory mice used in this study.

Mouse	Full nomenclature	Gender	Age at arrival	Supplier
CD-1	Crl:CD1	Female	5 weeks	Janvier Labs
CD-1 nude	Crl:CD1-*Foxn1*^{nu}	Female	5 weeks	Charles River

Table 15 Mice feed in this study.

Feed	Supplier
Nude mouse diet fortified, γ-irradiated (25 kGy)	ssniff
Rat/Mouse diet low phytoestrogen, γ-irradiated (25 kGy)	ssniff

2.8 Culture of the cells

The cells in the present study were maintained in RPMI 1640 (PAN Biotech) supplemented with 10% Gibco™ Fetal Bovine Serum (Thermo Fisher Scientific) (full medium) in a humidified incubator at 37 °C with 5% CO_2 (standard cell culture conditions). When the cells were 70 – 90% confluent, the cells were passaged to keep their exponential growth phase. Namely, the cells were rinsed once with 1X PBS. Then the cells were covered with a thin layer of tryp-

sin solution (PAN Biotech) and incubated at standard cell culture conditions until detachment of the cells. After the trypsinization, the cells were resuspended in full medium and transferred into cell culture flasks. The seeding of cells for subsequent experiments was performed with the trypsinization of cells as explained above, followed by the determination of the cell concentration with the cell counter CASY TT.

The cells were kept in liquid nitrogen for long term storage. For this cryopreservation procedure, the cells were cultured until 80 – 90% confluency, trypsinized as described above, centrifuged for 5 min at 133g and the supernatant removed. The resulting pellet was then resuspended in full medium containing 5% DMSO to avoid the formation of ice crystals at $1 \cdot 10^6$ cells/ml. One ml aliquots of the cell suspension were transferred into cryovials and cooled in the Mr. Frosty™ freezing container (Thermo Fisher Scientific) overnight at -80 °C. Finally, the cryovials were placed into the gas-phase above the liquid nitrogen in a tank.

The cells were revived from the liquid nitrogen by thawing the cryovial containing the cells rapidly in a 37 °C water bath. The defrosted cell suspension was then centrifuged for 5 min at 133g, the supernatant was removed and the cells were resuspended in 1 ml full medium. The final cell suspension was then added into a cell culture flask containing full medium. The cells were passaged after reviving at least twice before performing experiments.

2.9 Antibiotic kill curve

For the generation of transgenic cell lines, it is necessary to specifically select the cells that express the gene of interest. To do so, a selective marker (such as an antibiotic resistance gene) is often cloned into the plasmid that facilitates growth of cells in media containing the respective antibiotic. In this study, the cell line ES-2 was transfected with the plasmid pGL4.51[luc2/CMV/Neo] (Promega) (Table 5 and Figure S1) in order to generate luciferase-expressing ES-2 cells. Consequently, the neomycin resistance gene in the pGL4.51 was used as a selective marker which once successfully incorporated into the genome of the ES-2 cells, allowed them to grow in full media with the antibiotic geneticin disulfate (G418) (Carl Roth). Nevertheless, since the sensitivity of mammalian cells to antibiotics may differ among cell lines, before the procedure, the lowest antibiotic concentration to kill untransformed ES-2 cells was determined by performing an antibiotic kill curve.

For the procedure, cells were seeded at a density of $2 \cdot 10^5$ cells per well in 1 ml full medium in a 24-well plate. The next day, selective media of full medium with increasing concentrations of the antibiotic geneticin disulfate (G418) were prepared (final concentrations of 0, 50, 100, 200, 300, 400, 500, 600, 700, 800, 900 and 1,000 µg/ml). Then, the cells were rinsed once with 1X PBS and the geneticin selective media were added in technical duplicates. On the following days, the cells were monitored using phase contrast microscopy and the geneticin selective media were renewed every two to three days. After 10 days, 300 µg/ml geneticin disulfate (G418) was determined as the lowest antibiotic concentration to kill untransformed ES-2 cells.

2.10 Transfection of the cells

The cell line ES-2 was transfected with the plasmid pGL4.51[luc2/CMV/Neo] (Promega) using lipofection, based on the use of cationic lipids to introduce foreign genetic material into cells (Zhi et al. 2018). The transfection was done to generate a luciferase-expressing ES-2 cell line that could later be used in in vivo experiments to monitor tumor growth non-invasively in mice with an animal imager, such as the IVIS Spectrum in vivo imaging system (Revvity).

For the procedure, the cells were seeded at a density of $2 \cdot 10^5$ cells per well in 1 ml full medium in a 24-well plate to achieve approximately 70 – 80% confluency, when cells are still exponentially growing. On the next day, the cells were rinsed once with 1X PBS and 500 µl RPMI 1640 medium was added to the cells. Then, in an Eppendorf tube 2 µl of the transfection reagent Lipofectamine™ 3000 Reagent was added to 25 µl Gibco™ Opti-MEM™ I Reduced Serum Medium (Thermo Fisher Scientific). In another Eppendorf tube, 0.5 µl P3000™ Reagent and 500 ng plasmid were added to 25 µl Opti-MEM™ I Reduced Serum Medium. Thereafter, the mixture of the second tube was added to the first tube and the combined mixture was incubated at room temperature for 12 min. Next, 50 µl of the combined mixture was added to the RPMI 1640 medium of the cells in the 24-well plate, which was gently tilted back and forth to allow homogeneous distribution of the previously added transfection mixture with the medium. The plate was then incubated at standard cell culture conditions for 7 h after which the transfection medium was replaced with 1 ml full medium. The plate was then incubated under standard cell culture conditions and once the surviving cells of the transfection process reached approximately 50% confluency, the medium was replaced with full medium containing 300 µg/ml of the antibiotic geneticin disulfate (G418)) (geneticin selective

medium) for seven days, with media change every two to three days. Once the cells reached a confluency of approximately 80%, single cell cloning was performed.

2.11 Single cell cloning

In this study transfected ES-2 cells were grown in monoclonal colonies, and specific monoclonal colonies were isolated and expanded independently to obtain a stable ES-2 cell line with high luciferase activity.

Transfected ES-2 cells (Section 2.10) were seeded at a density of $1 \cdot 10^3$ cells in 30 ml full medium in a 15 cm cell culture dish. Two days later, the full medium was replaced with geneticin selective medium. On subsequent days, colony growth was examined under phase contrast microscopy and geneticin selective medium was renewed every two to three days, until several colonies reached a size of at least 50 cells. Then, the dish was rinsed once with 1X PBS, full medium was added and a micropipette with a 200 µl pipette tip was used to aspirate the desired colonies that were transferred to individual wells of a 96-well plate. The colonies were expanded independently until an adequate cell number was achieved for cryopreservation (Section 2.8) and to examine the luciferase activity (Section 2.12).

2.12 In vitro quantification of the luciferase activity

The ES-2 cell lines created transfecting the plasmid pGL4.51[luc2/CMV/Neo] (Section 2.10) and single cell cloning (Section 2.11) were subjected to the ONE-Glo™ Luciferase Assay System (Promega) in order to quantify their luciferase activity. Luciferase is an oxidoreductase which oxidizes its substrate luciferin and produces light (de Wet et al. 1987), which can be measured by light sensitive apparatus such as a luminometer.

First, untransfected ES-2 cells (negative control) and luciferase-transfected ES-2 cells were seeded in technical triplicates at a density of $1 \cdot 10^3$ cells per well in 100 µl full medium in a 96-well Nunc white plate (Thermo Fisher Scientific). The next day, the cells and the ONE-Glo™ reagent were equilibrated at room temperature. Then, 100 µl ONE-Glo™ reagent were added directly into the medium, and the reagent, medium and cells were mixed by pipetting up and down. Next, the mixture was left for 3 min at room temperature to allow complete cell lysis, followed by measuring the luminescence using the plate reader infinite M200 Pro

(Tecan). The clone with the highest luciferase activity was selected for subsequent experiments.

2.13 Transduction of the cells

The ovarian cancer cell line ES-2_luc was transduced with one of four lentivirus short hairpin RNA (shRNA) knockdown vectors (Table 6 and Figure S2). Three of the vectors (LVS(VB250130-1189kqe), LVS(VB250130-1186yet) and LVS(VB250130-1187fxy)) encode shRNA targeting different exons of the *GPAM* gene to create an ES-2_luc cell line with a stable knockdown of GPAM expression. The vector LVC(VB010000-9532axg)-b encodes a non-targeting scrambled shRNA, which was used as a negative control. Additionally, all the mentioned vectors also encode a mCherry fluorescent marker.

The day before the transduction, ES-2_luc cells were seeded at a density of $1.25 \cdot 10^4$ cells per well in 100 µl full medium in a 96-well plate. On the day of the transduction, multiplicities of infection (MOI) of three, five and eight were applied for the transduction procedure. For such a procedure, the transduction media composed of lentivirus vectors and polybrene (Merck Millipore) in RPMI 1640 medium were first prepared. Specifically, the lentivirus vectors were diluted in RPMI 1640 medium according to their viral titer, and the stock polybrene solution was diluted in RPMI 1640 to a final concentration of 12 µg/ml. In the next step, the media in the 96-well plate were replaced with 25 µl of transduction media. In order to avoid the loss of the small transduction media volume due to evaporation, 200 µl RPMI 1640 medium was added to the wells which surrounded the transduced cells, and the 96-well plate was wrapped with clingfilm completely. The plate was then placed into the incubator at standard cell culture conditions and on the next day, 200 µl full medium were added to the cells to stop the transduction process. Then, on the following day, the media were replaced with 200 µl full medium with 1 µg/ml puromycin (puromycin selective medium), and the cells were cultured with the puromycin selective medium for seven days. On the seventh day after stopping the transduction process, successful transduction of the cells was verified by detecting the fluorescent marker mCherry with fluorescence microscopy. The cells were then expanded in order to achieve a satisfactory cell number to cryopreserve the cell lines (Section 2.8) and successful knockdown of GPAM expression was verified by analyzing its expression with quantitative real time-polymerase chain reaction (qRT-PCR) and Western blot (Section 2.16).

2.14 Determination of protein concentration

The determination of the total protein concentration from cellular protein samples was performed using the bicinchoninic acid (BCA) assay (Thermo Fisher Scientific) according to the manufacturer's instructions. This assay is based on two reactions: first, under alkaline conditions, the peptide bonds reduce Cu^{2+} to Cu^{+} and the amount of Cu^{+} produced is proportional to the amount of protein present; second, one Cu^{+} ion chelates with two BCA molecules forming a purple complex that absorbs light at 562 nm and can be used to quantify the protein amount (Smith et al. 1985).

Protein concentrations were determined with a calibration curve of bovine serum albumin (BSA) (0 – 2 mg/ml). The absorbances of the protein samples per sample were measured in technical duplicates at 562 nm in the plate reader infinite M200 Pro (Tecan).

2.15 SDS-PAGE

The procedure is based on the electrophoretic mobility of proteins through a polyacrylamide gel (PAGE). The anionic detergent sodium dodecyl sulfate (SDS) is used to unfold and linearize the proteins and confer them a similar charge-to-mass ratio. Therefore, the proteins are separated in relation to the molecular masses (Laemmli 1970).

For the peptide fragmentation fingerprinting, 20 µl eluate of each sample was heated at 70 ºC for 10 min. Thereafter, the samples were applied to a gradient polyacrylamide gel (4 – 20% Mini-PROTEAN® TGX™ Precast Protein Gels, 10-well, 50 µl, BioRad) in a chamber filled with 1X Tris/Glycine/SDS Buffer (10X) (BioRad). Next, the separation of the protein samples was performed using 20 mA/gel, after which proteins were silver-stained with the Pierce™ Silver Stain for Mass Spectrometry (Thermo Fisher Scientific) according to the manufacturer's instructions.

For Western blotting, 15 µg total protein of each sample was mixed with ultrapure water and loading buffer 4X (BioRad) to a final concentration of 1X and a final volume of 20 µl, and heated at 95 ºC for 5 min. Next, the samples were applied to a discontinuous SDS 10% polyacrylamide gel in a chamber filled with 1X Tris/Glycine/SDS Buffer (10X) (BioRad). Then, the separation of the protein samples was initiated using 20 mA/gel while the samples were in

the stacking gel; and once the migration front reached the separation gel, the current was increased to 25 mA/gel until the gel front was approximately 0.5 cm from the bottom of the gel.

2.16 Gene expression analysis

The mRNA and protein expression of GPAM in the cell lines created in this study with transduction (Table 13) was analyzed using quantitative real time-polymerase chain reaction (qRT-PCR) and Western blot, respectively.

2.16.1 mRNA expression analysis

2.16.1.1 Purification of RNA from mammalian cells

RNA was obtained from the desired cell lines using spin technology (RNeasy Mini kit (Qiagen)) with on-column DNase digestion (RNase-Free DNase Set (Qiagen)). The procedure was performed according to the manufacturer's protocols. Namely, cells in T75 flasks were trypsinized and resuspended in full medium (as explained in Section 2.8). Then, the cell suspensions were pelleted for 5 min at 133g, the supernatants were aspirated, the cell pellets were resuspended in 600 µl Buffer RLT and vortexed for 30 s. The obtained lysates were stored at -80 ºC until continuing with the process.

After thawing the lysates on ice, one volume of 70% ethanol was carefully mixed by pipetting with each lysate until a homogeneous mixture was obtained. The mixtures were then transferred onto RNeasy spin columns in collection tubes and centrifuged for 15 s at 8,000g. The flow-throughs were discarded, and the samples retained in the columns were washed. For the washing, 350 µl Buffer RW1 were added to the spin columns and centrifuged for 15 s at 8,000g, and then the flow-throughs were discarded. Next, the DNase digestion was performed by adding 10 µl DNase I mixed with 70 µl Buffer RDD per sample onto the column and incubating 15 min at room temperature. The RNA samples were then washed once with Buffer RW1 as explained above and thereafter twice with Buffer RPE. For washing with Buffer RPE, 500 µl Buffer RPE were added to the spin columns and centrifuged at 8,000g for 15 s the first time and 2 min the second time, and the flow-throughs were discarded. Then, a centrifugation was performed for 1 min at 8,000g to eliminate any possible carryover. Finally, the RNA samples were eluted in 30 µl RNase-free water, and the concentration determined with a spectrophotometer (NanoDrop One), followed by the synthesis of complementary DNA (cDNA) (Section 2.16.1.2). RNA samples were stored at -80 °C.

2.16.1.2 Synthesis of cDNA

For the mRNA expression analysis, the RNA obtained from the desired cell lines (Section 2.16.1.1) was reverse transcribed to cDNA. The procedure was performed using the High-Capacity cDNA Reverse Transcription Kit (Thermo Fisher Scientific) according to the manufacturer's protocol. Specifically, for each sample, 2 µg RNA sample in 10 µl RNase-free water were mixed with 4.2 µl RNase-free water, 2 µl 10X RT-buffer, 0.8 µl 25X dNTPs, 2 µl 10X random primer and 1 µl reverse transcriptase. The mixtures were vortexed briefly, centrifuged and cDNA prepared using a thermal cycler and the program outlined in Table 16. Once the thermal cycler program was completed, the cDNA samples were diluted with 180 µl diethylpyrocarbonate treated water (Thermo Fisher Scientific) to 0.01 µg/µl and stored at -20 ºC.

Table 16 Thermal cycler program for the reverse transcription reaction.

Settings	**Step 1**	**Step 2**	**Step 3**	**Step 4**
Temperature (ºC)	25	37	85	4
Time (min)	10	120	5	Hold

2.16.1.3 Relative quantification of the mRNA expression

For the mRNA expression analysis, quantitative real time-polymerase chain reaction (qRT-PCR) was used and a relative quantification was performed using the $2^{-\Delta\Delta C_T}$ method (Livak and Schmittgen 2001). The qRT-PCR uses fluorescent reporter molecules to monitor the production of amplification products during each cycle of the PCR reaction. The principle of quantification is based on the fact that the more copies of a target present at the beginning of the assay, the fewer cycles of amplification are required for the fluorescence to reach a threshold level of detection. The C_T value (threshold cycle value) is the fractional cycle where the threshold level of detection is reached (Bustin et al. 2005). The $2^{-\Delta\Delta C_T}$ method (Livak and Schmittgen 2001) provides a calculation of the expression fold change of a target gene between a target sample and a reference sample. In the calculation, an endogenous control, a gene with a constant expression level in all samples, is also used to normalize for variations in cDNA input. Typical endogenous controls are the so-called 'housekeeping genes' such as β-actin or rRNA, the expression of which remains relative stable even when cells are chemically or genetically perturbed. In essence, the method is based on the calculation of the value

$\Delta C_T = C_{T,\text{ target gene}} - C_{T,\text{ endogenous control}}$, then $\Delta\Delta C_T = \Delta C_{T,\text{ target sample}} - \Delta C_{T,\text{ reference sample}}$ and finally fold change = $2^{-\Delta\Delta C_T}$.

The qRT-PCR runs were performed with the QuantiFast® SYBR® Green PCR kit (Qiagen) and QuantiTect Primer Assays (Table 4) on the QuantStudioTM 3 Real-Time PCR System (Applied Biosystems) according to the manufacturer's instructions, measuring all samples with 20 ng cDNA and in technical duplicates. For the application of the $2^{-\Delta\Delta C_T}$ method, the gene *ACTB* was used as the endogenous control and the cell line ES-2_luc shNEG as the reference sample.

2.16.2 Protein expression analysis

2.16.2.1 Extraction of proteins from mammalian cells

Proteins were extracted from the desired cell lines by cell lysis and solubilization of proteins with RIPA buffer. Namely, cells in T75 flasks were trypsinized and resuspended in full medium (as explained in Section 2.8). Then, the cell suspensions were pelleted for 5 min at 133g, the supernatants were aspirated and the cell pellets were resuspended in 200 µl RIPA buffer with 1% protease inhibitor cocktail I (Sigma-Aldrich) and 1% phosphatase inhibitor cocktails II & III (Sigma-Aldrich) and snap frozen in liquid nitrogen. The lysates were stored at -80 ºC until further processing. Finally, the lysates were thawed on ice, vortexed for 5 s and placed on ice for 5 min. Then the lysates were centrifuged at 16,000g for 40 min at 4 ºC. The supernatants were collected into new, pre-cooled 1.5 ml Eppendorf tubes and the protein concentration of these samples was determined by the BCA assay (Section 2.14).

2.16.2.2 Western blot

The extracted proteins (Section 2.16.2.1) were separated by SDS-PAGE (Section 2.15) and transferred onto a PVDF transfer membrane (Thermo Fisher Scientific). For such a procedure, the Trans-Blot® SD semi-dry transfer cell (BioRad) was used according to the manufacturer's instructions. Namely, per SDS polyacrylamide gel, three sheets of extra thick blot paper (BioRad) were soaked in anode buffer and one sheet in cathode buffer. The SDS polyacrylamide gel with the protein samples was equilibrated in cathode buffer. The PVDF membrane was activated by immersion in methanol for 30 s and then equilibrated in the anode buffer. Next, the three sheets soaked in anode buffer were placed on the anode plate. The activated PVDF membrane was placed next, followed by the SDS polyacrylamide gel and the sheet soaked in cathode buffer. The transfer of the proteins onto the PVDF membrane was carried out for

30 min at 230 mA per gel. Thereafter, the membrane was washed in ultrapure water for 5 min with vigorous shaking and shortly stained with Ponceau S solution to confirm the presence of the proteins on the membrane. Finally, the membrane was washed in 1X TBS-T for 10 min with vigorous shaking in order to remove the stain and prepare the membrane for subsequent procedures.

In this study, two proteins were detected, namely GPAM and β-actin (the loading control). For the detection of GPAM, the membrane was blocked in milk blocking solution (5% (w/v) milk powder in 1X TBS-T) for 2 h with gentle shaking at room temperature, followed by an overnight incubation at 4 ºC and gentle shaking with the primary antibody solution (anti-GPAM antibody (sc-398135, Santa Cruz Biotechnology) diluted 1:1,000 in milk blocking solution). On the following day, the membrane was washed thrice with 1X TBS-T for 10 min each continuing with a 2 h incubation at room temperature and gentle shaking with the secondary antibody solution (anti-mouse HRP linked antibody (7076S, Cell Signaling) diluted 1:1,000 in milk blocking solution). Then, the membrane was washed thrice with 1X TBS-T for 10 min each and the detection of GPAM was performed by a chemiluminescence reaction. For such reaction, the membrane was placed into the HRP-dependent substrate solution PURECL™ Dura (Vilber) and after a short incubation, the emitted light was detected with the blot imager Vilber Fusion Fx7 (Vilber). Next, the membrane was washed once with 1X TBS-T for 5 min. If the same membraned needed to be probed again, this was incubated in stripping buffer for 30 min at room temperature with vigorous shaking, and washed thrice with 1X TBS-T for 10 min each. For the detection of β-actin, the membrane was blocked in milk blocking solution for 2 h with gentle shaking at room temperature, followed by a 30 min incubation at room temperature and gentle shaking with the primary antibody solution (anti-β-actin antibody (A2228, Sigma-Aldrich) diluted 1:5,000 in milk blocking solution). Thereafter, the membrane was washed thrice with 1X TBS-T for 10 min each followed by a 20 min incubation at room temperature and gentle shaking with the secondary antibody solution (anti-mouse HRP linked antibody diluted 1:10,000 in milk blocking solution). Then, the membrane was washed thrice with 1X TBS-T for 10 min each and the detection of β-actin was performed by a chemiluminescence reaction as explained above.

2.17 Cytotoxicity analysis of FSG67 in ovarian cells

A cell-viability study of FSG67 with the immortalized ovarian cells HOSE6-3, HOSE17-1 and I64-hTERT, as well as the ovarian cancer cell lines ES-2, OVCAR4 and OVCAR8 was performed to determine the inhibitory concentration (IC) values IC_{20} and IC_{50} of the drug in different cell lines that would help guide drug concentration for subsequent studies. For example, to help to identify concentrations that would elicit an effect on the tested cells, for example cell migration, without affecting viability.

On the day before the experiment, cells were seeded at a cell number that led to 70 – 80% confluency on the day of the experiment. Namely, HOSE6-3, HOSE17-1 and I64-hTERT cells were seeded with $4.5 \cdot 10^4$ cells per well; ES-2 and OVCAR8 cells with $5 \cdot 10^4$ cells per well; and OVCAR4 cells with $7 \cdot 10^4$ cells per well. All cells were plated in 200 µl full medium in a 96-well plate in four technical replicates. On the day of the experiment, different concentrations of the GPAT inhibitor FSG67 (Focus Biomolecules) were prepared (final concentrations of 0.01, 0.0316, 0.1, 0.316, 1, 3.16, and 5 mM) in full medium using the 100% (v/v) DMSO prepared stock solution of 5 M FSG67. Two additional solutions were prepared: a full medium control with no additional components, and full medium with the highest concentration of DMSO used (0.1% (v/v)), in order to verify that DMSO had no effect on the viability of the cells. The media from the cells were removed and 100 µl of the FSG67-containing media or respective controls were added per well in four technical replicates. The cells were incubated under standard cell culture conditions for 24 h and 48 h.

After the 24 h or 48 h incubation, the cell viability was determined with the CellTiter-Blue® assay (Promega). For this assay, the media of the cells were removed and 120 µl full medium supplemented with CellTiter-Blue® reagent (100 µl full medium plus 20 µl CellTiter-Blue® reagent) were added per well. The cells were placed into an incubator under standard cell culture conditions for 1.5 h, when the blue color of the controls changed to pink. Then, 100 µl of the cell media were transferred into a 96-well black microplate (Greiner Bio-One) and the fluorescent signal was measured at $540_{Ex}/590_{Em}$ nm in the plate reader infinite M200 Pro (Tecan). Based on the assumption that the concentration of FSG67 and the cell viability follows a sigmoidal curve, a logistic model was fitted to the data (Section 2.24).

2.18 Cell assays

2.18.1 Wound closure assay

The wound closure assay allows for the study of collective cell migration in vitro. The assay is performed by creating an artificial gap in a monolayer of cells, which depending on the cell line, leads to the cells at the edges of the gap moving towards the opening to close the wound. In this study, the assay was used to test if the GPAT inhibitor FSG67 or silencing GPAM influences collective cell migration.

To test the effect of FSG67 on collective cell migration, the ovarian cancer cells ES-2 and OVCAR8 were seeded at a density of $8 \cdot 10^5$ cells per well in 3 ml full medium in a 6-well plate and incubated until cells were approximately 100% confluent. Once the confluency was reached, two 'wounds' per well were created by scratching the cell monolayer in a straight line with a sterile 10 µl pipette tip. The cells were then carefully rinsed with 1X PBS once to remove cell debris and detached cells, and 3 ml full medium was added per well. At this moment, four fields of the wounds were selected per well and photographed with the microscope BZ-X810 (Keyence). These images were considered as time point 0 h. Next, DMSO (DMSO-only control) or FSG67 were added directly into the culture medium in the wells to the desired final concentrations. Namely, a DMSO working solution was prepared by diluting 100% DMSO to 1% DMSO in full medium. In the same way, a FSG67 working solution was prepared by diluting 1 M FSG67 dissolved in 100% DMSO to 10 mM FSG67 in full medium. For each experiment, the corresponding volume of FSG67 working solution was added directly to obtain the desired final concentration (60, 90, 180 or 270 µM), whereas the corresponding volume of DMSO working solution was added to match the highest concentration of DMSO (0.027% (v/v)) used in the FSG67-treated wells. Plates were placed into the incubator under standard cell culture conditions, and the selected fields were photographed at time points 5 h and 24 h. To examine the effect of silencing GPAM on collective cell migration, a similar procedure was performed as described for FSG67, but in this case using the transduced cell lines ES-2_luc shNEG, ES-2_luc shGPAM1, ES-2_luc shGPAM2 and ES-2_luc shGPAM3; and thus no additional compounds were added after photographing the fields at time point 0 h. Once images were acquired, quantitative data analysis was performed with the software Fiji ((Fiji Is Just) ImageJ 2.16.0/1.54p), measuring the areas of the photographed wounds and calculating the percentage of wound closure normalized to 0 h.

2.18.2 Transwell assay

The transwell assay was used to analyze individual cell migration in vitro. In this assay, cells are placed on the upper layer of a cell culture insert (upper chamber) with a permeable membrane, which is then partially immersed in a solution/media containing a chemoattractant (bottom chamber). Following a predefined incubation period, the cells that migrate through the membrane are quantified. In this study, the assay was used to test if FSG67 or silencing GPAM influences individual cell migration.

For the study of FSG67, the ovarian cancer cells ES-2, OVCAR4 and OVCAR8 were collected and resuspended in serum-free medium (RPMI 1640 (PAN Biotech)). Two cell culture inserts (cell culture inserts 24-well 8.0 µm pore, SABEU) were used per condition, into which $2.5 \cdot 10^4$ (ES-2) or $2 \cdot 10^5$ (OVCAR4 and OVCAR8) cells were seeded in 0.5 ml into the upper chambers of the inserts that were placed in a 24-well plate. In addition, for each condition, two control wells were prepared, into which 0.5 ml of the same cell suspensions were seeded in 1 ml full medium. Then, DMSO (DMSO-only control) or FSG67 were added directly into the upper chambers and the control wells to the desired final concentrations. Specifically, a DMSO working solution was prepared by diluting 100% DMSO to 1% DMSO in serum-free medium. In the same way, a FSG67 working solution was prepared by diluting 1 M FSG67 dissolved in 100% DMSO to 10 mM FSG67 in serum-free medium. The needed volume of FSG67 working solution to obtain the desired final concentration (60 and 90 µM) was added directly into the upper chambers and control wells, while the volume of DMSO working solution was added to match the highest concentration of DMSO (0.009% (v/v)) used in the FSG67-treated chambers and wells. The plates were then placed into the incubator at standard cell culture conditions for 20 min. Thereafter, 600 µl full medium (with 10% FBS used as the chemoattractant) were added to the bottom chambers, and the plates were placed into the incubator at standard cell culture conditions for 24 h to allow cells to migrate through the pores of the membranes. After the 24 h incubation, a cotton swab moistened in 1X PBS was used to clean the inner membranes of the inserts, and migrated cells on the outer membranes were fixed and stained for 20 min at room temperature in 600 µl crystal violet fixation solution (0.5% (w/v) crystal violet, 20% (v/v) methanol in ultrapure water) per membrane. In the meantime, the number of cells in the control wells was determined using the cell counter CASY TT. After fixation and staining, the inserts were washed in tap water and left to dry overnight. Finally, images of four sections of each membrane of the inserts were taken with the microscope BZ-X810 (Keyence), and the software Fiji ((Fiji Is Just) ImageJ 2.16.0/1.54p)

was used to determine the number of cells in each image that was then normalized to the number of cells in the respective control wells. For the study of silencing GPAM, a similar workflow was carried out as for the inhibitor FSG67. Here, the transduced cell lines ES-2_luc shNEG, ES-2_luc shGPAM1, ES-2_luc shGPAM2 and ES-2_luc shGPAM3 were seeded directly into the inserts in serum-free medium, allowed to attach for 20 min, followed by the addition of full medium in the bottom chambers. After 24 h incubation, the cells were removed from the inner chamber, and the cells that migrated through were fixed and stained in crystal violet solution and quantified as described above.

2.18.3 Colony formation assay

The colony formation assay is an in vitro cell survival assay based on the ability of a single cell to grow into a colony, testing the ability of cells to undergo unlimited division. This assay allows for the determination of cell reproductive death in response to a treatment, such as a specific drug or genetic manipulation (Franken et al. 2006). In this study, the assay was used to test if the GPAT inhibitor FSG67 or silencing GPAM influences the formation of colonies.

Two approaches were used to study the influence of FSG67 on colony formation of ES-2, OVCAR4 and OVCAR8 cells. In the first approach, cells were treated at the same time of seeding. Specifically, $2 \cdot 10^2$ cells in 3 ml full medium per well were seeded in technical triplicates into 6-well plates, and DMSO (DMSO-only control) or FSG67 were added directly into the culture medium to the desired final concentrations (0.009% (v/v) DMSO, 60 and 90 µM FSG67) as explained in the previous cell assays. In the second approach, cells were treated with DMSO or FSG67 on the day after seeding. In both approaches, the plates were placed into the incubator under standard cell culture conditions for 11 days (ES-2 and OVCAR8) or 13 days (OVCAR4). Thereafter, the colonies were washed twice with 1X PBS and then fixed and stained for 20 min at room temperature with 1 ml crystal violet fixation solution (0.5% (w/v) crystal violet, 20% (v/v) methanol in ultrapure water) per well. Then, the colonies were washed thrice with tap water and left to dry overnight. Finally, images of each well were taken, and the software Fiji ((Fiji Is Just) ImageJ 2.16.0/1.54p) was used to quantify the number and size of the colonies. The silencing of GPAM in the formation of colonies was studied following a similar workflow, testing the transduced cell lines ES-2_luc shNEG, ES-2_luc shGPAM1, ES-2_luc shGPAM2 and ES-2_luc shGPAM3; without additional treatment, and placing the cells into the incubator for 11 days.

2.18.4 Anoikis assay

In this study, the influence of the GPAT inhibitor FSG67 or silencing GPAM in the resistance against the programmed cell death anoikis was determined. Anoikis is triggered when adherent cells detach from the ECM, and thus cells with the respective treatment were cultured in anchorage resistant plates prepared using the polymer poly(2-hydroxyethyl methacrylate) (pHEMA) that prevents cell adhesion, and the cell viability measured with the CellTiter-Blue® assay (Promega).

First, 10 mg/ml pHEMA solution (95% (v/v) ethanol, 5% (v/v) ultrapure water) was prepared by vigorous shaking at 37 ºC overnight. The solution was then sterilely filtered with a 0.2 µm filter and 750 µl was added per well of 6-well plates to completely coat each well. The plates were partially opened under a sterile hood overnight to dry. Before seeding any cells in the coated plates, the wells were washed once with 1X PBS. For the experiments, $2.5 \cdot 10^5$ cells in 2 ml full medium were seeded into both the pHEMA coated, as well as uncoated 6-well plates that were used as controls. For the characterization of the effect of FSG67 on anoikis cell death, ES-2, OVCAR4 and OVCAR8 cells were treated with DMSO (DMSO-only control) or FSG67 at the desired final concentrations (0.027% (v/v) DMSO, 180 and 270 µM FSG67) at the time of plating, as explained in the previous cell assays. To determine the effect of GPAM silencing, the cell lines ES-2_luc shNEG, ES-2_luc shGPAM1, ES-2_luc shGPAM2 and ES-2_luc shGPAM3 were plated onto the coated and uncoated (control) wells. The plates were placed into the incubator at standard cell culture conditions for 24 h, and on the next day, cell viability was determined with the CellTiter-Blue® assay (Promega). Specifically, 100 µl of the CellTiter-Blue® reagent were added to the wells, and the plates were incubated for 2 h at standard cell culture conditions until the blue color of the reagent changed to pink in the untreated cells as an indicator of viability. Then, 100 µl of the cell media from all wells were transferred into a 96-well black microplate (Greiner Bio-One) and the fluorescent signal measured at $540_{Ex}/590_{Em}$ nm in the plate reader infinite M200 Pro (Tecan).

2.19 Housing conditions of laboratory mice

Laboratory mice (Table 14) were allowed to adapt to their new environment for one week before they were used in experiments. Water and feed was supplied ad libitum, and the mice stayed under pathogen-free conditions in a 12 h day/night rhythm. All animal experiments were performed according to the applications submitted to and approved by the State Agency

for Nature, Environment and Consumer Protection (2025-12 and 2021.A030, Landesamt für Natur, Umwelt und Verbraucherschutz, LANUV, Germany).

2.20 Ovarian cancer cell line-derived xenograft models

Cell line-derived xenograft (CDX) models are preclinical cancer models where human cancer cells are implanted into immunodeficient mice to allow the growth of human tumors without rejection. In this study, ovarian cancer cells (Table 13) were injected intraperitoneally (IP) to evaluate the role of GPAM in ovarian cancer metastasis.

2.20.1 Establishment of peritoneal metastasis models of ovarian cancer cells

The cells ES-2_luc shNEG or ES-2_luc shGPAM1 (Table 13) were cultured (Section 2.8) in T175 flasks until approximately 80% confluency on the injection day. Prior to the injection, the cells were trypsinized as explained in Section 2.8 followed by the determination of the cell concentration with the cell counter CASY TT. Then, the cell suspension was centrifuged at 133g for 5 min, and the cell pellet was resuspended in the corresponding volume of 1X PBS to prepare a cell suspension of $5 \cdot 10^7$ cells/ml, which was kept on ice until the moment of the injection.

For each mouse, 100 µl containing $5 \cdot 10^6$ cells were injected intraperitoneally (IP) with a 30G syringe needle into female CD-1 nude mice. One hundred µl of cells that were passed through the syringe needle were also plated into a well of a 6-well plate and observed the next day to ensure that they were viable. Mice were observed daily and monitored using the previously approved scoresheets, evaluating aspects such as weight loss, body circumference or abnormal behavior. Bioluminescence signal in the mice was measured once a week in the IVIS Spectrum in vivo imaging system (Revvity) (Section 2.20.2), until the end of the experiment, when mice were sacrificed and internal organs were analyzed to evaluate metastasis formation (Section 2.20.3).

2.20.2 In vivo imaging of the models

Since the used cells were luciferase-expressing cells, D-luciferin potassium salt (Revvity) and the IVIS Spectrum in vivo imaging system (Revvity) were used to perform non-invasive bioluminescence imaging of the established peritoneal metastasis models. Luciferin solution was prepared freshly prior to the imaging dissolving D-luciferin potassium salt in 1X PBS at a

concentration of 15 mg/ml, and sterilely filtered using a 0.2 µm filter. For imaging, luciferin solution was injected at 10 µl/g body weight IP into mice with a 30G syringe. After 10 min to allow complete distribution of the luciferin in mice, the bioluminescence signal was acquired. Specifically, the mice were anesthetized three minutes before the imaging with a mixture of isoflurane in oxygen (2.5% (v/v) at a flow rate of 1 l/min). Then, the mice were placed in supine position in the IVIS Spectrum in vivo imaging system and the bioluminescence signal was measured. Data acquisition and processing were performed with the software Living Image® version 4.7.2 (Revvity).

2.20.3 Ex vivo imaging of the models

Eight weeks after IP injection of the cells, internal organs of the CDX models were analyzed to determine the spread of metastasis. First, physical euthanasia of the mice was performed by cervical dislocation. Then, the abdominal cavity was opened, and the internal organs (liver, kidney, spleen, diaphragm, stomach, intestines, fat pad, omentum, lungs and pancreas) were removed, washed once in 1X PBS and placed on a black non-reflecting Lexan foil. The mentioned collection of organs was placed in the IVIS Spectrum in vivo imaging system and the bioluminescence signal was measured approximately 20 min after the luciferin injection as beforehand explained (Section 2.20.2). The organs were snap frozen in liquid nitrogen for later analyses.

2.21 Toxicology and pharmacokinetic studies of FSG67 in vivo

To identify the concentration of FSG67 that would be applicable for in vivo antitumor efficacy and metastases studies, as well as to determine FSG67 blood concentration over time, maximum tolerated dose (MTD) and pharmacokinetic properties of FSG67 were studied in vivo. For the MTD study, female CD-1 mice (Table 14) were treated IP with either vehicle (5% DMSO, 40% PEG400, 5% Tween80, 50% PBS) or increasing doses of FSG67, starting with a dose of 10 mg/kg. The dose was increased by 10 mg/kg every 3 – 4 days until signs of toxicity were observed in the mice, and then the prior dose to the one that induced signs of toxicity was used for subsequent analyses. In the next step, a repeated dose toxicity (RDT) was performed, where the toxicological profile of FSG67 following repeated administrations was determined. Namely, female CD-1 mice (Table 14) were treated with either vehicle (5% DMSO, 40% PEG400, 5% Tween80, 50% PBS) or the previously determined dose of FSG67 IP for two weeks, five days on and two days off. Finally, a pharmacokinetic study of FSG67

was performed. For such a procedure, female CD-1 mice (Table 14) were treated IP with the selected dose of FSG67, and blood samples were collected after treatment at 5 min, 15 min, 30 min, 60 min, 90 min, 2 h, 4 h, 6 h and 24 h, in EDTA-containing tubes and centrifuged at 13,000g for 10 min at 4 ºC to separate the blood plasma, which was stored at -80 ºC until analysis by LC-MS/MS (Section 2.21.1).

2.21.1 Determination of the concentration of FSG67 in blood plasma

The determination of the concentration of FSG67 in blood plasma was performed by Dr. Anke Unger at the Lead Discovery Center GmbH (LDC). FSG67 was extracted from the blood plasma by protein precipitation. A volume of 80 µl of acetonitrile containing 0.1 µM griseofulvin as internal standard were added to 20 µl of blood plasma and mixed well. The samples were filtered through 0.45 µm filter plates, diluted with water and transferred to LC-MS/MS analysis. If necessary, samples were diluted prior to analysis using blank matrix to fall within the calibration range. Samples were analyzed using a Shimadzu Prominence UFLC system coupled to a Sciex QTrap 5500 instrument. Data acquisition and peak processing was performed using Analyst 1.6.2 software. FSG67 was separated using an Agilent Poroshell 120 EC (2.1 x 50 mm) column. Separation was achieved using a generic gradient starting from 5% B and increasing to 100% B over 1 min of solvents A (0.1% formic acid) and B (0.1% formic acid in acetonitrile) at a flow rate of 1.0 ml/min. MS instrument settings were automatically tuned and optimized prior to analysis. Ionization of FSG67 was achieved by electrospray ionization (ESI) in positive mode and FSG67 was detected in multiple reaction monitoring (MRM) mode using a specific precursor-to-product ion transition (m/z 326.193 → 281.900).

For quantification, a calibration curve using blank mouse blood plasma with spiked analyte concentrations of 0.0003 to 1.11 µM was established. Curve fitting and calculation of unknown sample concentrations was performed based on peak area ratios. Quality control samples covering the low, medium and high concentration range were included (deviation from nominal concentration < 20%). An overall recovery of the analyte of > 80% was achieved.

2.22 Trace of labeled LPA molecules

Three different approaches were used to study the localization of LPA in ovarian cancer cells. One approach was based on the use of fluorescently-labeled LPA and fluorescent microscopy. In this approach, the day before the experiment, COV318 cells were seeded at a density of

$7 \cdot 10^4$ cells per well in 1 ml full medium in a 24-well plate. On the day of the experiment, the cells were washed once with 1X PBS and starved by incubating in 0.5 ml serum-free medium (RPMI 1640 (PAN Biotech)) for 1 h using standard cell culture conditions. At the end of the incubation time, one field per well was selected and photographed with the microscope BZ-X810 (Keyence), which was labeled as time point 0 h. Next, the cells were incubated for 1 h at standard cell culture conditions in 550 µl transfection media. The transfection media were prepared as follows: in an Eppendorf tube, 2.5 µl Lipofectamine™ 3000 Reagent (Thermo Fisher Scientific) was added to 60 µl Gibco™ Opti-MEM™ I Reduced Serum Medium (Thermo Fisher Scientific). In another Eppendorf tube, 5 µl P3000™ Reagent were mixed with the fluorescent LPA TopFluor® Lyso PA (Avanti Research) and Opti-MEM™ I Reduced Serum Medium to a final volume of 62.5 µl and the desired final concentration (0 – 40 µM) of fluorescent LPA. Next, the mixture from the second tube was added to the first tube and this final mixture was incubated at room temperature for 12 min. Then, 50 µl of the mixture was added to 500 µl RPMI 1640, obtaining the 550 µl transfection media. Additionally, the same transfection media were prepared without Lipofectamine™ 3000 Reagent or P3000™ Reagent, substituting the respective volumes using Opti-MEM™ I Reduced Serum Medium. After the 1 h incubation, the cells were washed once with 1X PBS followed by the addition of 500 µl RPMI 1640 and 50 µl Opti-MEM™ I Reduced Serum Medium to each well, which were imaged again with the microscope BZ-X810 (Keyence).

The second approach involved the use of ^{13}C-labeled LPA and mass spectrometry. The mass spectrometry procedure was performed by Dr. Jörg Reinders and colleagues at the Bioanalytics department at Institut für Arbeitsforschung an der TU Dortmund (IfADo), which functions as a core facility that supports in-house research projects. The day before the experiment, COV318 cells were seeded at a density of $1.3 \cdot 10^5$ cells per well in 1 ml full medium in a 12-well plate. On the day of the experiment, the cells were washed with 1X PBS and starved by incubating the cells for 1 h in 1 ml serum-free medium (RPMI 1640) at standard cell culture conditions. After the 1 h incubation time, the media were replaced by RPMI 1640 containing 40 µM 16:0 LPA (U-13C) (Avanti Research) (^{13}C-LPA) and the cells were incubated for 1 h at standard cell culture conditions, after which they were washed thrice with 1X PBS, followed by the addition of 1 ml RPMI 1640 per well and incubation for 2 h at standard cell culture conditions. Next, media and cell samples were extracted using 80% methanol containing 100 nM 17:1 LPA. After centrifugation, 10 µl of the supernatant was injected into the LC-MS/MS-system consisting of an QExactive mass spectrometer coupled to a Vanquish Horizon

UHPLC. Samples were separated isocratically with 40% solvent B (A: 5 mM ammonium carboxylic acid, 0.1% formic acid in 50% methanol; B: acetonitrile) on a Nucleodur HILIC, 125 x 3 mm, 3 µm column (Macherey-Nagel) for 14 min. The mass spectrometer operated in Full-MS mode with a resolution of 140,000. Quantification was accomplished using Skyline Daily (version 24.1.1) against a calibration curve from 0 – 10 nM.

A third approach used 1-palmitoyl-d_9 lysophosphatidic acid (Cayman Chemical) (d-LPA) together with the high-speed imaging CARS microscopy (Section 2.22.1). In this approach, the day before the experiment, $7 \cdot 10^5$ cells COV318 cells were seeded in a 35 mm glass bottom microwell dish (MatTek). On the day of the experiment, the cells were washed once with pre-warmed (37 ºC) PBS, followed by the addition of 500 µl pre-warmed PBS to each well which were imaged as explained in Section 2.22.1. Then, d-LPA was added to the cells at a final concentration of 100 µM in a final volume of 1 ml pre-warmed PBS, and the cells were imaged again for 30 min as explained in Section 2.22.1.

2.22.1 Coherent anti-Stokes Raman scattering spectroscopy (CARS) imaging

CARS is based on the Raman effect, an inelastic scattering of photons by matter (Raman and Krishnan 1928). When a monochromatic light interacts with matter there is a change in the direction and energy of the light, resulting in the energy of the light being lower (Stokes shift) or higher (anti-Stokes shift) (Jones et al. 2019). This effect can be applied in spectroscopy (Raman spectroscopy) as well as in microscopy (Raman microscopy) (Jones et al. 2019). Raman signals can be used to observe specific endogenous biomolecules. Nevertheless, the signal of one biomolecule may overlap with the signal of another biomolecule (Egoshi, Dodo, and Sodeoka 2022). To overcome these limitations, specific groups can be used which produce Raman signals that are not present in the biological samples, such as carbon-deuterium bonds (Egoshi, Dodo, and Sodeoka 2022). Thus, 1-palmitoyl-d_9 lysophosphatidic acid (Cayman Chemical) (d-LPA) together with the high-speed imaging CARS microscopy were used to image intracellular LPA.

The determination of the optimal Raman shift of d-LPA for CARS imaging was performed on a Raman microscope WITec alpha300 R (Oxford Instruments) with a Zeiss EC Epiplan-Neofluar 10x magnification objective. The laser excitation wavelength was 532 nm, and ten accumulations were performed with an integration time of 5 s. Raman data acquisition and processing were carried out with the software WITec Project 6.0.

CARS imaging was performed using a confocal laser scanning microscope TCS SP8 (Leica Microsystems GmbH) with a picoEmerald IR laser system (APE GmbH) and an IR optimized 40x objective with a NA of 1.1; together with Dr. Nachiket Vartak from the Bioimaging group at IfADo. The IR laser was configured to 0.5 W on both lasers at 80% output power. Cells with d-LPA were imaged at 2104 cm^{-1}. Data processing was performed with the software Fiji ((Fiji Is Just) ImageJ 2.16.0/1.54p).

2.23 Study of LPA-binding proteins

2.23.1 LPA-protein pull-down

Two types of protein solutions were pulled down in this study. Cell lysate protein solutions were pulled down to identify LPA-binding proteins. To obtain these solutions, after cell culture and trypsinization (Section 2.8) cell suspensions were divided equally into two tubes and washed twice by two cycles of centrifugation at 133g for 5 min in cold 1X PBS. Thereafter, the cells were resuspended in 1 ml lysis/binding buffer (10% (v/v) glycerol, 100 mM NaCl, 1% (v/v) Triton X-100, 1% Protease-/Phosphatase-Inhibitor-Cocktail, 1 mM DTT, 20 mM Tris-HCl, pH 7.4) and the tubes rotated for 30 min at 4 ºC to facilitate cell lysis. The lysates were then centrifuged at 16,000g for 20 min at 4 ºC to remove cell debris (pellet), and the supernatants collected into new, pre-cooled 1.5 ml Eppendorf tubes. Protein concentrations were determined using the BCA assay (Section 2.14) and adjusted to a final concentration of 1 µg/µl in a final volume of 1 ml. Additionally, anti-LPA antibody solutions were pulled down as a control of the LPA-protein pull-down. These solutions were prepared by diluting 0.5 µl of anti-LPA antibody (Z-P200, Echelon Biosciences) in 2 ml lysis/binding buffer.

Beads were washed and equilibrated before performing the actual pull-downs. For such a procedure, 40 µl control agarose beads (Echelon Biosciences) and 40 µl LPA-coated agarose beads (Echelon Biosciences) were centrifuged at 500g for 1 min at 4 ºC and washed thrice in lysis/binding buffer. For the washing steps, the beads were resuspended in 1 ml lysis/binding buffer, rotated at 4 ºC for 1.5 min, followed by another centrifugation step at 500g for 1 min at 4 ºC. Thereafter, the actual pull-downs were performed. For the pull-downs, one half of the anti-LPA antibody solution was mixed with control agarose beads, while the other half was mixed with LPA-coated agarose beads. The 1 ml cell lysate protein solutions were mixed directly with control and LPA-coated agarose beads. These solutions were incubated at 4 ºC for 1.5 h in rotation, and then centrifuged at 500g for 1 min at 4 ºC. The centrifuged beads were

then washed five times with wash buffer (150 mM NaCl, 0.5% (v/v) Tween 20, 20 mM MES-NaOH, pH 7.4). For the washing steps, 1 ml wash buffer was added to each centrifuged bead pellet, followed by rotation at 4 ºC for 1.5 min, centrifugation at 500g for 1 min at 4 ºC and removal of the supernatants. After washing, the proteins were eluted by incubating the beads at 70 ºC for 10 min in either loading buffer (BioRad) for the peptide fragmentation fingerprinting (Section 2.23.2) or in 10 mM Tris, 1% (w/v) SDS, pH 7.8 for the sequential window acquisition of all theoretical fragment ion mass spectra (SWATH-MS) (Section 2.23.3), followed by a centrifugation at 500g for 1 min to remove the beads (pellet). Finally, the supernatants were collected into new Eppendorf tubes for the subsequent experiments.

2.23.2 Peptide fragmentation fingerprinting

Proteins were identified by querying the profile of their fragmented peptides against a database, so called peptide fragmentation fingerprinting, by Dr. Jörg Reinders and colleagues at the Bioanalytics department at Institut für Arbeitsforschung an der TU Dortmund (IfADo). For such a procedure, after SDS-PAGE separation, staining (Section 2.15) and excision from the gel of the protein bands to be analyzed, protein-band gel pieces were washed first in 100 µl of 50 mM ammonium bicarbonate (pH 7.8) followed by 25 mM ammonium bicarbonate in 50% acetonitrile to remove small molecule compounds. Afterwards, the gel pieces were dried in a vacuum centrifuge and rehydrated using 20 µl 50 mM ammonium bicarbonate buffer containing 12.5 ng/µl sequencing grade trypsin (Serva GmbH). After an overnight incubation at 37 °C, the resulting peptides were eluted by the addition of 25 µl 5% formic acid and incubated for 15 min at room temperature under constant shaking. Finally, 15 µl of the supernatant were used for the LC-MS/MS analysis.

Samples were injected into the LC-MS/MS system Ultimate 3000RS UHPLC coupled to a Sciex TripleTOF6600+ mass spectrometer. Peptides were separated on a 150 µm x 100 mm Waters nanoEase M/Z HSS C18 T3, 100 Å, 1.8 µm column with precolumn concentration on a 180 µm x 5 mm Waters nanoEase M/Z Symmetry C18, 100 Å, 5 µm precolumn (flow rate 20 µl/min; 0.1% trifluoroacetic acid) at 40 °C. Elution was performed at a flow rate of 2 µl/min using a binary gradient (solvent A: 0.1% formic acid; solvent B: 0.1% formic acid in acetonitrile) from 3% to 25% B, 25% to 50% B followed by a washing step at 90% B and re-equilibration of the column for a total run time of 45 min. The mass spectrometer was operated in information-dependent mode using a TOP50 method with a 25 ms Full-MS-scan and up

to 50 dependent MS/MS-scans of 40 ms each. Resulting files were searched against the Uniprot database using Protein Pilot (version 5.0.3).

2.23.3 SWATH-MS

Proteins were also identified by the sequential window acquisition of all theoretical fragment ion mass spectra (SWATH-MS) by Dr. Jörg Reinders and colleagues at the Bioanalytics department at IfADo. First, proteins (from Section 2.23.1) were digested. For such a procedure, the proteins were precipitated using 80% methanol and pelleted by 5 min centrifugation at 21,000g at 4 °C. The pellet was resuspended in 1% SDS/50 mM Tris-HCl, pH 7.8 and protein concentrations were determined with the ServaPurple Protein Quantification assay (SERVA GmbH). The resulting samples were diluted to 0.25 µg/µl using 6 M urea in ammonium bicarbonate buffer (50 mM, pH 7.8) and 200 µl were subjected to an overnight, automated filter aided sample preparation (FASP) tryptic protein digest on a Nimbus pipetting robot (Hamilton) equipped with a MPE2 positive pressure filtering device. During the robotic program, disulfide bonds were reduced by the addition of 10 µl 100 mM dithiothreitol followed by an incubation for 15 min at 37 °C. Blocking of the free thiols was accomplished by adding 10 µl 250 mM iodoacetamide and incubation for another 15 min. Afterwards, the samples were transferred to a 30,000 kDa-ultrafiltration 96-well plate (AcroPrep, 300 µl, Omega membrane, Pall Corporation) and filtered for 15 min using a pressure of 15 psi. Samples were subsequently washed thrice with 200 µl each of 6 M urea in ammonium bicarbonate buffer (50 mM, pH 7.8) using the same filtering settings. Thereafter, the samples were washed an additional three times with 200 µl ammonium bicarbonate buffer, followed by the addition of 195 µl ammonium bicarbonate buffer and 10 µl trypsin solution (0.1 µg/µl in 1 mM HCl) and the tryptic digestion was conducted for 6 h at 37 °C with constant shaking. Digestion of the proteins was stopped by adding of 10 µl 5% formic acid and samples were filtered. The eluent was transferred to a 96-deep-well-plate and stored at 4 °C until the end of the program. Finally, 15 µl of the resulting 200 µl peptide solutions were used for the LC-MS/MS analysis as described previously, with a binary gradient (solvent A: 0.1% formic acid; solvent B: 0.1% formic acid in acetonitrile) from 3% to 25% B in 66 min, 25% to 50% B in 15 min followed by a washing step at 90% B and re-equilibration of the column for a total run time of 95 min. Each sample was injected twice as the mass spectrometer operated in SWATH-MS-mode with gas-phase fractionation using two fractions (m/z 400 – 600 and 600 – 1,000) with each 60 SWATH-windows of variable size with 250 ms for the Full-MS-scan and 40 ms per SWATH-window. Spectral data of the analyzed peptides were searched and quantified using

Skyline Daily (version 24.1.1) and only proteotypic peptides of ID-confidence ≥ 95% with dotp-values ≥ 0.9 and q-value ≤ 0.01 were used for quantification. Proteins with less than two different peptides were excluded.

2.24 Statistical analysis

If not mentioned, three or more biological replicates were carried out. Analyses were performed with the software GraphPad Prism (version 10) and OriginPro 2025 (version 10.2.0.196). Data are presented as the mean value with standard deviation or with box plots with whiskers from the minimal to maximal value. An unpaired t-test or ANOVA followed by post hoc analysis were used to determine significant difference between conditions, and $p < 0.05$ was considered significant. The statistical significance is represented as: *, $p < 0.05$; **, $p < 0.01$; ***, $p < 0.001$ and ****, $p < 0.0001$. The built-in logistic function was used to analyze the cytotoxicity data, fitting the data to a four-parameter logistic model and providing the inhibitory concentration (IC) values as well as the coefficient of determination R^2, which was used to evaluate the goodness of fit of the model.

3 Results

3.1 Generation of luciferase-expressing ES-2 cell lines

To study the effect of GPAM silencing on metastasis in vivo, a peritoneal metastasis model was chosen, in which ovarian cancer cells are injected intraperitoneally (IP) into mice, and the developing tumors monitored non-invasively. This non-invasive detection is accomplished by injecting cells stably transfected with a luciferase-expressing system that generates bioluminescence upon the administration of luciferin, which is oxidized by luciferase to generate light (de Wet et al. 1987). The emitted light is then measured by the IVIS Spectrum in vivo imaging system.

The ovarian cancer cell line ES-2 was chosen for the model due to its aggressive phenotype and ability to form metastatic tumors (Ying et al. 2023). Prior to transfecting the cells with the plasmid pGL4.51[luc2/CMV/Neo], which encodes the firefly luciferase gene *luc2*, an antibiotic kill curve experiment was performed with the antibiotic geneticin disulfate (G418) to identify a concentration that led to complete loss of viability of the parental ES-2 cells and which could be used to select for the successfully transfected cells that express the neomycin (Neo) resistant gene. After seven days of treatment, 300 µg/ml G418 was identified as the optimal concentration and was subsequently used to select ES-2 cells that were successfully transfected with the plasmid pGL4.51[luc2/CMV/Neo]. Finally, single cell cloning was performed in order to pick luciferase-expressing cell lines with a uniform genetic background and high luciferase activity.

Three clones were selected and propagated for further analyses, named ES-2_luc_c1, ES-2_luc_c2 and ES-2_luc_c3. To identify which of the three had the highest luciferase activity for subsequent experiments, the ONE-Glo^{TM} Luciferase Assay System (Promega) was used to measure their luminescence. As expected, the parental cell line ES-2 did not produce luminescence and while the three ES-2 clones all successfully produced luminescence signals, they were quite variable (Figure 6). ES-2_luc_c2 produced a very weak signal compared to ES-2_luc_c1 and ES-2_luc_c3, with the latter exhibiting the highest luminescence signal (approximately two-fold higher than that produced by ES-2_luc_c1) and was thus selected for further experiments and renamed ES-2_luc.

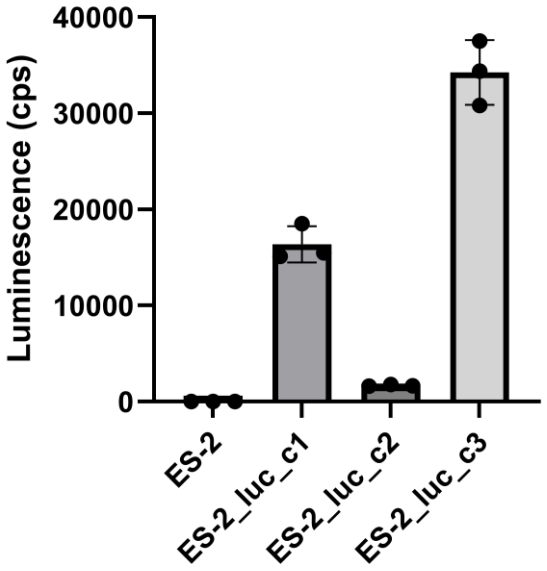

Figure 6 Successful production of luciferase-expressing ES-2 cell lines. ES-2 cells were stably transfected with the pGL4.51[luc2/CMV/Neo] plasmid, and single cell cloning performed after selecting successfully transfected cells with the antibiotic geneticin disulfate (G418). Luciferase activity was measured in three selected ES-2_luc clones (ES-2_luc_c1, ES-2_luc_c2 and ES-2_luc_c3) as well as in the parental cell line ES-2, which was used as a negative control. The ONE-Glo^{TM} reagent was added directly into the cell media and mixed by pipetting with the cells and media. The mixture was left for 3 min at room temperature to allow complete cell lysis, followed by the determination of the luminescence with the plate reader infinite M200 Pro (Tecan). Data is presented as the mean value ± standard deviation of three technical replicates and given as counts per second (cps).

3.2 Generation of stable GPAM knockdown ES-2 cell lines

A main objective of this PhD thesis was to determine the effect of silencing GPAM on metastasis in vivo. Thus, a stable system was first needed that allows for the permanent silencing of the expression of GPAM in cells. The chosen system was a lentiviral short hairpin RNA (shRNA) knockdown vector (VectorBuilder), which uses lentiviral delivery to integrate an shRNA cassette targeting the desired gene into the host cell genome. In the selected system, the shRNA is under the control of a constitutive promoter, and the transcription of the shRNA elicits the RNA interference response against the targeted gene (Stewart et al. 2003).

To create ES-2 cells in which GPAM is stably silenced, the previously generated ES-2_luc cell line was transduced with three different lentiviral shRNA vectors targeting different exons of *GPAM*, here named ES-2_luc shGPAM1, ES-2_luc shGPAM2 and ES-2_luc shGPAM3 (Table 13) as well as a non-targeting scrambled shRNA used as a negative control (ES-2_luc shNEG). To ensure that the transduction process was successful, ES-2_luc cells were transduced with multiplicities of infection (MOI) of three, five and eight. The transduction was stopped after one day by removing the transduction media and replacing with full

medium. The successfully transduced cells were then selected by culturing the cells for seven days with full medium containing 1 µg/ml puromycin (Marchan et al. 2017), and confirmed by detecting the fluorescent marker mCherry with fluorescence microscopy (Figure 7). As anticipated, no fluorescence signal was detected in the untransduced cells (negative control; Figure 7, top panel); while the cells transduced with the different lentiviral vectors all fluoresced red (Figure 7, lower panels). The ES-2_luc shGPAM2 cells exhibited the lowest signal among all cell lines but was nevertheless selected for further analyses because at least 70% of the cells fluoresced red. The transduced cell lines were then expanded for cryopreservation and subsequent analyses that included confirmation of the GPAM knockdown and effect on cellular processes.

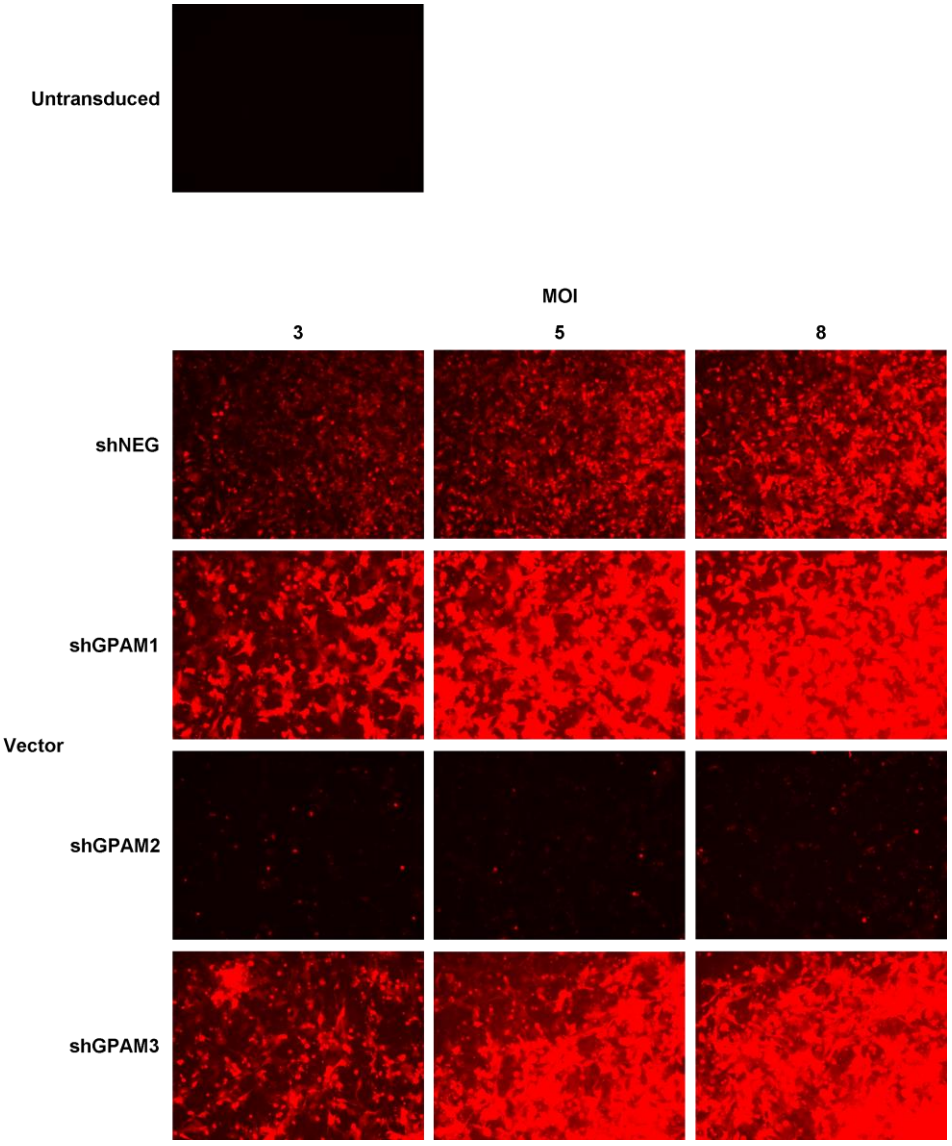

Figure 7 Fluorescence microscopy verified the successful transduction of ES-2_luc cells with different shRNA lentiviral vectors. ES-2_luc cells were transduced with multiplicities of infection (MOI) of three, five and eight and selected with 1 µg/ml puromycin for seven days. The top image is the untransduced ES-2_luc cells.

To confirm reduced GPAM expression in the cells transduced with GPAM shRNA compared to shNEG cells, mRNA and protein expression analyses were performed using quantitative real time-polymerase chain reaction (qRT-PCR) and Western blot, respectively. The cells which grew at similar rates were selected for subsequent experiments, which were ES-2_luc shNEG MOI 3, ES-2_luc shGPAM1 MOI 3, ES-2_luc shGPAM2 MOI 5 and ES-2_luc shGPAM3 MOI 3, and renamed ES-2_luc shNEG, ES-2_luc shGPAM1, ES-2_luc shGPAM2 and ES-2_luc shGPAM3 respectively. Gene expression analysis with qRT-PCR revealed a statistically significant decrease in *GPAM* mRNA expression in all three shGPAM cell lines compared to the shNEG control (Figure 8A), from approximately 90% downregulation with shGPAM1 to 75% with shGPAM3. Similar results were also observed on the protein level (Figure 8B). In summary, ES-2 cells with a stable GPAM silencing were successfully created using three shRNA oligos targeting different exons of the gene.

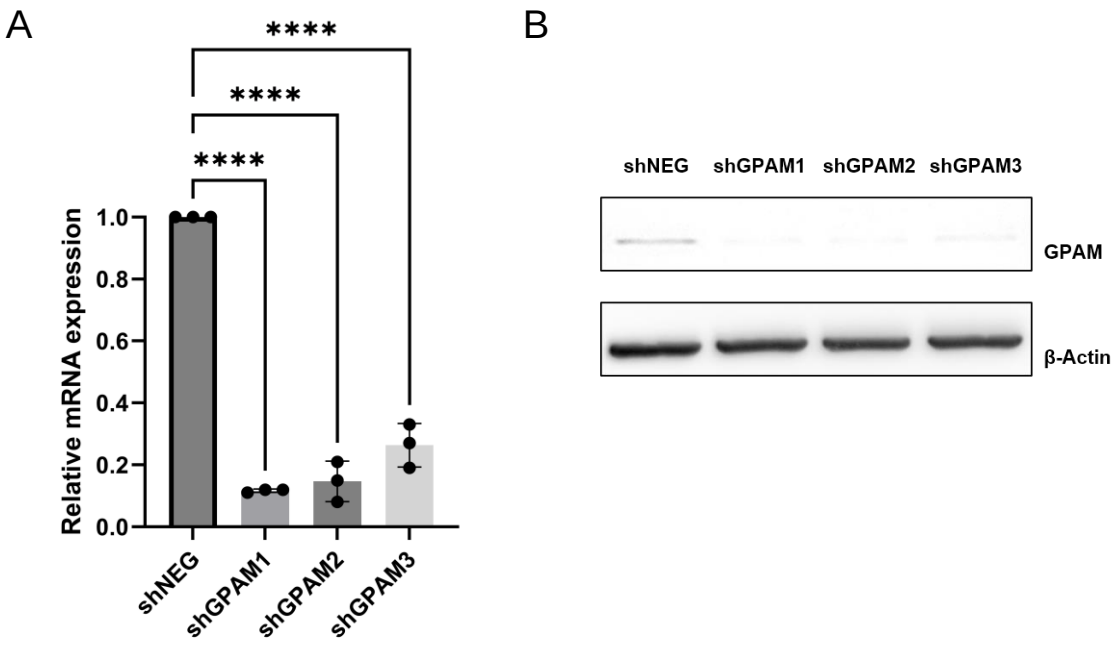

Figure 8 Gene and protein expression analysis verified the successful knockdown of GPAM. A) Relative mRNA expression of *GPAM* in the cell lines ES-2_luc shGPAM1, ES-2_luc shGPAM2 and ES-2_luc shGPAM3 compared to the control ES-2_luc shNEG. *ACTB* was used as the endogenous control. Data is presented as the mean value with the standard deviation from three biological replicates, and each biological replicate was performed in technical duplicates. B) Representative Western blot of three biological replicates of GPAM protein expression in the cell lines ES-2_luc shNEG, ES-2_luc shGPAM1, ES-2_luc shGPAM2 and ES-2_luc shGPAM3. β-Actin was used as loading control. ****, $p < 0.0001$.

3.3 Stably knocking down GPAM inhibits cancer-relevant processes in vitro

After confirming the knockdown of GPAM in the ES-2 cells, the effect of GPAM knockdown on cellular phenotypes important in cancer development and metastasis was investigated.

3.3.1 Stable GPAM knockdown reduces collective cell migration

Collective cell migration refers to the movement of cells as a collective unit, and is regulated by the interaction of these cells with one another and their environment to guide direction and behavior (Rorth 2009). Many ‘normal’ cells migrate collectively under physiological conditions; a characteristic that is also often observed in invading tumor cells (Rorth 2009). Thus, the effect of knocking down GPAM on collective cell migration was studied using the wound closure assay (Section 2.18.1). Briefly, ES-2 GPAM knockdown and control cells were seeded and incubated at standard cell culture conditions until the cells formed a confluent monolayer. Then, two artificial gaps were created (‘wounds’), and time-lapse microscopy was performed to evaluate the wound closure after 24 h.

The ES-2_luc shNEG cell line completely closed the wound after 24 h; however, those created in the ES-2_luc shGPAM1, ES-2_luc shGPAM2, ES-2_luc shGPAM3 cell lines were not completely closed, still leaving small apertures (Figure 9A). Additionally, quantification analyses revealed that ES-2_luc shGPAM1 and ES-2_luc shGPAM3 showed a significantly reduced wound closure compared to the control ES-2_luc shNEG (Figure 9B), that were both approximately 20% less closed than the control. Taken together, silencing GPAM slowed migration of the studied ES-2 cells, showing a small but significant effect in two out of three cell lines tested.

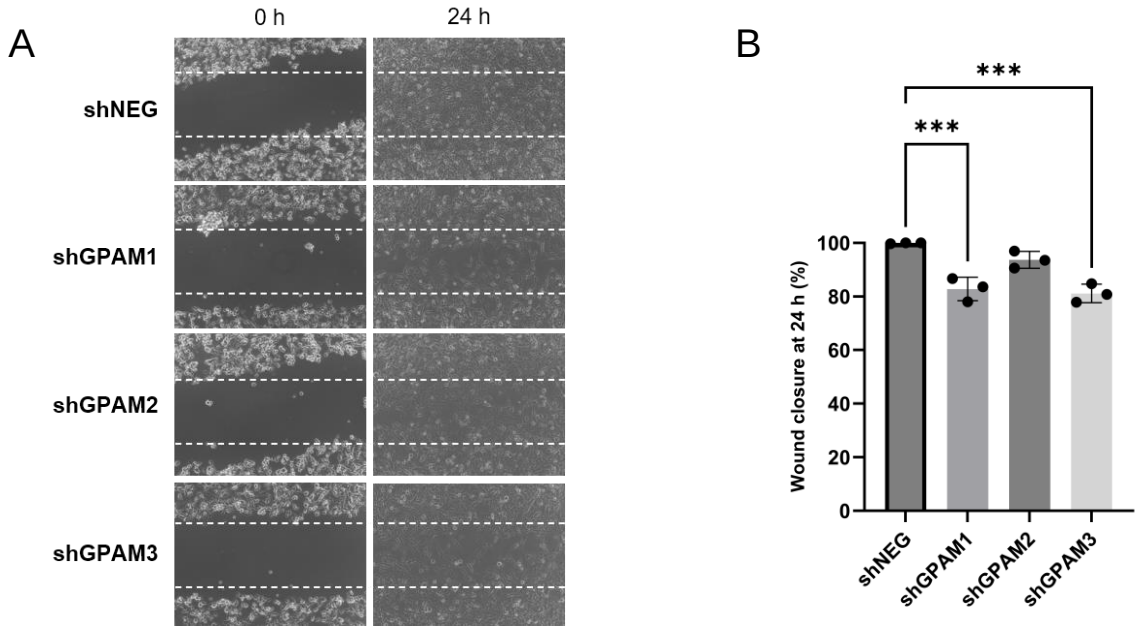

Figure 9 Stable knockdown of GPAM reduces collective cell migration. A) Representative phase contrast microscopy images of the ovarian cancer cell lines ES-2_luc shNEG, ES-2_luc shGPAM1, ES-2_luc shGPAM2 and ES-2_luc shGPAM3 at the time of creating the wound (0 h) and 24 h later. B) Quantification of the wound closure after 24 h, measured as the percentage of wound closure compared to the respective initial wound. Data is presented as the mean value with the standard deviation from three biological replicates, and each biological replicate was performed in four technical replicates. ***, $p < 0.001$.

3.3.2 Stable GPAM knockdown does not significantly influence individual cell migration

Another important feature of cancer cells is their ability to move as a single cell (individual cell migration), which is particularly relevant during detachment, invasion and metastasis (Friedl and Wolf 2003). Therefore, the transwell assay (Section 2.18.2) was used to evaluate the impact of the knockdown of GPAM on individual cell migration. For this assay, ES-2_luc shNEG, ES-2_luc shGPAM1, ES-2_luc shGPAM2 and ES-2_luc shGPAM3 were resuspended in serum-free medium, transferred to the upper chamber of the transwell and their migration through the pores to the underside of the membrane towards full medium with 10% FBS in the bottom chamber was measured after 24 h. The migrated cells were fixed and stained with crystal violet fixation solution and finally quantified.

Representative microscopic images of the fixed cells on the membranes indicate that there was no obvious difference in individual cell migration between the control shNEG and any of the shGPAM knockdown cell lines (Figure 10A). This observation was substantiated by the quantification, which revealed that despite an on average 30% reduction in migration in all

shGPAM cell lines compared to the control (Figure 10B), the change was not statistically significant, maybe due to the variability among the biological replicates in the knockdown cell lines. In conclusion, silencing GPAM seems not to have a strong influence on individual cell migration in the studied ovarian cancer cell line.

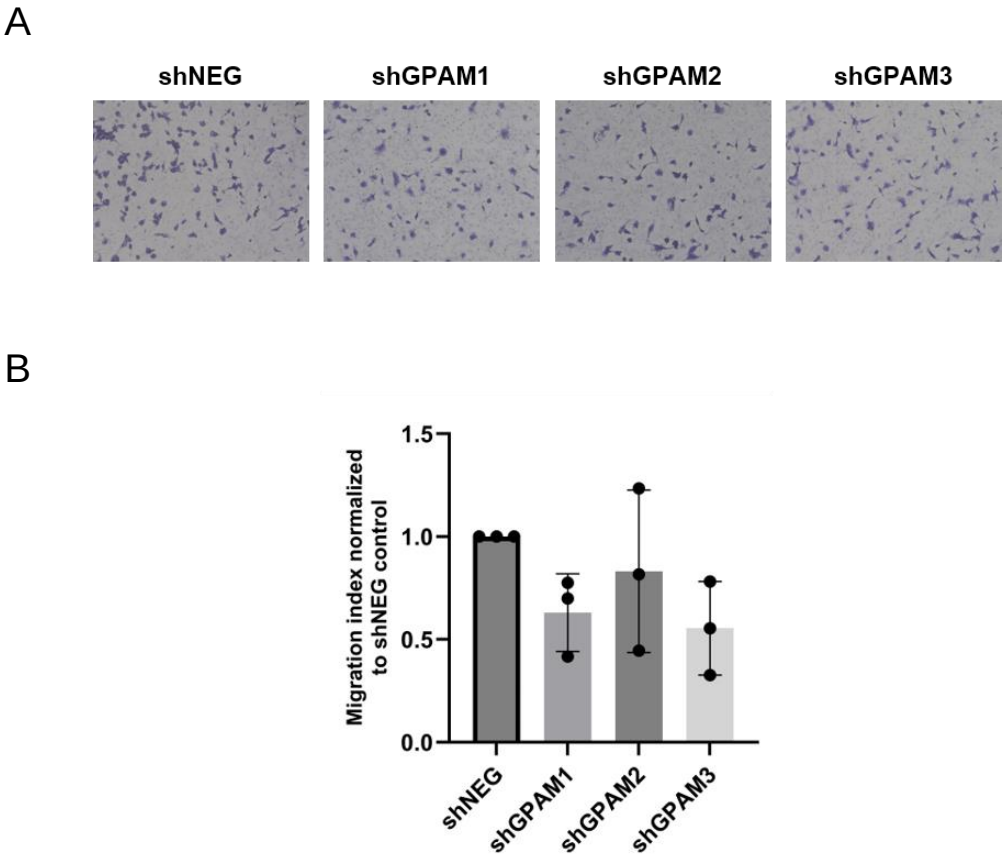

Figure 10 Stable knockdown of GPAM in ES-2 cells does not have a strong effect on individual cell migration. A) Representative brightfield microscopy images of fixed and stained ovarian cancer cell lines ES-2_luc shNEG, ES-2_luc shGPAM1, ES-2_luc shGPAM2 and ES-2_luc shGPAM3 after 24 h incubation in the transwell assay. B) Quantification of the migration for ES-2_luc shGPAM1, ES-2_luc shGPAM2 and ES-2_luc shGPAM3 cells compared to the control ES-2_luc shNEG. The migration index was the number of cells in each image normalized to the number of cells in the respective control wells. The migration indices were from two inserts per cell line and four images per membrane of the insert and normalized to the shNEG control from each biological replicate. Data is presented as the mean value with the standard deviation from three biological replicates with four technical replicates each.

3.3.3 Stable knockdown of GPAM reduces the formation of colonies

One key feature of cancer cells is their ability to proliferate indefinitely (Hanahan and Weinberg 2011), a basic characteristic which is important for cancer development and metastasis, where individual cancer cells need to grow on the secondary metastatic sites. Thus, the colony

formation assay (Section 2.18.3) was used to test if silencing GPAM affected the clonogenic capacity of ES-2 ovarian cancer cells. This assay tests the ability of a single cell to form a colony (Franken et al. 2006). Briefly, the ovarian cancer cell lines ES-2_luc shNEG, ES-2_luc shGPAM1, ES-2_luc shGPAM2 and ES-2_luc shGPAM3 were seeded at a very low cell number and incubated under standard cell culture conditions until colonies were observed. The colonies were then stained, fixed and their number and size quantified.

Visual examination of the control shNEG cell line revealed the formation of colonies of variable size and cell number as indicated by the staining intensity (Figure 11A, shNEG). Furthermore, both visual inspection (Figure 11A) and subsequent quantification (Figure 11B) showed that silencing GPAM led to a strong decrease in the number of colonies (approximately 80%) compared to the control shNEG cell line (Figure 11B). Additionally, the decrease was consistent, i.e. with a low variability among the biological replicates, in all knockdown cell lines (Figure 11B). Conversely, visual inspection and subsequent quantification did not demonstrate a clear effect on colony size, which was highly variable among the shGPAM cell lines, as well as the negative control cells (Figure 11A, shNEG). In summary, the stable knockdown of GPAM has a significant effect on the number of colonies formed but no effect on the size of the colonies which are highly variable.

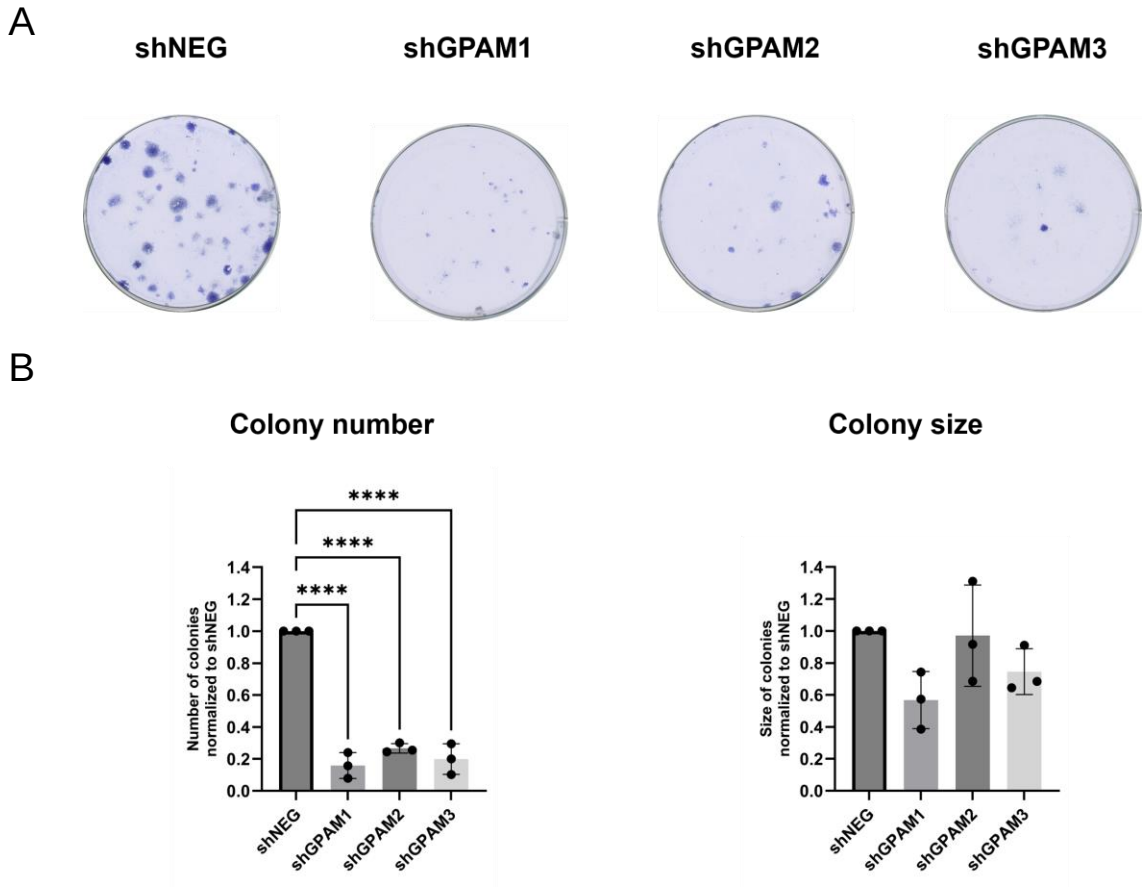

Figure 11 Stably silencing GPAM reduces the formation of colonies. ES-2_luc shNEG, ES-2_luc shGPAM1, ES-2_luc shGPAM2 and ES-2_luc shGPAM3 cells were seeded for colony formation assay. After 11 days colonies were fixed and stained with crystal violet fixation solution. A) Representative images of fixed and stained colonies of the cell lines ES-2_luc shNEG, ES-2_luc shGPAM1, ES-2_luc shGPAM2 and ES-2_luc shGPAM3. B) Quantification of the number (left side) and size (right side) of the colonies formed by the cells ES-2_luc shGPAM1, ES-2_luc shGPAM2 and ES-2_luc shGPAM3 compared to the control ES-2_luc shNEG. Data is presented as the mean value with the standard deviation from three biological replicates with three technical replicates each. ****, $p < 0.0001$.

3.3.4 GPAM knockdown does not influence anoikis resistance

Anoikis is a cell death program activated when cells lose their connection to the extracellular matrix (Frisch and Francis 1994). The resistance to anoikis is an acquired characteristic of cancer cells, especially needed during metastasis when the cancer cells detach from the primary tumor and surrounding tissue and disseminate towards a metastatic secondary site (Taddei et al. 2012). Therefore, it was evaluated if stably silencing GPAM reduces the resistance of ovarian cancer cells to activate anoikis. As explained in Section 2.18.4, ES-2_luc shNEG, ES-2_luc shGPAM1, ES-2_luc shGPAM2 and ES-2_luc shGPAM3 cell lines were plated either in wells that were coated with poly(2-hydroxyethyl methacrylate) (pHEMA) (anchorage re-

sistant plates) to prevent attachment and induce anoikis in normally adherent cells or in uncoated control plates where cells could attach freely and survive. Comparing the viability of the cells plated on the uncoated plates to those from the coated plates ensures that any loss in viability in the coated plates is due to a loss of cell attachment (anoikis) and not to factors, such the media. Cell viability was measured after 24 h with the CellTiter-Blue® assay (Promega).

The effect of silencing GPAM on anoikis resistance was analyzed by comparing the viability of the ES-2_luc shGPAM cell lines to the ES-2_luc shNEG control cell line in the coated plates, which was then compared to the viability of the cells in the uncoated plates. No significant differences were observed between the knockdown and control cell lines, nor between the coated and the uncoated plates (Figure 12), overall suggesting that GPAM does not influence resistance to anoikis in the ES-2 cells.

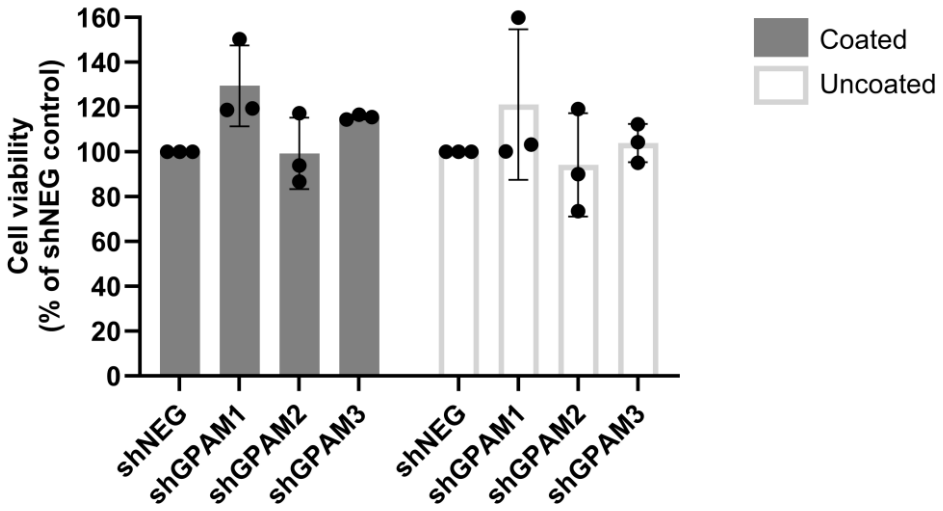

Figure 12 Stably knocking down GPAM does not influence anoikis resistance. The cell lines ES-2_luc shNEG, ES-2_luc shGPAM1, ES-2_luc shGPAM2 and ES-2_luc shGPAM3 were plated on pHEMA-coated anchorage resistant plates as well as uncoated control plates and incubated under standard cell culture conditions for 24 h. The CellTiter-Blue® assay (Promega) was then used to determine the viability of the knockdown cell lines compared to the control cell line. The cell viability is presented compared to the respective ES-2_luc shNEG control and as the mean value ± standard deviation of three biological replicates.

3.4 First experiment indicates a role for GPAM in ovarian cancer metastasis in vivo

The stable knockdown of GPAM led to a decrease in cancer-relevant processes in vitro, such as collective cell migration and colony formation. Among the stable cell lines created, ES-2_luc shGPAM1 exhibited the most uniform knockdown at mRNA level compared to the other ES-2_luc shGPAM cell lines as well as a significant difference in collective cell migration and colony formation compared to the control cell line ES-2_luc shNEG. Thus, ES-2_luc shGPAM1 and ES-2_luc shNEG were next injected intraperitoneally (IP) into female CD-1 nude mice to establish a peritoneal metastasis model to evaluate the influence of GPAM in ovarian cancer metastasis, as the transcoelomic spread through the peritoneal cavity is the most common route of metastasis in ovarian cancer (Lengyel 2010).

As outlined in Figure 13A, $5 \cdot 10^6$ ES-2_luc shNEG or ES-2_luc shGPAM1 cells were injected IP into female CD-1 nude mice, and the bioluminescence signal in the mice was measured once a week over a period of eight weeks, at which time the mice were sacrificed and internal organs of the peritoneum analyzed to evaluate metastatic spread. The bioluminescence signal can be interpreted as a measure of the quantity of cancer cells present in the mouse. In order to reliably measure tumor growth, the bioluminescence signal measured in each mouse per week was normalized to the measured bioluminescence signal in the same mouse directly after the injection of the cells (time 0), what herein is presented as ‘relative total flux’.

The bioluminescence signal in mice injected with ES-2_luc shNEG cells (shNEG mice) appeared to increase over time during the first five weeks, after which there was a slow decrease in the bioluminescence signal, which was nevertheless still present after eight weeks (Figure 13B and Figure S3A). The bioluminescence signal in mice injected with ES-2_luc shGPAM1 cells (shGPAM1 mice) showed a similar pattern, but the increase in bioluminescence was only observed during the first two weeks (Figure 13B and Figure S3), after which a faster decrease of the bioluminescence signal was observed compared to shNEG, which was significantly different after six weeks and almost completely absent after eight weeks (Figure 13C). Quantitative analysis of the ex vivo bioluminescence signal of the collected peritoneal organs of mice revealed a similar trend as measured in the mice in vivo, showing an on average higher bioluminescence signal in the organs of shNEG mice compared to shGPAM1, albeit not statistically significant (Figure 13D and Figure S3B). Thus, the results of this first in vivo experiment indicate that GPAM may promote ovarian cancer metastasis, although the results

of its inhibition in the ES-2 cells were highly variable between biological replicates and should be confirmed in future studies. Details about these future studies are discussed in Section 4.4 below.

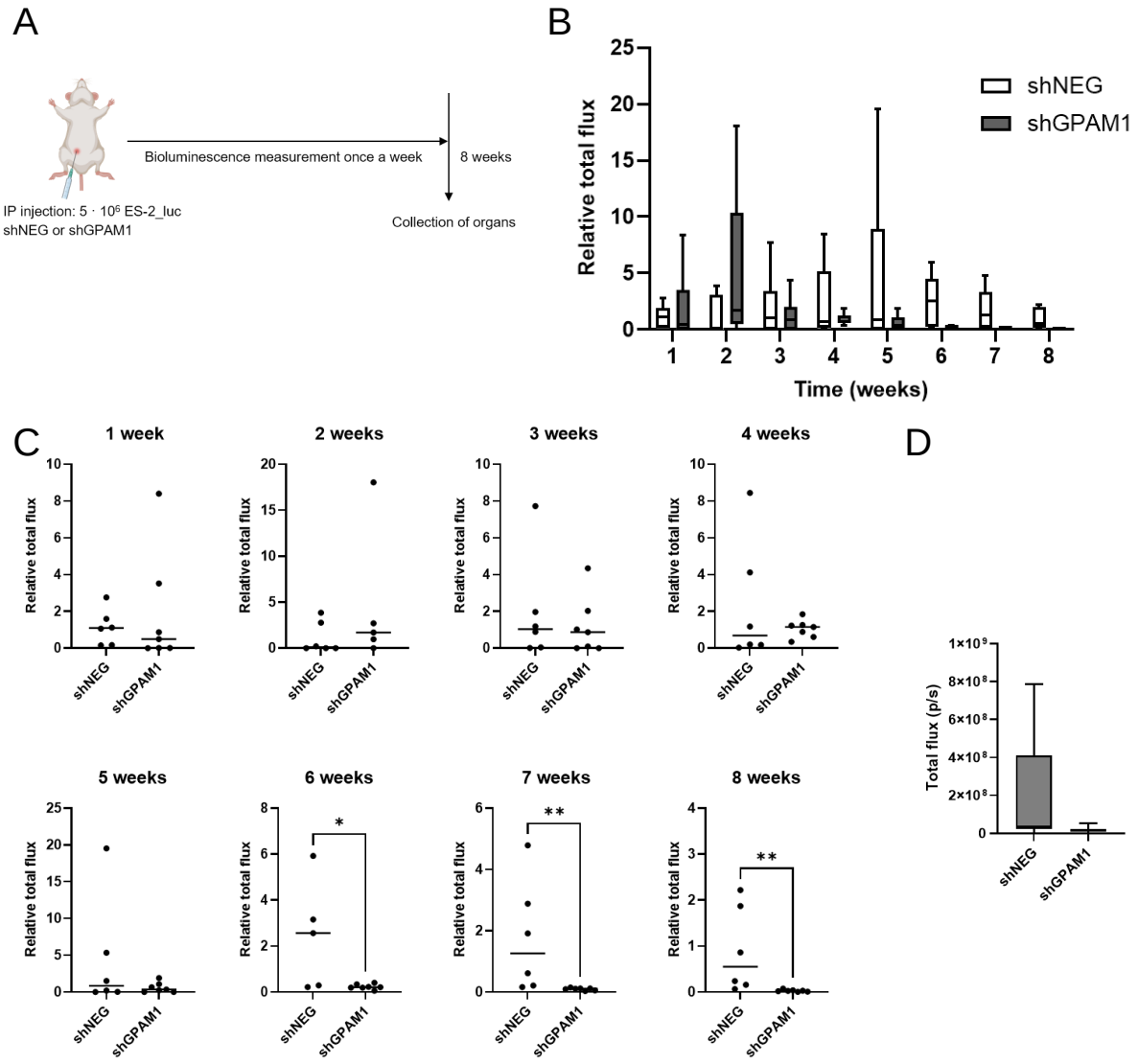

Figure 13 GPAM may have a role in ovarian cancer metastasis. A) Schema of the experimental outline. A cell number of $5 \cdot 10^6$ ES-2_luc shNEG or ES-2_luc shGPAM1 cells was injected intraperitoneally (IP) into female CD-1 nude mice, and the bioluminescence signal in the mice was measured once a week for eight weeks, when the mice were sacrificed and internal organs collected. B) Quantitative analysis of the bioluminescence signal in mice injected with ES-2_luc shNEG (shNEG) or ES-2_luc shGPAM1 cells (shGPAM1) normalized to the bioluminescence signal in the same mouse just after IP injection of the cells. C) As in B but showing individual data points. D) Ex vivo bioluminescence quantification of the collected peritoneal organs from shNEG or shGPAM1 mice eight weeks from the IP injection. Images of C and D can be found in Figure S3. Data is presented with box plots with whiskers from the minimal to maximal value (B and D) or as individual data points (C) from six to seven mice per condition. *, $p < 0.05$; **, $p < 0.01$.

3.5 Cytotoxicity analysis of the GPAT inhibitor FSG67 in ovarian surface epithelial and cancer cells

Silencing GPAM hindered cancer-relevant processes in vitro and reduced tumor formation in an in vivo metastatic model. However, these experiments were performed using a shRNA stable knockdown system and for subsequent preclinical studies a more relevant approach to inhibit GPAM was needed. Therefore, the GPAT inhibitor small-molecule FSG67 (2-(nonylsulfonamido) benzoic acid) was evaluated in vitro in relation to the same cancer-relevant processes previously investigated and in vivo. FSG67 is a competitive inhibitor of the GPAT enzymes, which was shown, among others, to suppress lipid synthesis in 3T3-L1 adipocytes or decrease serum leptin levels and the accumulation of lipids in the liver of diet-induced obese mice (Kuhajda et al. 2011). Additionally, the compound was also shown to have antitumor activity in acute myeloid leukemia (Irifune et al. 2023). Since this compound was not yet tested in ovarian cancer models, an in vitro cell-viability study was first carried out to evaluate possible concentrations of FSG67 for subsequent experiments. Briefly, the viral-transformed ovarian surface epithelial cells HOSE6-3, HOSE17-1 and I64-hTERT, as well as the ovarian cancer cells ES-2, OVCAR4 and OVCAR8 were incubated with increasing concentrations of FSG67 (Focus Biomolecules) (0.01, 0.0316, 0.1, 0.316, 1, 3.16, and 5 mM) under standard cell culture conditions for 24 and 48 h, and thereafter the cell viability was determined with the CellTiter-Blue® assay (Promega).

To evaluate the cytotoxicity activity of FSG67 in the tested cell lines, the cell viability data was fitted to a logistic model and the inhibitory concentrations (IC) IC_{20} and IC_{50} calculated. First, the quality of the curve fit was evaluated with the coefficient of determination R^2, where values close to 0 denote a poor fit; whereas values close to 1 denote an optimal fit. Overall, the curve fit showed a good performance, with R^2 values ranging from 0.87 to 0.99 (Figure 14). Then, the IC_{20} and IC_{50} values were evaluated. With the exception of the viral-transformed ovarian surface epithelial cells HOSE6-3 and I64-hTERT, which appeared to be more resistant to FSG67 than the other cells at 24 h based on their respective higher IC_{50} values (Figure 14A), in general similar IC values were observed between the ovarian surface epithelial cells and the ovarian cancer cells (Figure 14). In short, these first analyses provided guidance as to which FSG67 concentrations were suitable to use when studying the effect of the compound on cancer-relevant cell processes.

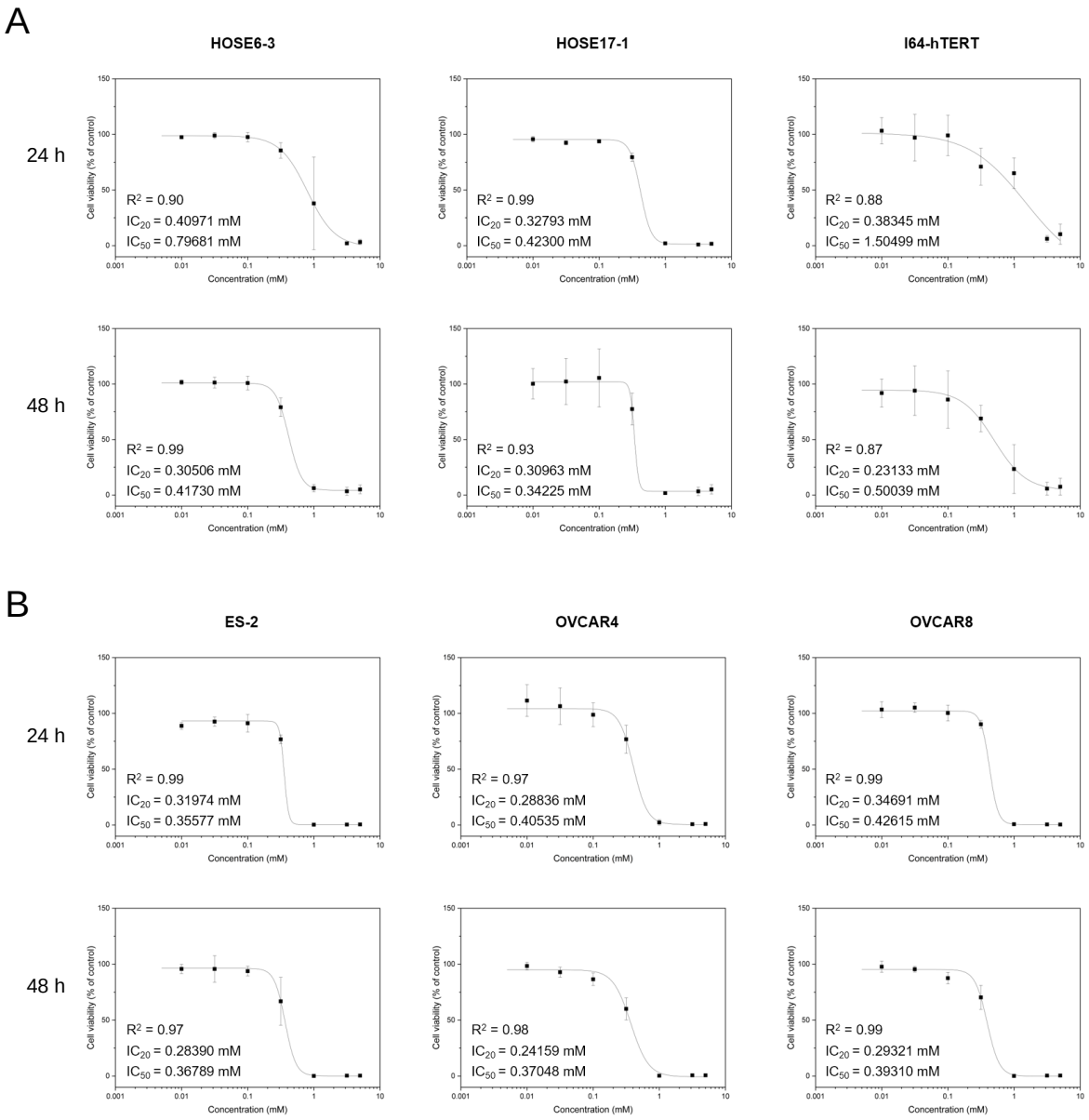

Figure 14 Analysis of the cytotoxicity of FSG67 in ovarian cells. A) The viral-transformed ovarian surface epithelial cells HOSE6-3, HOSE17-1 and I64-hTERT were incubated with increasing concentrations of FSG67 under standard cell culture conditions for 24 and 48 h, and then the cell viability was determined with the CellTiter-Blue® assay to perform a dose-response analysis, fitting the cell viability data to a logistic model from which the inhibitory concentrations (IC) IC_{20} and IC_{50} were calculated. B) As in A, but testing the ovarian cancer cells ES-2, OVCAR4 and OVCAR8. The cell viability is presented compared to the respective control and as the mean value ± standard deviation of three biological replicates.

3.6 Inhibiting GPAM with FSG67 hinders cancer-relevant processes in vitro

Having established FSG67 concentrations that do not significantly impact the viability of the studied ovarian cancer cells, the effect of the inhibitor on colony formation, migration and anoikis resistance was next studied.

3.6.1 FSG67 alters the formation of colonies

Metastasis is one of the hallmarks of cancer (Hanahan and Weinberg 2011), where cancer cells leave the primary tumor, travel to secondary organs, either via the blood, lymph or body cavities, where they attach and proliferate to colonize this new site. The colony formation assay can be used to mimic several steps of this metastatic colonization, such as the initial attachment and the subsequent proliferation. Thus, the colony formation assay (Section 2.18.3) was performed using two approaches to investigate whether FSG67 would influence either process. Here, three ovarian cancer cells ES-2, OVCAR4 and OVCAR8 were used. The cells were treated with FSG67 at the time of seeding (to investigate its effect on initial attachment) or on the day after seeding (to study proliferation). The cells were incubated under standard cell culture conditions, and the produced colonies were fixed and stained, followed by quantification of the number and size of the colonies.

As observed in the cell line ES-2_luc shNEG (Figure 11A, shNEG), visual inspection of the untreated colonies revealed that ES-2 formed colonies with variable size and intensities (Figure 15A). In contrast, both OVCAR4 and OVCAR8 formed uniformly sized colonies. Treating the cells with 60 or 90 µM FSG67 resulted in no significant difference in the number of colonies for any of the three cell lines, regardless of if the cells were treated at the time of seeding (Figure 15B) or the day after seeding (Figure 15C). No significant effect was also seen in colony size of ES-2 and OVCAR4 cells in response to FSG67 treatment. In contrast, a significant difference was observed in the size of the OVCAR8 colonies when treated at the time of seeding or on the day after seeding (Figure 15B and Figure 15C). Specially, a dose-dependent reduction in the size of the OVCAR8 colonies was observed that was significant for both concentrations of FSG67 when the treatment was performed on the day after seeding (Figure 15C). In summary, FSG67 reduced colony size but not colony number, and the latter was only detected in OVCAR8 cells, especially when treated on the day after seeding.

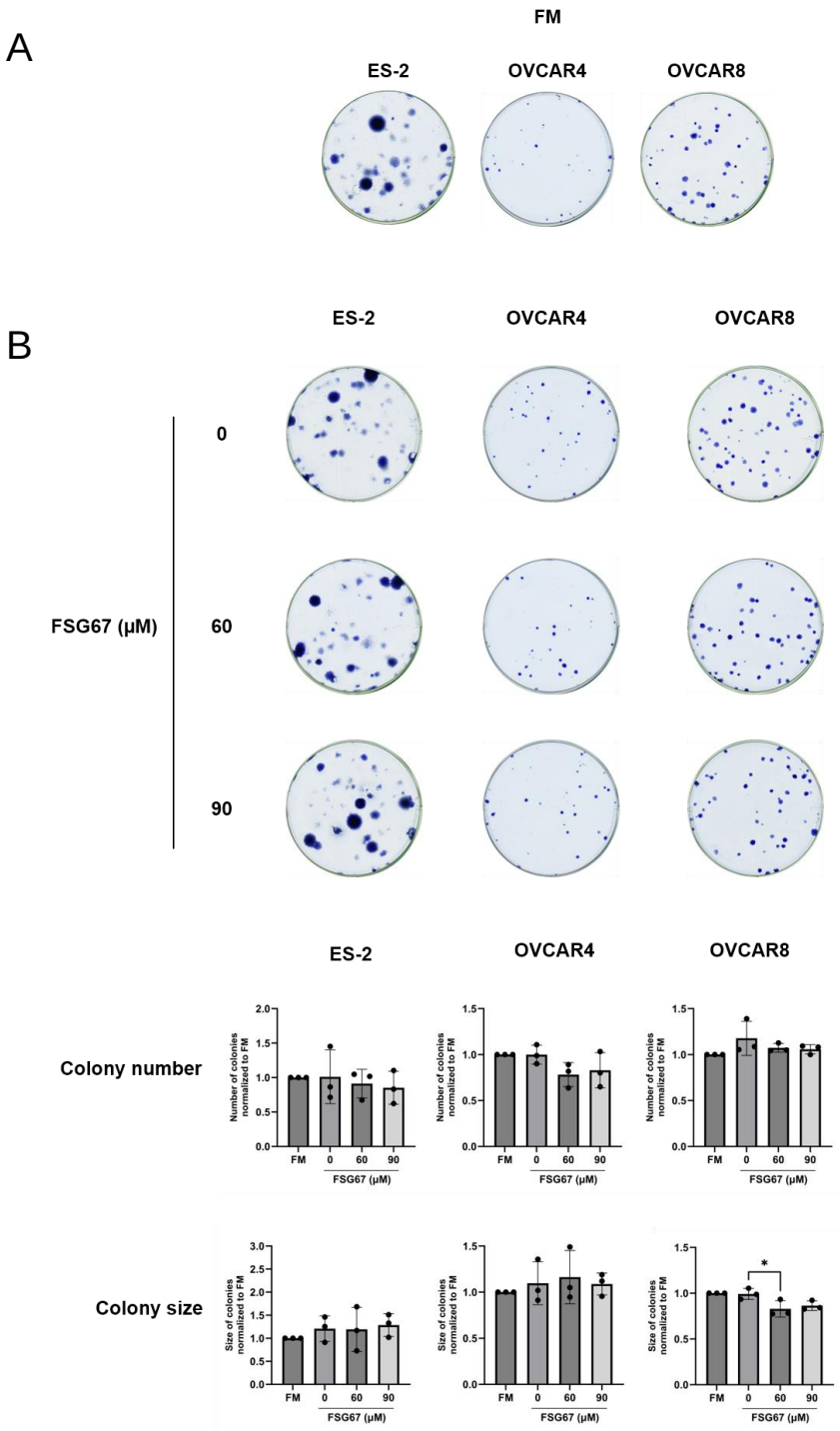

Figure 15 The GPAT inhibitor FSG67 influences the colony size in a cell line-specific manner. ES-2, OVCAR4 and OVCAR8 cells were seeded for colony formation assay. After 11 days (ES-2 and OVCAR8) or 13 days (OVCAR4) colonies were fixed and stained with crystal violet fixation solution. A) Representative images of fixed and stained colonies of the full medium (FM) untreated cell lines ES-2, OVCAR4 and OVCAR8. B) Representative images of fixed and stained colonies ES-2, OVCAR4 and OVCAR8 when treated at the time of seeding (upper part) with 0 (DMSO-only control), 60 and 90 µM FSG67, as well as the quantification of the number and size of the colonies normalized to the FM control (bottom part). C) As in B, but in this case the cells were treated on the day after seeding. Data is presented as the mean value with the standard deviation from three biological replicates with three technical replicates each. *, $p < 0.05$; **, $p < 0.01$ and ***, $p < 0.001$.

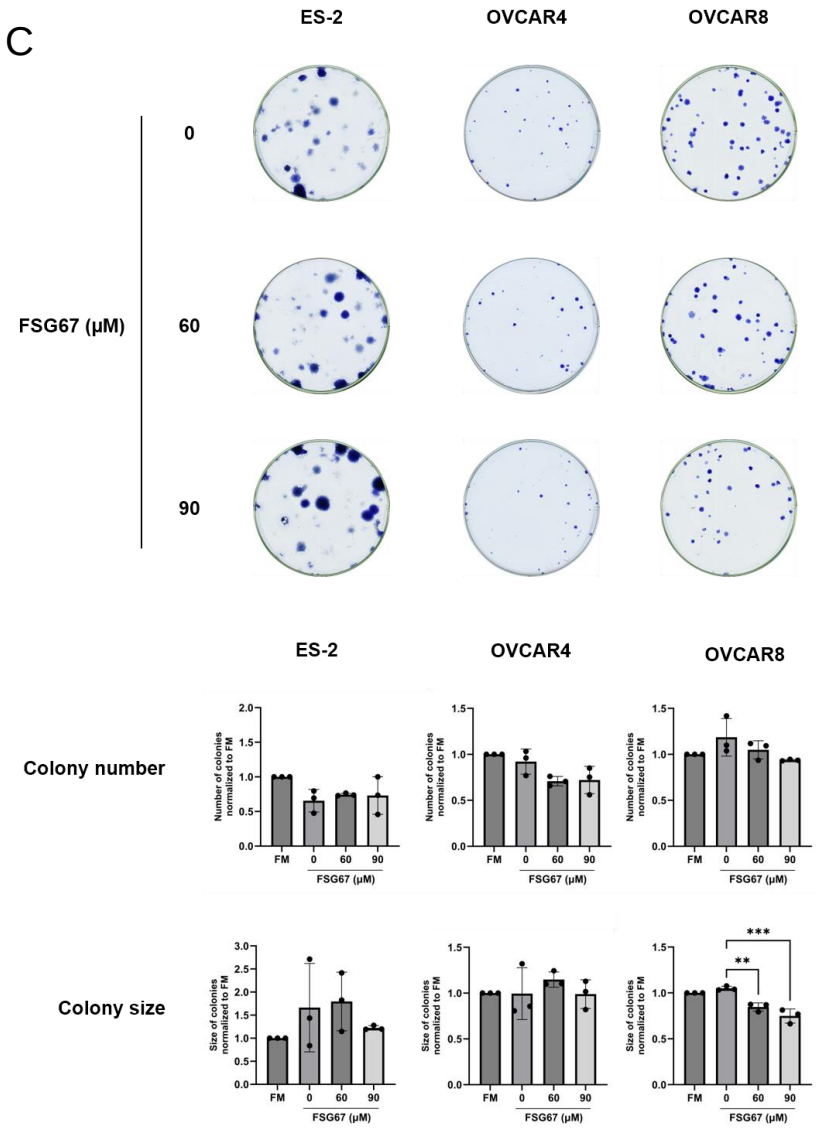

Figure 15 Continued from page 69.

3.6.2 FSG67 strongly reduces individual cell migration

The transwell assay (Section 2.18.2) was used to study if FSG67 hinders individual cell migration of ovarian cancer cells. The ovarian cancer cells ES-2, OVCAR4 and OVCAR8 were placed in serum-free medium in transwell inserts, treated with FSG67 and allowed to migrate towards full medium through the pores of the membranes for 24 h. Then, cells that migrated to the outer membranes were fixed and stained with crystal violet fixation solution and quantified. The migration of the cells without FSG67 was compared to the migration of the cells in presence of FSG67. Brightfield images of the transwell insert membranes showed a strong decrease in migrated cells when FSG67 was added (Figure 16A). Both 60 and 90 µM FSG67 led to a significant decrease in migration in all three tested ovarian cancer cell lines (Figure 16B). Quantification of the images additionally revealed that the decrease was quite con-

sistent among all three cell lines, which was dose dependent in the ES-2 cells (Figure 16B). Therefore, it can be concluded that FSG67 strongly reduces individual cell migration in the cell lines tested.

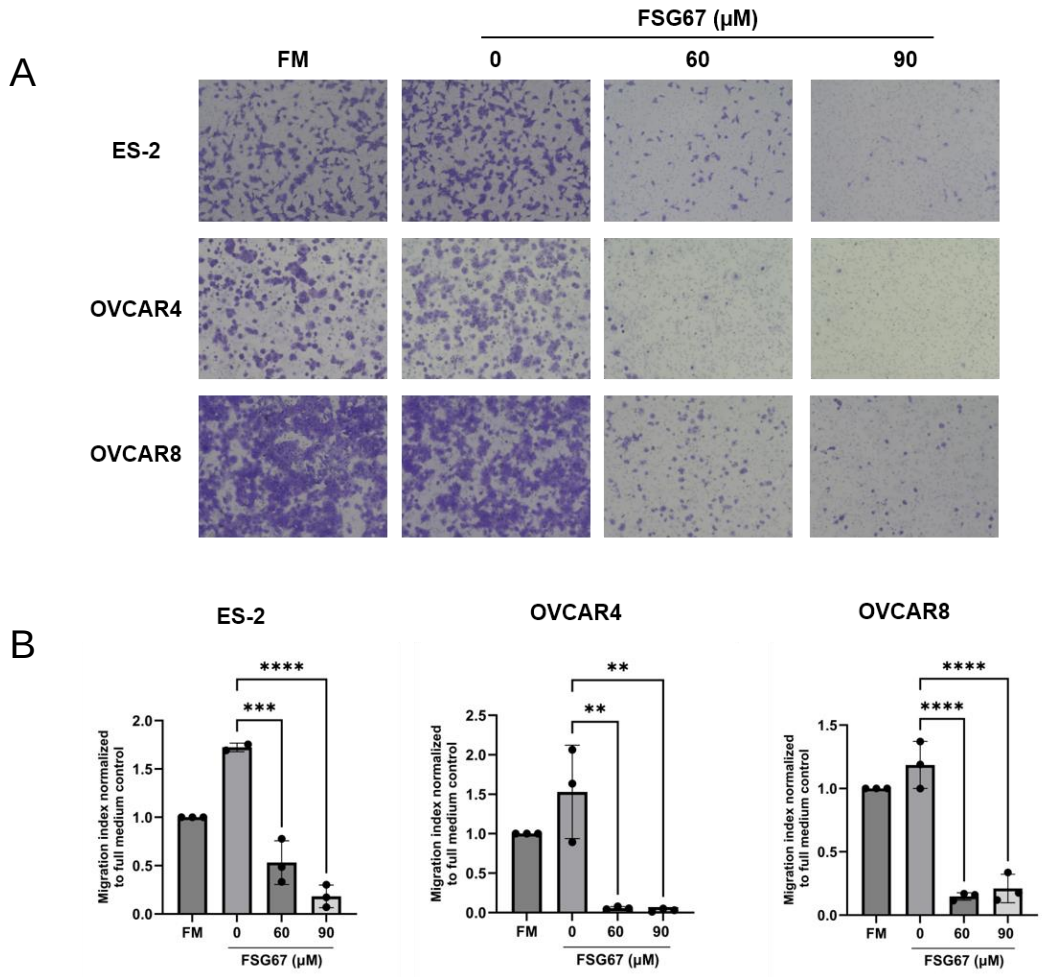

Figure 16 FSG67 strongly reduces individual cell migration in three ovarian cancer cell lines. A) Representative brightfield images of fixed and stained ovarian cancer cells ES-2, OVCAR4 and OVCAR8 after 24 h incubation in the transwell assay in presence of FSG67 (0 (DMSO-only control), 60 and 90 µM). FM stands for full medium. B) Quantification of the migration of the cells ES-2, OVCAR4 and OVCAR8 compared to the respective untreated full medium control. The migration index was the number of cells in each image normalized to the number of cells in the respective control wells. The migration indices were from two inserts per condition and four images per membrane of the insert and normalized to the respective untreated full medium control from each biological replicate. Data is presented as the mean value with the standard deviation from three biological replicates with four technical replicates each. **, $p < 0.01$; ***, $p < 0.001$ and ****, $p < 0.0001$.

3.6.3 FSG67 impairs collective cell migration

As previously mentioned, collective cell migration refers to the movement of cells as a group, a physiological process performed by many different cell types, for example during wound

healing and embryonic development, as well as by cancer cells during invasion processes (Rorth 2009). Therefore, the wound closure assay (Section 2.18.1) was employed to evaluate whether FSG67 inhibits collective cell migration in ovarian cancer cells by creating two artificial gaps (the 'wounds') in confluent monolayers of the ES-2 and OVCAR8 cells. OVCAR4 cells were not investigated in this assay since they are not suitable for the wound closure assay, as they do not form a uniform monolayer. The wounds were evaluated at different time points (5 and 24 h) after the cells were treated with the two concentrations of FSG67 (60 and 90 µM) used in the transwell assay.

No effect was observed when the wounds were examined 24 h after the treatment, since all wounds for all treatment conditions were already closed (Figure 17A). Nonetheless, these results do not imply that the tested concentrations of FSG67 had no effect on collective cell migration. FSG67 could have reduced the migration speed of the cells, and although slower compared to the cells in the absence of FSG67, cells treated with FSG67 had enough time to close the wound. Therefore, the assay was repeated examining the wounds 5 h after treatment. At this time, the wounds were not completely closed (Figure 17B), but the remaining gap to be closed was similar in all tested conditions for both ES-2 and OVCAR8 cells (Figure 17B, bottom part). Therefore, a subsequent experiment was repeated with higher concentrations of FSG67, specifically 180 and 270 µM, concentrations that were still lower than the IC_{20} of the compound in these cell lines (Figure 14B, upper panels). Here a reduction of the wound closure was observed with 270 µM FSG67 (Figure 17C) in both cell lines after 24 h. Furthermore, the reduction was significant after 5 h of treatment in the ES-2 monolayers, but not the OVCAR8 monolayers (Figure 17C). In conclusion, these results show that the GPAT inhibitor FSG67 impairs collective cell migration in ovarian cancer cells at the highest tested concentration of 270 µM.

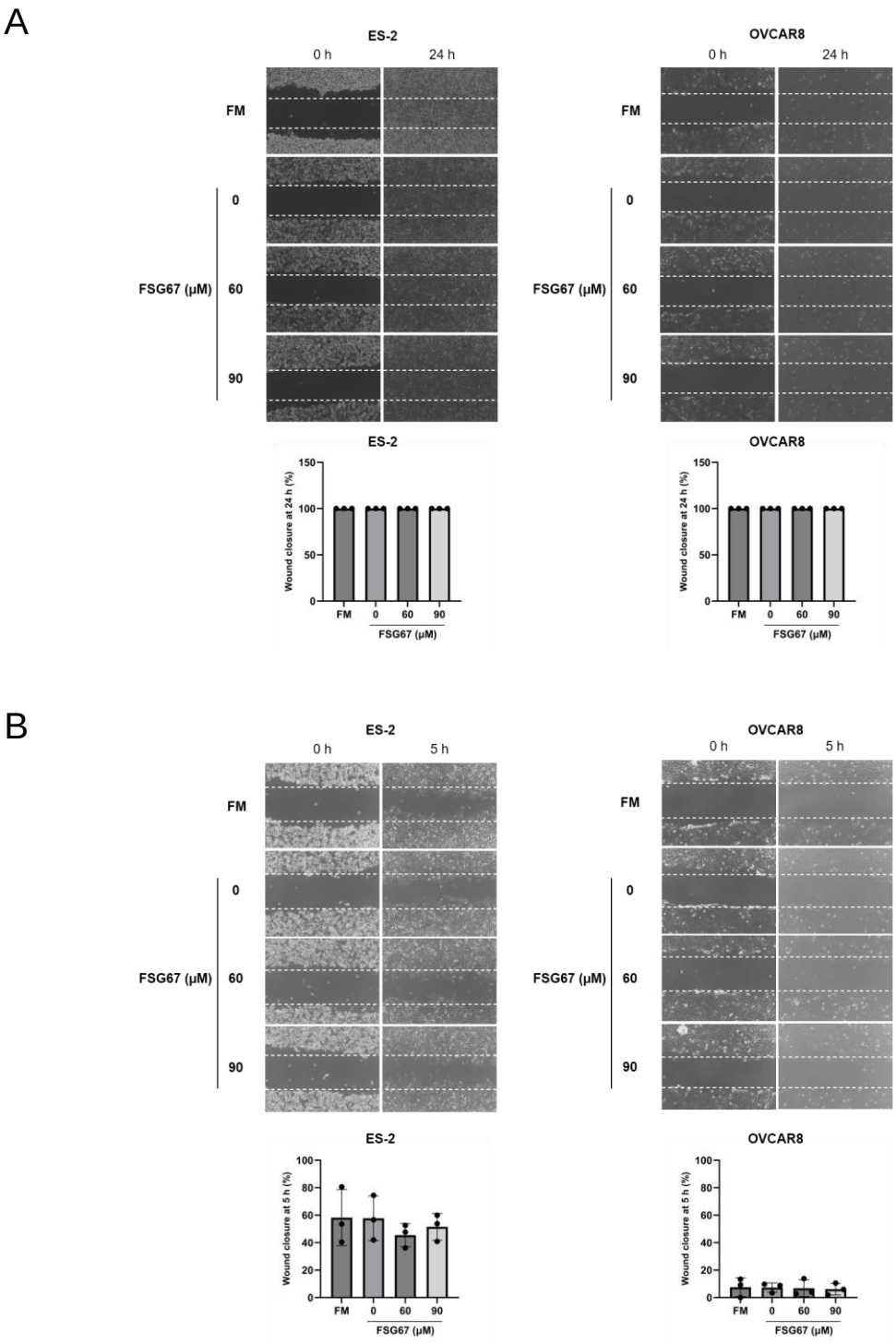

Figure 17 The GPAT inhibitor FSG67 impairs collective cell migration. A) Representative phase contrast microscopy images of the ES-2 and OVCAR8 monolayers at the time of creating the wound (0 h) and 24 h later in full medium (FM) and with FSG67 (0 (DMSO-only control), 60 and 90 µM) (upper part) together with the quantification of the wound closure after 24 h, measured as the percentage of wound closure with respect to the initial wound (bottom part). B) As in A, but in this case the wound closure was evaluated after 5 h. C) As in A and B but testing 0 (DMSO-only control), 180 and 270 µM FSG67 which was evaluated after both 5 and 24 h. Data is presented as the mean value ± standard deviation from three biological replicates, and each biological replicate was performed in four technical replicates. **, $p < 0.01$ and ****, $p < 0.0001$.

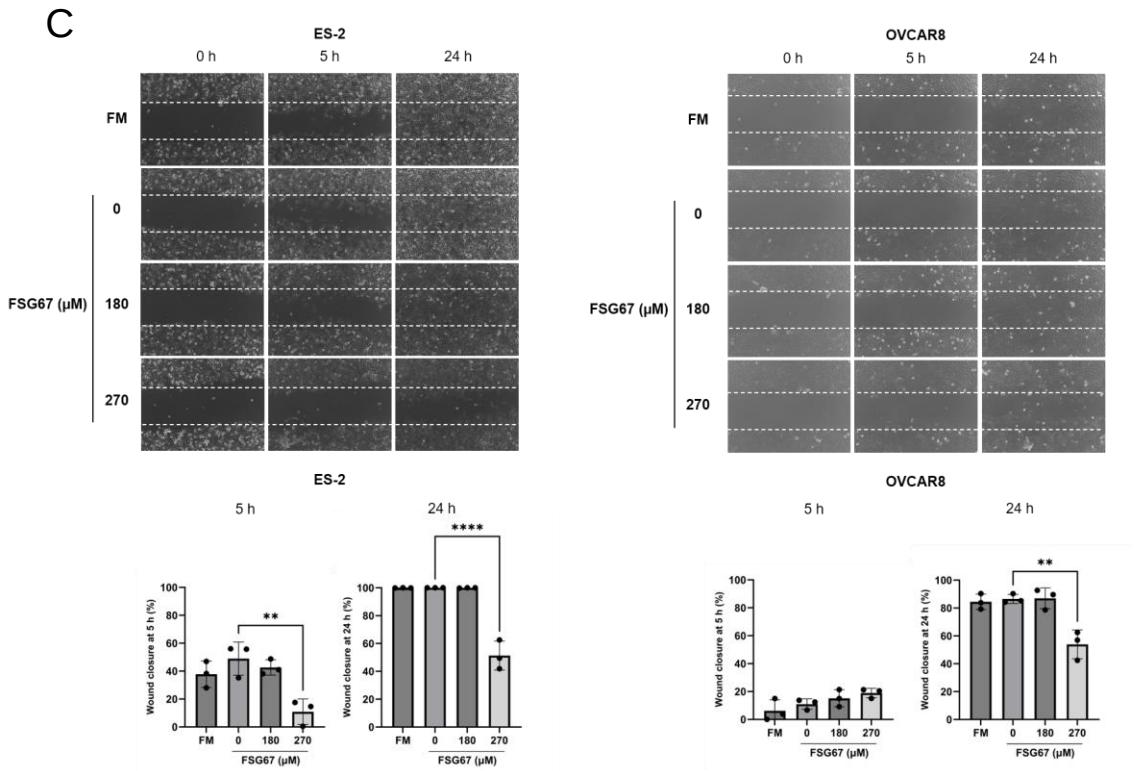

Figure 17 Continued from page 73.

3.6.4 FSG67 reduces the resistance to anoikis

To investigate the effect of FSG67 on anoikis resistance, ES-2, OVCAR4 and OVCAR8 cells were plated onto pHEMA coated plates, which prevents attachment and are used to induce anoikis in normally adherent cells, as well as uncoated plates that are used as controls to ensure that the cell line being used is capable of attachment and survival. The cells were treated with different concentrations of FSG67 at the time of plating and incubated under standard cell culture conditions for 24 h after which the cell viability was evaluated with the CellTiter-Blue® assay (Promega).

In order to assess if FSG67 reduces resistance to anoikis, the viability of the studied ovarian cancer cell lines was compared among the different concentrations of FSG67, as well as between the pHEMA-coated and uncoated plates. In this experimental setup, the highest concentration of 270 µM FSG67 significantly decreased the viability of ES-2 cells in suspension in the coated plates compared to 0 µM FSG67 (Figure 18A, coated), what may imply a reduction in anoikis resistance. However, this decrease was also observed in the uncoated plates (Figure 18A, uncoated), indicating that this reduction in viability was not specifically due to an effect of FSG67 on anoikis, but rather due to the compound itself. A concentration of 180 µM

FSG67 also led to a reduction in anoikis resistance of ES-2 cells in the coated plates, which was not significant (Figure 18A, coated). However, compared to the uncoated plates, treatment of cells with 180 µM FSG67 on the coated plates led to a statistically significant decrease in cell viability (Figure 18A). These results suggest that the detached cells in the coated plates, i.e. when anoikis is triggered, were more sensitive to the increasing FSG67 concentrations, until a concentration was reached where an effect of FSG67 specifically on anoikis could not be evaluated. OVCAR4 cells appeared to be more resistant to the effect of FSG67 and anoikis, since a statistically significant difference was only reached with the highest concentration of FSG67 and anoikis-activated cells in the coated plates (Figure 18B). Finally, OVCAR8 cells showed a similar phenotype as the ES-2 cells regarding the effect of FSG67 and anoikis with a significant difference seen with 180 µM (Figure 18C). Taken together, with all three cell lines there was a small but significant decrease in anoikis resistance with FSG67, but with different concentrations of the compound (namely 180 µM for ES-2 and OVCAR8 cell lines and 270 µM for OVCAR4), suggesting that FSG67 reduces resistance to anoikis in ovarian cancer cells, but with different sensitivities.

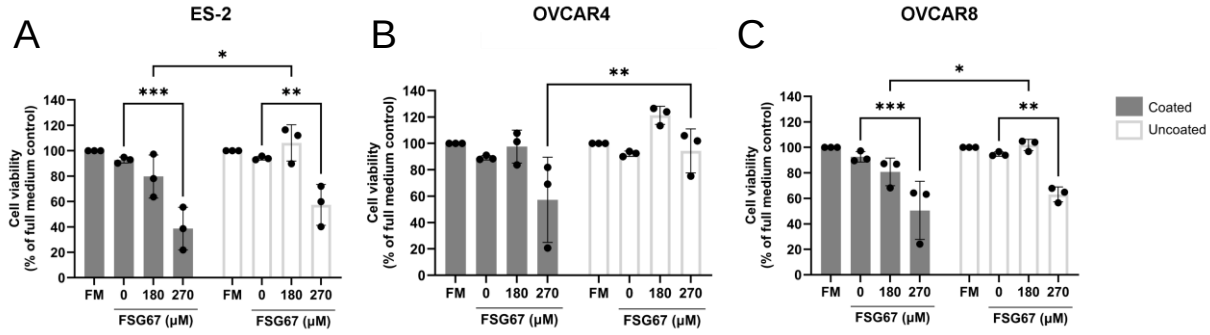

Figure 18 The GPAT inhibitor FSG67 reduces anoikis resistance. The cell lines ES-2 (A), OVCAR4 (B) and OVCAR8 (C) were plated on pHEMA-coated anchorage resistant plates as well as uncoated control plates, treated at the time of plating with FSG67 and incubated under standard cell culture conditions for 24 h. The CellTiter-Blue® assay (Promega) was then used to compare the viability of the cells in the absence or with FSG67, as well as the viability in coated or uncoated cell plates. The cell viability is presented compared to the respective full medium (FM) control and as the mean value with the standard deviation of three biological replicates. *, $p < 0.05$; **, $p < 0.01$ and ***, $p < 0.001$.

3.7 Toxicology and pharmacokinetic studies of FSG67 in vivo

Since data from the present study showed that the GPAT inhibitor FSG67 impairs cancer-relevant processes in ovarian cancer cells in vitro, FSG67 was evaluated in initial experiments in vivo (Section 2.21) to determine the toxicological and pharmacokinetic profile of the com-

pound for subsequent in vivo studies. First, a maximum tolerated dose (MTD) study was performed, where female CD-1 mice were treated intraperitoneally (IP) with increasing doses of FSG67, starting with 10 mg/kg and increasing every 3 – 4 days until the mice developed signs of toxicity, and then the prior dose was used for following experiments. In the described MTD study, 50 mg/kg was found to be the maximal safe dose and was used for the subsequent repeated dose toxicity (RDT) study. In this RDT study, female CD-1 mice were treated with 50 mg/kg FSG67 IP for two weeks, five days on and two days off. Vehicle-treated as well as FSG67-treated mice did not show any sign of toxicity or acute loss of weight during the course of the study, with all mice maintaining a similar weight of approximately 28 g (Figure 19A) and without reaching a 10% loss in body weight (Figure 19B). Thus, 50 mg/kg FSG67 IP for two weeks was proven to be safe for subsequent in vivo studies.

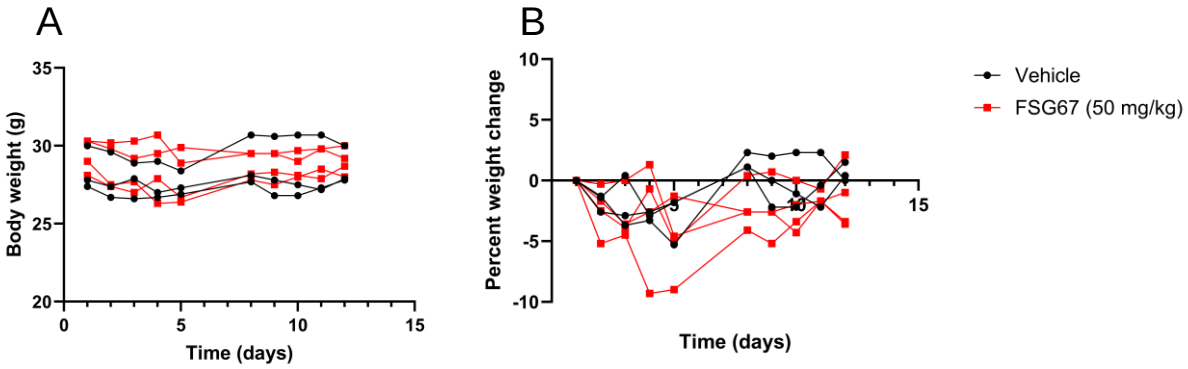

Figure 19 Mice did not show abnormal loss of weight during the FSG67 repeated dose toxicity (RDT) study. Female CD-1 mice were treated with either vehicle or 50 mg/kg FSG67 intraperitoneally (IP) for two weeks, five days on and two days off, and prior to each treatment their weight was measured (A) and the percent weight change respect the first day of treatment was determined (B). Body weights per day of at least three mice per condition are presented.

To determine the pharmacokinetic profile of FSG67, female CD-1 mice were treated IP with a single dose of 50 mg/kg FSG67 and the concentration of FSG67 in the plasma over time was measured at the Lead Discovery Center GmbH (LDC) (Section 2.21). A short absorption phase followed by an elimination phase were observed, reaching a peak plasma concentration of 427.93 µM at 15 min and with practically total elimination of the compound after 6 h (Figure 20). Therefore, 50 mg/kg FSG67 IP may be effective for subsequent in vivo studies with the ovarian cancer cells investigated in the present study, as the peak plasma concentration of 427.93 µM reached the highest IC value in ovarian cancer cells reported in this study (IC_{50} = 426.15 µM for OVCAR8, Figure 14B) and was above the maximal needed concentration to elicit an effect in cancer-relevant processes (270 µM, Figure 17C, Figure 18B).

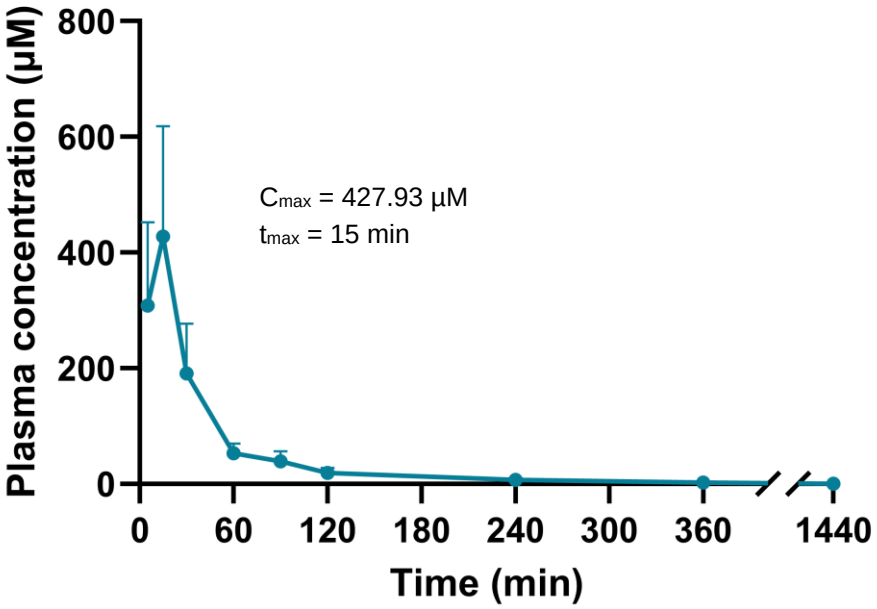

Figure 20 Pharmacokinetic profile of FSG67. Female CD-1 mice were treated intraperitoneally (IP) with 50 mg/kg FSG67, and blood samples were collected after treatment at different time points (from 0 to 24 h), from which the FSG67 plasma concentration was determined using mass spectrometry in collaboration with the Lead Discovery Center GmbH (LDC). Data is presented as the mean value with the standard error of the mean from three mice.

3.8 Studies on intracellular LPA in extracellular signaling and protein interaction partners as regulator of cancer-relevant processes

Results of the present work and previous data (Gonscharow 2025; Irifune et al. 2023; Yao et al. 2023) revealed that silencing or pharmacologically inhibiting GPAM impairs several processes relevant for cancer development and metastasis. Nevertheless, the mechanism underlying GPAM's role in these processes is not known. One of our initial hypotheses linked the observed phenomena to the level of GPAM's intracellular metabolic product, LPA. However, subsequent recent work from our research group showed that the migratory capacity of different ovarian cancer cell lines was independent of alterations in intracellular LPA levels as a result of GPAM silencing (Gonscharow 2025). Therefore, this PhD thesis focused on the role of intracellular LPA in autocrine and/or paracrine signaling and the identification of protein interaction partners to elucidate the mechanism by which GPAM regulates cancer-relevant processes.

3.8.1 Intracellular LPA is not exported into the extracellular environment

Most of the literature on LPA thus far has focused on its role as a structural lipid and an extracellular signaling molecule (Geraldo et al. 2021; Yung, Stoddard, and Chun 2014). However, intracellular LPA may also act in an autocrine and/or paracrine manner to regulate cancer-relevant processes (Xie, Gibbs, and Meier 2002). Therefore, it was hypothesized that intracellular LPA must first be exported into the extracellular environment to mediate autocrine and/or paracrine functions.

3.8.1.1 Introduction of exogenous labeled LPA into ovarian cancer cells

To be able to determine if intracellular LPA is exported into the extracellular environment, it is necessary to be able to first detect LPA inside the cells, which was accomplished in the present work using differently labeled LPA molecules. Previous work by the research group used lipofectamine to introduce LPA into cells to show that increasing concentrations of intracellular LPA is associated with increased migration (Marchan et al. 2017). Nevertheless, this early study was done in the breast cancer cell line MCF7, and therefore the conditions needed to be optimized for the ovarian cancer cell lines used in the present work. Therefore, the fluorescent LPA TopFluor® Lyso PA (Avanti Research) and fluorescent microscopy were used with different concentrations of TopFluor® Lyso PA without and with lipofectamine (Lipofectamine™ 3000 Reagent (Thermo Fisher Scientific)) (Section 2.22) to identify the minimal and maximal concentrations needed to obtain a satisfactory signal inside the cell. The absence or presence of lipofectamine was used to determine if the molecule could naturally move into the intracellular space or if an artificial process such as transfection with lipofectamine was needed.

As expected, no fluorescence signal was observed in the ovarian cancer cells COV318 before adding the fluorescent LPA TopFluor® Lyso PA (Figure 21A). After 1 h incubation with 10 µM fluorescent LPA (both without and with lipofectamine), fluorescence was detected inside the cells (Figure 21B) and further incubation with increasing concentrations of fluorescent LPA led to higher fluorescent signals in the intracellular space. Interestingly, a fluorescent signal was observed inside the cells without the addition of lipofectamine, suggesting that fluorescent LPA was able to enter the cell via an active or passive transport mechanism that is not yet identified. To date, there is little to no evidence showing that LPA can cross the membrane to enter the cell from the extracellular environment. While the data is encouraging it may not reflect the uptake of the LPA molecule. TopFluor® Lyso PA is a LPA molecule

with a saturated fatty acid chain linked to a BODIPY fluorophore by an amide bond, and this BODIPY component may promote the movement of fluorescent LPA into the cell by increasing its lipophilicity and enhancing membrane interactions. Therefore, to determine whether LPA itself can enter cell, which would be one of the first studies to show this, and then to investigate whether LPA inside the cell can be further exported, ^{13}C-labeled LPA and mass spectrometry analyses were performed.

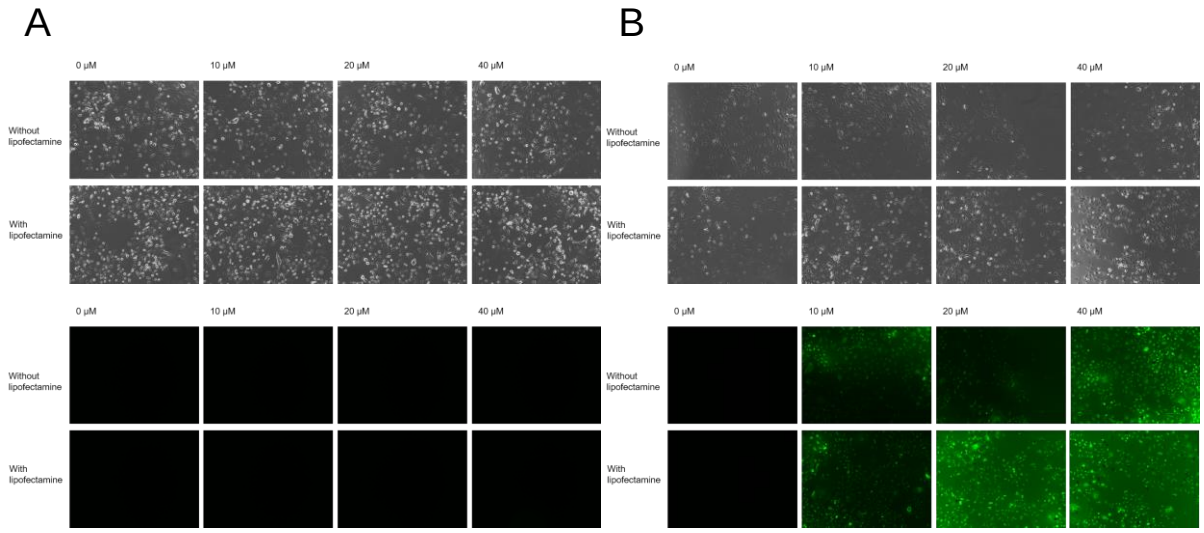

Figure 21 Fluorescent signal of TopFluor® Lyso PA detected in COV318 cells incubated without and with lipofectamine. Just before the incubation with fluorescent LPA images of the ovarian cancer COV318 cells were taken (A), and after 1 h incubation with concentrations of fluorescent LPA ranging from 0 – 40 µM and without or with lipofectamine, fluorescent LPA was removed, and the cells were washed and imaged again (B). Representative images of three biological replicates are shown.

3.8.1.2 ^{13}C-LPA is taken into the cell but not exported into the extracellular space

COV318 cells were incubated with 16:0 LPA (U-13C) (Avanti Research) (^{13}C-LPA) for 1 h, washed, the cell medium replaced by medium without ^{13}C-LPA and the cells were incubated for 2 h. This latter incubation was performed to investigate if any LPA taken into the cells was able to traffic back to the extracellular space. Finally, cells and media samples were collected, and the ^{13}C-LPA concentration was measured in both fractions by mass spectrometry at the Bioanalytics department at IfADo (Section 2.22).

To study the movement of ^{13}C-LPA between the intracellular and the extracellular space, the concentration of ^{13}C-LPA was compared between cells (the intracellular space) and media (the extracellular space) samples. As expected, ^{13}C-LPA was not detected in any sample (cells or media) prior to incubating the cells with ^{13}C-LPA (Figure 22, left half of graph). In con-

trast, a strong signal was detected in the cells when incubated with ^{13}C-LPA (Figure 22, right half of graph) corresponding to approximately 0.5 µM. These results suggest that ^{13}C-LPA was transported from the extracellular space to the intracellular space, and that once inside the cells, ^{13}C-LPA was not exported back into the extracellular space, as the levels in the media remained under the limit of detection after 2 h incubation.

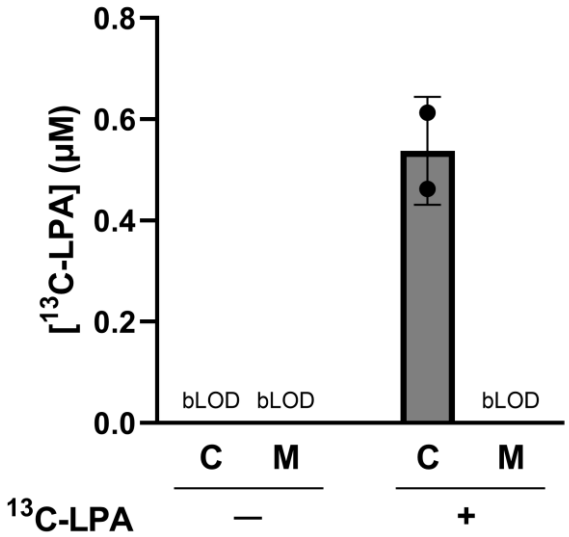

Figure 22 ^{13}C-LPA could have been moved from the extracellular space to the intracellular space and, once inside the cells, ^{13}C-LPA could not be transported back. Ovarian cancer COV318 cells were incubated without (−) or with (+) 40 µM 16:0 LPA (U-13C) (^{13}C-LPA) for 1 h at standard cell culture conditions. The cells were subsequently washed, the cell medium replaced by medium without ^{13}C-LPA and the cells were incubated for 2 h at standard cell culture conditions. Thereafter samples from the cells (C) or media (M) were collected to measure the concentration of ^{13}C-LPA by mass spectrometry. The abbreviation bLOD stands for below limit of detection. Data is presented as the mean value ± standard deviation of two biological replicates.

In summary, the results with exogenous labeled LPA molecules suggest that LPA can enter COV318 cells via a mechanism that is not yet known, and once inside the cells, LPA is not exported to the extracellular space where it could bind LPA receptors on the cell surface. Thus, intracellular LPA does not appear to influence the studied cancer-relevant processes by either an autocrine and/or paracrine mechanism, indicating that other hypotheses should be evaluated.

One such mechanism by which intracellular LPA could influence cancer-relevant processes might be related to the distribution of the molecule inside the cell. The accumulation of the molecule in specific organelles, such as the mitochondria, might be linked to cancer-relevant

processes such as cell migration, and thus the disruption of this distribution by the interventions studied in this PhD thesis may lead to the observed phenotypes. Initial work was performed to begin investigating this hypothesis. Specifically, a procedure to visualize LPA inside cells was set up based on 1-palmitoyl-d_9 lysophosphatidic acid (Cayman Chemical) (d-LPA) and coherent anti-Stokes Raman scattering (CARS) microscopy (Section 2.22). The d-LPA molecule is structurally similar to the native molecule 16:0 LPA and contains nine carbon-deuterium bonds that produces a Raman signal that can be imaged in the cells using CARS microscopy (Egoshi, Dodo, and Sodeoka 2022). First the Raman spectrum of the molecule d-LPA was analyzed in order to select the Raman shift to be imaged with CARS microscopy. The criterion used for the selection of the Raman shift was to obtain the strongest signal possible that is in the silent region, that is the Raman shift region of 1800 – 2800 cm^{-1} where no endogenous molecules from the cells produce a Raman signal (Egoshi, Dodo, and Sodeoka 2022). Based on this criterion, the Raman shift at 2104 cm^{-1} was chosen for the d-LPA molecule (Figure 23A). Then, COV318 cells were imaged at 2104 cm^{-1} with CARS microscopy before adding d-LPA and imaging was then continued for 30 min. Although background noise was detected before adding d-LPA (Figure 23B, pre-addition) — possibly autofluorescence from traces of cell medium components used to culture the cells before the experiment — an increase in the grayscale intensity within the cells was observed 30 min after adding d-LPA (Figure 23B, 30 min after addition). Additionally, the distribution of the signal (circular pattern) suggests that LPA may be localized to specific organelle; however, further studies using specific dyes for the different organelles will have to be performed. Thus, these first experiments showed d-LPA and CARS microscopy as a possible approach to study the distribution of intracellular LPA inside the cell.

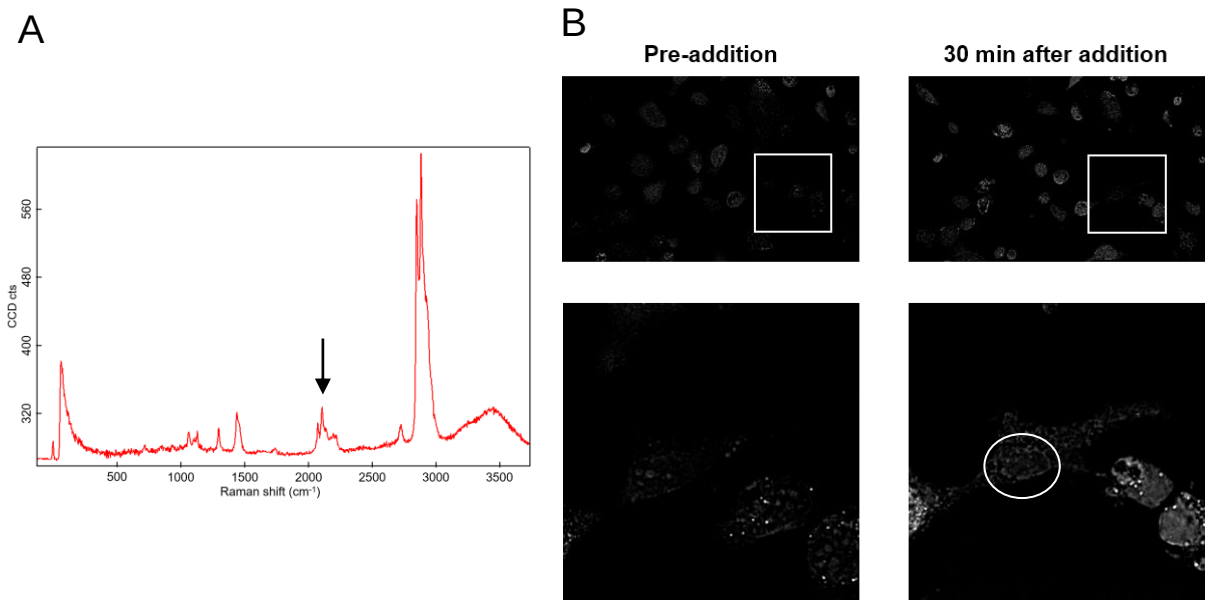

Figure 23 Visualization of 1-palmitoyl-d_9 lysophosphatidic acid (d-LPA) with coherent anti-Stokes Raman scattering (CARS) microscopy. A) Raman spectrum of the molecule d-LPA showing the intensity of the Raman shift in CCD counts (CCD cts) and with a black arrow pointing towards the 2104 cm^{-1} Raman shift selected for subsequent CARS microscopy experiments. The Raman spectrum was determined in two independent experiments. B) CARS microscopy images of ovarian cancer COV318 cells at 2104 cm^{-1} before adding d-LPA (pre-addition) and after 30 min incubation with d-LPA (30 min after addition) with a white circle surrounding a circular pattern observed after adding d-LPA. Representative images of two biological replicates are shown.

3.8.2 Identification of intracellular LPA-binding protein candidates

Since the results presented so far suggest that intracellular LPA is not exported into the extracellular space, the direct interaction of intracellular LPA with proteins in the cell could be responsible for the observed effects in this PhD thesis. Therefore, an LPA-protein pull-down assay was established and used together with subsequent MS-based protein identification to identify intracellular LPA-binding proteins.

The LPA-protein pull-down was based on the use of control agarose beads (control beads) and LPA-coated agarose beads (LPA beads) (Echelon Biosciences). Briefly, cell lysates from ovarian cancer cell lines were incubated with either control beads or LPA beads. Then, the bound proteins were eluted. Following elution, two separate experimental approaches were used. In initial attempts, the bound proteins were separated by SDS-PAGE and stained, and bands indicating specific interactions (intensity of LPA band higher than control band) were cut out and analyzed by peptide fragmentation fingerprinting (Section 2.23.2). However, due to limitations by the visual evaluation of band intensities, as well as high levels of keratin contamination observed in the MS-based protein identification, most probably from the SDS-

PAGE gel, this approach was not further pursued (results summarized in Supplemental material. The LPA-protein pull-down and peptide fragmentation fingerprinting).

In the second approach, the identification of specific LPA-protein interactions was instead based on the use of the sequential window acquisition of all theoretical fragment ion mass spectra (SWATH-MS) at the Bioanalytics department at IfADo (Section 2.23.3), not requiring electrophoresis to first separate the proteins but instead providing quantitative peptide as well as protein-level data (Ludwig et al. 2018). The sum of the integrated peak areas of the proteotypic peptides were computed, and this sum of areas was then used to identify LPA-protein interactions. Briefly, ES-2 protein solutions were mixed with control or LPA beads; these solutions containing beads and proteins were incubated to allow the interaction of the proteins with the beads. Then, the beads were washed to remove unbound proteins and finally the retained proteins were eluted and identified by SWATH-MS for three biological replicates per condition.

Data analysis was first done on the peptide level, detecting a total of 51 proteotypic peptides (Table 17). As can be seen in Table 17, only two peptides were detected in sample ‘C-1’, which suggests a reduction in the protein extraction and/or LPA-protein pull-down efficiency. Looking closer at the total ion chromatograms, much higher level of polyethylene-glycol-(PEG)-based polymer contamination was observed in C-1 (Figure 24), which then suppresses the actual protein signals (Annesley 2003). Because of this, C-1 was excluded from further analysis.

Table 17 Proteotypic peptides detected by the sequential window acquisition of all theoretical fragment ion mass spectra (SWATH-MS). Accession code of the related protein for each proteotypic peptide is presented together with the integrated peak area of the respective peptide detected in the eluate from control beads (C) or LPA beads (LPA) from three biological replicates. The abbreviation ND stands for not detected.

Proteotypic peptide	**C-1**	**C-2**	**C-3**	**LPA-1**	**LPA-2**	**LPA-3**
sp|O60814|H2B1K_HUMAN/ sp|P06899|H2B1J_HUMAN/ sp|P23527|H2B1O_HUMAN/ sp|P33778|H2B1B_HUMAN/ sp|P57053|H2BFS_HUMAN/ sp|P58876|H2B1D_HUMAN/ sp|P62807|H2B1C_HUMAN/ sp|Q16778|H2B2E_HUMAN/ sp|Q5QNW6|H2B2F_HUMAN/ sp|Q8N257|H2B3B_HUMAN/ sp|Q93079|H2B1H_HUMAN/ sp|Q99877|H2B1N_HUMAN/ sp|Q99879|H2B1M_HUMAN/ sp|Q99880|H2B1L_HUMAN QVHPDTGISSK	ND	98997	102130	ND	131880	91679
sp|O60814|H2B1K_HUMAN/ sp|P06899|H2B1J_HUMAN/ sp|P23527|H2B1O_HUMAN/ sp|P33778|H2B1B_HUMAN/ sp|P57053|H2BFS_HUMAN/ sp|P58876|H2B1D_HUMAN/ sp|P62807|H2B1C_HUMAN/ sp|Q16778|H2B2E_HUMAN/ sp|Q5QNW6|H2B2F_HUMAN/ sp|Q8N257|H2B3B_HUMAN/ sp|Q93079|H2B1H_HUMAN/ sp|Q99877|H2B1N_HUMAN/ sp|Q99879|H2B1M_HUMAN/ sp|Q99880|H2B1L_HUMAN AMGIMNSFVNDIFER	ND	101320	47163	5310	139300	46636
sp|P02768|ALBU_HUMAN LVNEVTEFAK	103510	ND	ND	ND	ND	ND
sp|P02768|ALBU_HUMAN YLYEIAR	ND	252160	679970	2023900	483040	310000
sp|P02768|ALBU_HUMAN YICENQDSISSK	ND	90067	427650	566460	267880	68069
sp|P02768|ALBU_HUMAN KVPQVSTPTLVEVSR	ND	394070	705480	ND	ND	621660
sp|P02768|ALBU_HUMAN CCTESLVNR	ND	92638	340250	374660	180570	178740

sp|P04908|H2A1B_HUMAN/ sp|P0C0S8|H2A1_HUMAN/ sp|P20671|H2A1D_HUMAN/ sp|Q16777|H2A2C_HUMAN/ sp|Q6FI13|H2A2A_HUMAN/ sp|Q7L7L0|H2A3_HUMAN/ sp|Q93077|H2A1C_HUMAN/ sp|Q96KK5|H2A1H_HUMAN/ sp|Q99878|H2A1J_HUMAN/ sp|Q9BTM1|H2AJ_HUMAN AGLQFPVGR	ND	449620	439030	ND	339630	423660
sp|P04908|H2A1B_HUMAN/ sp|P0C0S8|H2A1_HUMAN/ sp|P20671|H2A1D_HUMAN/ sp|Q16777|H2A2C_HUMAN/ sp|Q6FI13|H2A2A_HUMAN/ sp|Q7L7L0|H2A3_HUMAN/ sp|Q93077|H2A1C_HUMAN/ sp|Q96KK5|H2A1H_HUMAN/ sp|Q99878|H2A1J_HUMAN/ sp|Q9BTM1|H2AJ_HUMAN VTIAQGGVLPNIQAVLLPK	ND	427030	194250	25544	653170	296760
sp|P06702|S10A9_HUMAN NIETIINTFHQYSVK	ND	8416	8526	26544	1995400	135290
sp|P06702|S10A9_HUMAN QLSFEEFIMLMAR	ND	29451	5411	16774	237560	14671
sp|P06702|S10A9_HUMAN LTWASHEK	ND	15584	61188	58416	409350	42790
sp|P07339|CATD_HUMAN ISVNNVLPVFDNLMQQK	ND	24073	13656	18320	556970	27131
sp|P07339|CATD_HUMAN LVDQNIFSFYLSR	ND	ND	49251	ND	1322400	79103
sp|P07339|CATD_HUMAN VGFAEAAR	ND	25122	46244	34055	810420	29825
sp|P08670|VIME_HUMAN SYVTTSTR	ND	140590	114320	12498	269610	141730
sp|P08670|VIME_HUMAN VELQELNDR	76630	ND	ND	ND	ND	ND
sp|P08670|VIME_HUMAN FANYIDK	ND	209200	158170	12823	384750	178830
sp|P08670|VIME_HUMAN LGDLYEEEMR	ND	278670	233360	ND	593400	126010
sp|P08670|VIME_HUMAN QVDQLTNDK	ND	172260	141340	16585	295630	135780
sp|P08670|VIME_HUMAN EEAENTLQSFR	ND	289410	59242	ND	464450	222230
sp|P08670|VIME_HUMAN QDVDNASLAR	ND	183310	150900	16245	356350	177960
sp|P08670|VIME_HUMAN FADLSEAANR	ND	371970	309100	21502	739960	353830

sp|P08670|VIME_HUMAN LQDEIQNMKEEMAR	ND	157400	6996	ND	6645	103780
sp|P08670|VIME_HUMAN ISLPLPNFSSLNLR	ND	434130	173290	23786	945150	356840
sp|P08670|VIME_HUMAN DGQVINETSQHHDDLE	ND	234340	120830	ND	296720	49438
sp|P14923|PLAK_HUMAN LLNDEDPVVVTK	ND	66826	36455	261780	14954	86235
sp|P14923|PLAK_HUMAN LIILANGGPQALVQIMR	ND	69040	26724	216350	46142	196380
sp|P14923|PLAK_HUMAN LNTIPLFVQLLYSSVENIQR	ND	33817	24502	30655	18880	26293
sp|P14923|PLAK_HUMAN NEGTATYAAAVLFR	ND	101100	102390	233140	41803	104670
sp|P14923|PLAK_HUMAN VSVELTNSLFK	ND	68897	62573	252340	7905	283460
sp|P31151|S10A7_HUMAN SIIGMIDMFHK	ND	ND	ND	ND	604940	40826
sp|P31151|S10A7_HUMAN KIDFSEFLSLLGDIATDYHK	ND	ND	ND	ND	83720	ND
sp|P47929|LEG7_HUMAN LDTSEVVFNSK	ND	ND	ND	ND	ND	ND
sp|P47929|LEG7_HUMAN GQPFEVLIIASDDGFK	ND	38658	17464	160910	66039	92860
sp|P60709|ACTB_HUMAN/ sp|P63261|ACTG_HUMAN GYSFTTTAER	ND	53486	87829	177490	107220	158870
sp|P60709|ACTB_HUMAN/ sp|P63261|ACTG_HUMAN SYELPDGQVITIGNER	ND	66649	36840	243930	94935	228800
sp|P60709|ACTB_HUMAN/ sp|P63261|ACTG_HUMAN EITALAPSTMK	ND	40801	56833	53685	94326	158710
sp|P62805|H4_HUMAN ISGLIYEETR	ND	323060	368470	ND	646840	321520
sp|P62805|H4_HUMAN VFLENVIR	ND	432220	432020	ND	829310	402260
sp|P68104|EF1A1_HUMAN/ sp|Q5VTE0|EF1A3_HUMAN YYVTIIDAPGHR	ND	123100	89041	ND	ND	17894
sp|P68104|EF1A1_HUMAN/ sp|Q5VTE0|EF1A3_HUMAN EHALLAYTLGVK	ND	126910	ND	ND	ND	30956
sp|P68104|EF1A1_HUMAN/ sp|Q5VTE0|EF1A3_HUMAN IGGIGTVPVGR	ND	301340	507810	ND	148130	103000
sp|P68104|EF1A1_HUMAN/ sp|Q5VTE0|EF1A3_HUMAN QTVAVGVIK	ND	151650	221540	27995	50025	53729

sp|Q8TDL5|BPIB1_HUMAN EKPAGGIPVLGSLVNTVLK	ND	ND	ND	ND	ND	64532
sp|Q8TDL5|BPIB1_HUMAN LSFLVNALAK	ND	ND	ND	ND	ND	77713
sp|Q8TDL5|BPIB1_HUMAN QVMNLLVPSLPNLVK	ND	ND	ND	ND	ND	41938
sp|Q8TDL5|BPIB1_HUMAN SSIGLINEK	ND	ND	ND	ND	ND	82755
sp|Q8TDL5|BPIB1_HUMAN IQLMNSGIGWFQPDVLK	ND	ND	ND	ND	ND	57231
sp|Q6UWP8|SBSN_HUMAN FGQGVDNAAGQAGNEAGR	ND	ND	ND	ND	ND	19069
sp|Q6UWP8|SBSN_HUMAN FGQGAHHAAGQAGNEAGR	ND	ND	ND	6261	ND	62706

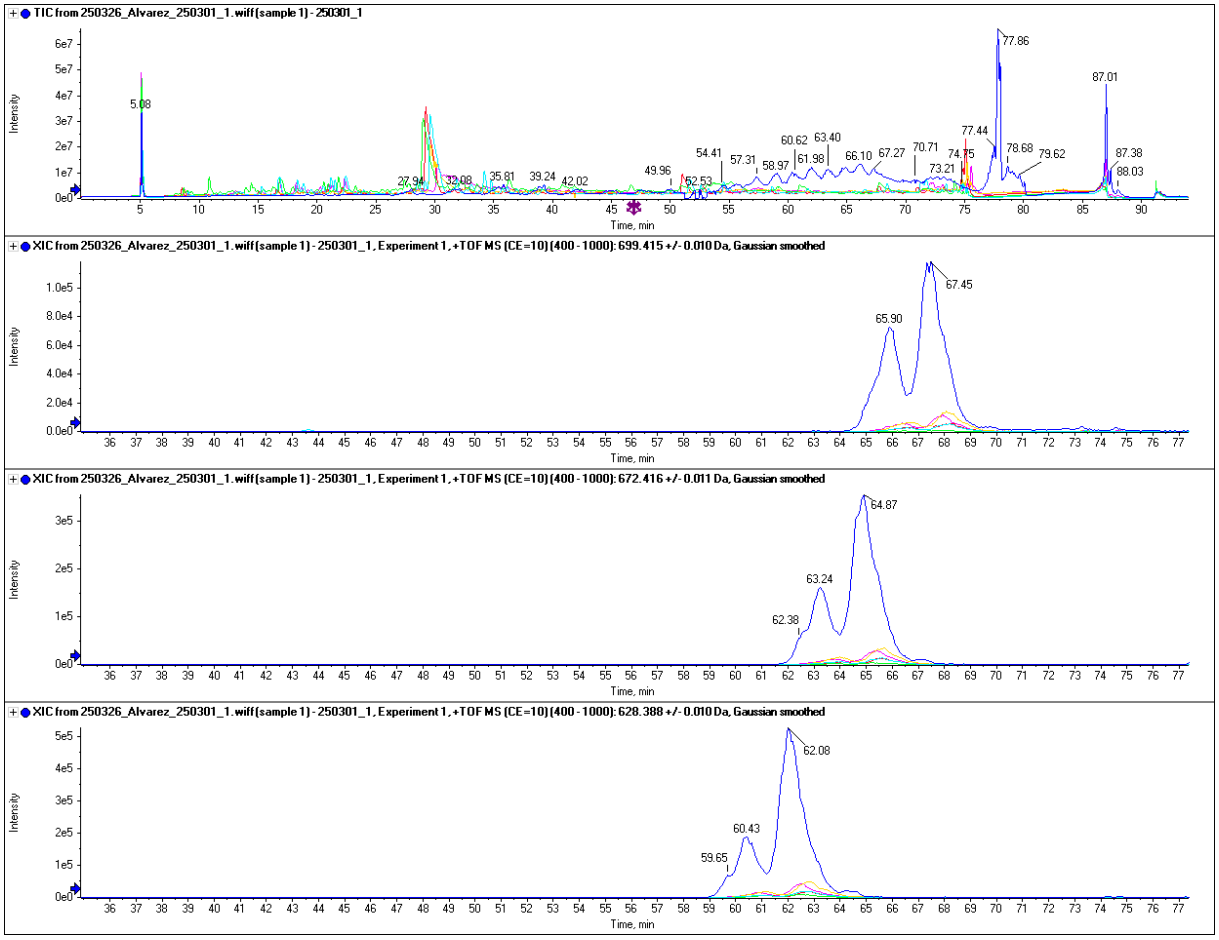

Figure 24 Ion chromatograms of the analyzed samples in the sequential window acquisition of all theoretical fragment ion mass spectra (SWATH-MS). The top panel shows the overlaid total ion chromatograms of the six samples. Intense signals derived from polyethylene-glycol-(PEG)-based polymers were obtained in sample C-1 (blue), most prominently in the retention time between 50 and 75 min. The lower panels show the extracted ion chromatograms of individual PEG-oligomers. Very intense signals were obtained for the sample C-1 (blue).

The peptide data was then summarized per protein, detecting a total of 14 proteins that interacted either with the LPA beads alone or with both control and LPA beads (Table 18). Three pulled-down proteins were detected to only interact with LPA beads, including S100 calcium-binding protein A7 (S100A7), BPI fold-containing family B member 1 (BPIFB1) and suprabasin (SBSN) (Table 18). S100A7 is a small calcium-binding protein first described in psoriatic keratinocytes (Sood et al. 2022). The protein BPIFB1 is secreted and has been linked to the innate immunity (Shin et al. 2011), while the role of SBSN, first characterized in the cornified envelope, remains unknown (Pribyl, Hodny, and Kubikova 2021). Interestingly, the three previously mentioned proteins have also been linked to cancer (Glazer et al. 2009; Nasser et al. 2012; Wei et al. 2018). However, these proteins were not detected to bind to LPA in all three biological replicates, and the results should therefore be interpreted with caution, and more importantly confirmed in independent experiments.

The other pulled-down proteins interacted with both control and LPA beads (Table 18), and the most relevant from among them was actin (ACTB/ACTG), where a stronger signal was observed for LPA beads compared to control beads (Table 18), a difference that was statistically significant (Figure 25). Both actin isoforms (ACTB and ACTG) are important components of the cytoskeleton and relevant for cell migration, thus having a link between LPA and cell migration.

Table 18 Summary of the peptide data per protein from the sequential window acquisition of all theoretical fragment ion mass spectra (SWATH-MS). Accession code of each protein is presented together with the sum of the integrated peak areas of the respective proteotypic peptides detected in the eluate from control beads (C) or LPA beads (LPA) from two to three biological replicates. The abbreviation ND stands for not detected. *Missing value (ND) was imputed as median - (2 · standard deviation) for the corresponding condition/protein.

Protein	C-2	C-3	Mean	Standard deviation	LPA-1	LPA-2	LPA-3	Mean	Standard deviation
sp|P31151|S10A7_HUMAN	ND	ND			ND	688660	40826	364743	458088
sp|Q8TDL5|BPIB1_HUMAN	ND	ND			ND	ND	324170		
sp|Q6UWP8|SBSN_HUMAN	ND	ND			6261	ND	81775	44018	53396
sp|O60814|H2B1K_HUMAN/ sp|P06899|H2B1J_HUMAN/ sp|P23527|H2B1O_HUMAN/ sp|P33778|H2B1B_HUMAN/ sp|P57053|H2BFS_HUMAN/ sp|P58876|H2B1D_HUMAN/ sp|P62807|H2B1C_HUMAN/ sp|Q16778|H2B2E_HUMAN/ sp|Q5QNW6|H2B2F_HUMAN/ sp|Q8N257|H2B3B_HUMAN/ sp|Q93079|H2B1H_HUMAN/ sp|Q99877|H2B1N_HUMAN/ sp|Q99879|H2B1M_HUMAN/ sp|Q99880|H2B1L_HUMAN	200320	149300	174810	36077	5310	271180	138320	138270	132935
sp|P02768|ALBU_HUMAN	828930	2153300	1491115	936471	2965000	931490	1178500	1691663	1109637
sp|P04908|H2A1B_HUMAN/ sp|P0C0S8|H2A1_HUMAN/ sp|P20671|H2A1D_HUMAN/ sp|Q16777|H2A2C_HUMAN/ sp|Q6FI13|H2A2A_HUMAN/ sp|Q7L7L0|H2A3_HUMAN/ sp|Q93077|H2A1C_HUMAN/ sp|Q96KK5|H2A1H_HUMAN/ sp|Q99878|H2A1J_HUMAN/ sp|Q9BTM1|H2AJ_HUMAN	876650	633280	754965	172089	25544	992800	720420	579588	498770
sp|P06702|S10A9_HUMAN	53450	75125	64288	15327	101730	2642300	192750	978927	1441242
sp|P07339|CATD_HUMAN	49195	109150	79173	42395	52376	2689800	136060	959412	1499144
sp|P08670|VIME_HUMAN	2471300	1467500	1969400	709794	103440	4352700	1846400	2100847	2136027
sp|P14923|PLAK_HUMAN	339680	252640	296160	61547	994260	129680	697040	606993	439268
sp|P47929|LEG7_HUMAN	38658	17464	28061	14986	160910	66039	92860	106603	48906
sp|P60709|ACTB_HUMAN/ sp|P63261|ACTG_HUMAN	160940	181500	171220	14538	475110	296480	546380	439323	128736
sp|P62805|H4_HUMAN	755280	800480	777880	31961	*35907	1476200	723780	1099990	532041
sp|P68104|EF1A1_HUMAN/ sp|Q5VTE0|EF1A3_HUMAN	703000	818390	760695	81593	27995	198160	205580	143912	100455

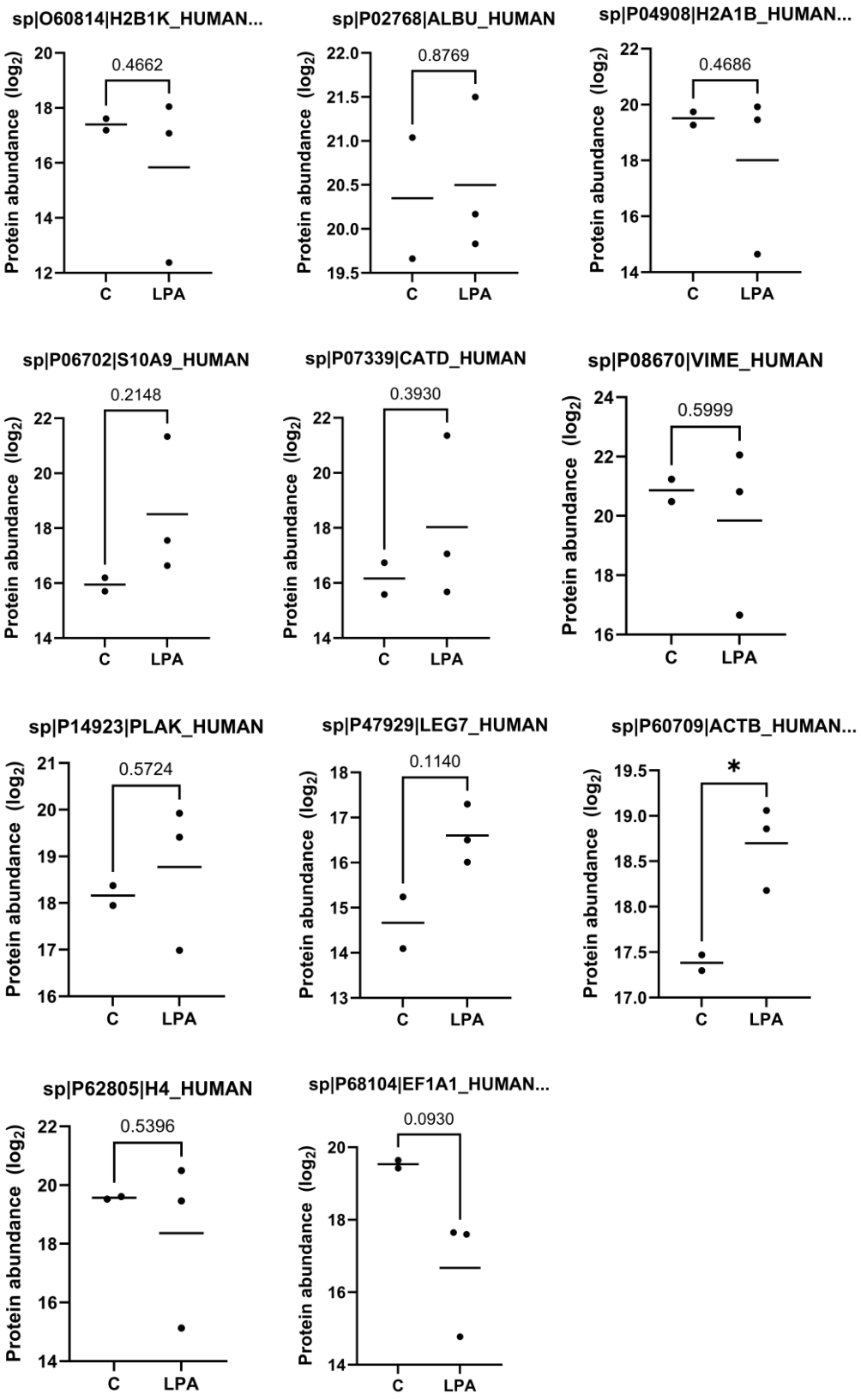

Figure 25 Actin was the most relevant protein among the detected pulled-down proteins which interacted with both control and LPA beads. Summary of the peptide data per protein from the sequential window acquisition of all theoretical fragment ion mass spectra (SWATH-MS) from two to three biological replicates was log_2-transformed (herein called protein abundance) and the statistical difference of the protein abundance between proteins eluted either from control beads (C) or LPA beads (LPA) was analyzed by t-test. *, $p < 0.05$.

4 Discussion

Ovarian cancer is the seventh most common cancer in women with a five-year relative survival rate of just 29% (Reid, Permuth, and Sellers 2017), since this type of cancer usually manifests severe symptoms at later stages, when the primary tumor has already metastasized, and to date reliable screening methods for early detection are not available (Berek et al. 2021). The glycerophospholipid LPA has been reported to be a relevant factor in different pathologies, including ovarian cancer. For example, LPA secreted by peritoneal cells was shown to enhance migration, adhesion and invasion of ovarian cancer cells (Ren et al. 2006). Additionally, the silencing of extracellular LPA receptors in ovarian cancer cells reduced their migration and invasiveness (Yu et al. 2008). Nevertheless, scientists have mainly focused on extracellular LPA as a signaling lipid that binds G protein-coupled receptors on the cell surface to mediate intracellular signaling that in turn regulates cell function, many of which are deregulated in cancer. However, LPA is also produced inside the cell as an important metabolic intermediate in the novo glycerophospholipid and triacylglycerol synthesis. For example the glycerol-3-phosphate acyltransferases, important regulators in the novo glycerophospholipid and triacylglycerol synthesis, catalyze the acylation of glycerol-3-phosphate with acyl-CoAs to produce LPA (Yamashita, Hayashi, Matsumoto, et al. 2014). Among the different glycerol-3-phosphate acyltransferase isoforms, GPAM has been extensively investigated in several diseases, including metabolic disorders and cancer. However, little is still known about its role in the latter. For example, the expression of GPAM was associated with worse outcome in ovarian cancer patients (Marchan et al. 2017). Additionally, silencing GPAM in breast, endometrioid and ovarian cancer cell lines reduced cell migration, as well as subcutaneous tumor growth in a xenograft mouse model (Gonscharow 2025; Marchan et al. 2017). Moreover, the knockdown of GPAM decreased proliferation and invasiveness of bile duct cancer cell lines (Zhang et al. 2022), as well as the proliferation of several acute myeloid leukemia cell lines (Irifune et al. 2023). Nonetheless, the role of GPAM in cancer metastasis has not been yet explored in vivo.

4.1 The effect of knocking down GPAM or inhibiting GPAM with the GPAT inhibitor FSG67 on cancer-relevant processes in vitro

In order to evaluate the function of GPAM in cancer metastasis in vivo, two approaches were planned to target GPAM in vivo: stable knockdown of GPAM using lentiviral shRNA tech-

nology and the GPAM inhibitor FSG67. However, the above mentioned approaches were evaluated first in vitro in relation to their effect on cancer-relevant processes in ovarian cancer cell lines before moving to in vivo mouse models. Specifically, collective cell migration, individual cell migration, number and size of colonies and resistance to anoikis were evaluated when GPAM was targeted with the lentiviral shRNA technology and the GPAM inhibitor FSG67. Work done in this PhD thesis could show that targeting GPAM, either with lentiviral shRNA technology or with FSG67, alter cancer-relevant processes in vitro. Nonetheless, different patterns were observed although the same enzyme was targeted.

Collective cell migration is the movement of cells as a group instead of as single cells (Rorth 2009). This collective cell migration can be performed by different cell types under physiological conditions, as well as cancer cells during invasion (Rorth 2009). To investigate the role of GPAM on collective cell migration, GPAM was silenced in ES-2 cells and their collective cell migration was studied using the wound closure assay. The GPAM silencing was showed to reduce collective cell migration in ES-2 cells. These results are in line with previous studies, where transient knockdown of GPAM using siRNA technology in ES-2 cells resulted in a decrease of collective cell migration (Marchan et al. 2017). Additionally, the same effect was observed using the MCF7, MDA-MB-231 and HeLa cancer cells (Marchan et al. 2017). Moreover, the GPAM inhibition with FSG67 was showed to reduce collective cell migration in ES-2 cells, as well as in OVCAR8 cells. Taken together, GPAM seems to be important in the collective cell migration of cancer cells.

Individual cell migration was also studied — a process that is important in cancer-related processes such as detachment, invasion and metastasis (Friedl and Wolf 2003) — using the transwell assay. Interestingly, silencing GPAM in ES-2 cells did not significantly influence individual cell migration; whereas FSG67 strongly reduced the individual cell migration. GPAM knockdown was performed using shRNA technology which triggers the specific RNA interference process against the targeted gene (Stewart et al. 2003). In contrast, FSG67 was developed as a competitive inhibitor of the GPAT enzymes using the catalytic region of GPAM (Wydysh et al. 2009). The catalytic regions of the GPAT enzymes GPAT1 (GPAM), GPAT2, GPAT3 and GPAT4 show high homology (Yamashita, Hayashi, Matsumoto, et al. 2014). Thus, the observed reduction in individual cell migration in ES-2 cells with FSG67 could have been the effect of FSG67 on all GPATs.

The capability of tumor cells to proliferate indefinitely is a basic characteristic of cancer cells (Hanahan and Weinberg 2011), since it promotes cancer development and metastasis. Thus, the colony forming capacity of ES-2 cells was studied after either GPAM knockdown or treatment with FSG67 (Franken et al. 2006). The size of the ES-2 colonies was unaffected in both cases. In contrast, the GPAM knockdown reduced the number of ES-2 colonies, but not the FSG67 treatment. The GPAM knockdown is designed to specifically target *GPAM*. But as mentioned in the previous paragraph, FSG67 can potentially interact with any of the GPATs. Thus, the interaction of FSG67 with any other GPAT rather than GPAM might have reduced the available pool of FSG67 molecules to interact with GPAM and therefore the number of FSG67 molecules needed to observe a reduction in the number of ES-2 colonies was not reached. If the explained mechanism is the reason of the observed phenotype in the number of ES-2 colonies, an increase in the concentration of FSG67 might allow to reach the number of FSG67 molecules interacting with GPAM to observe a reduction in the number of ES-2 colonies. And this increase should be close to the lowest IC_{20} value in ES-2 cells (IC_{20} = 283.90 µM, Figure 14B) in order to avoid that the cytotoxicity of FSG67 obscures other relevant processes which produce the reduction in the number of ES-2 colonies.

Finally, anoikis is the cell death program triggered when cells detach from the extracellular matrix (Frisch and Francis 1994). The resistance to anoikis facilitates metastasis and thus it was evaluated if the GPAM knockdown and the inhibition of GPAM with FSG67 altered the resistance of ovarian cancer cells to activate anoikis. GPAM knockdown in ES-2 cells had no effect on anoikis resistance, whereas the treatment with FSG67 did so. As mentioned previously regarding the individual cell migration of ES-2 cells, the observed effect on anoikis resistance in ES-2 cells with FSG67 could have been an effect of FSG67 acting on the other GPATs. In fact, Corbet et al. reported that lipid droplets can support anoikis resistance (Corbet et al. 2020). Additionally, Kuhajda et al. showed a reduction in the number and size of lipid droplets in 373-L1 adipocytes when treated with FSG67 (Kuhajda et al. 2011). Since the four GPATs catalyze the first step in de novo glycerophospholipid and triacylglycerol (TAG) synthesis, and TAG can be stored in lipid droplets (Yamashita, Hayashi, Matsumoto, et al. 2014; Yu et al. 2018), the ability of FSG67 to potentially interact with the four GPATs might have produced a synergistic inhibition of the four enzymes in ES-2 cells, which was more effective in preventing the formation of lipids droplets than the solely knockdown of GPAM.

4.2 The cytotoxicity of FSG67 in different cell lines

The stable GPAM knockdown was evaluated in vivo with a cell line-derived xenograft model of peritoneal metastasis, and bioluminescence signal measurements suggested that GPAM may play a role in ovarian cancer metastasis. Further discussion of this result is presented in Section 4.4 below. But for next preclinical studies FSG67 was considered as a more relevant method to inhibit GPAM. Since no information existed regarding the cytotoxicity of FSG67 in ovarian cancer cells, an in vitro cell-viability study of FSG67 was performed to evaluate possible concentrations for following experiments. Viral-transformed ovarian surface epithelial and ovarian cancer cells were incubated with increasing concentrations of FSG67 for 24 and 48 h and their viability determined, which was fitted to a logistic model to calculate the inhibitory concentrations (IC) IC_{20} and IC_{50}. These values were used as a guidance to determine suitable FSG67 concentrations to use when studying the effect of the compound on cancer-relevant cell processes.

The sensitivity of cells to FSG67 seems to be cell line-dependent. McFadden and coauthors showed a significant although slight decrease of approximately 10% viability in primary hypothalamic neurons after a 24 h treatment with 320 µM FSG67 (McFadden et al. 2014). In this work, a 24 h treatment with 316 µM FSG67 led to approximately the same reduction in viability in the tested ovarian cells. In contrast, Irifune et al. reported a loss of approximately 20% and 40% viability in $CD34^+$ acute myeloid leukemia cells when treated for 48 h with 80 and 120 µM FSG67, respectively (Irifune et al. 2023). Herein at least 231.33 µM FSG67 was needed to observe a loss of 20% viability in the tested ovarian cell lines when treated for 48 h.

4.3 The detected proteins with the LPA-protein pull-down

To understand the mechanism by which GPAM influences cancer cell processes, its enzymatic product LPA was studied in relation to its autocrine and/or paracrine signaling and protein interaction partners. Mass spectrometry analyses using ^{13}C-LPA revealed that intracellular LPA is not exported into the extracellular space. Therefore, an LPA-protein pull-down was established with a subsequent SWATH-MS analysis to find possible intracellular LPA-binding proteins. Following this approach, the proteins S100 calcium-binding protein A7 (S100A7), BPI fold-containing family B member 1 (BPIFB1), suprabasin (SBSN) and actin (ACTB/ACTG) were identified as LPA-binding protein candidates. The LPA-protein pull-down was based on the use of control agarose beads (control beads) and agarose beads coated

with LPA (LPA beads), which were incubated with extracted proteins from ovarian cancer cells, and the bound proteins were eluted. After the elution, the SWATH-MS provided quantitative data of the detected proteins interacting with either the control or LPA beads. The sum of the integrated peak areas of the proteotypic peptides was used as a measurement of the amount of protein which interacted with the control or the LPA beads. On the one hand, the proteins S100 calcium-binding protein A7 (S100A7), BPI fold-containing family B member 1 (BPIFB1) and suprabasin (SBSN) were detected to interact with just the LPA beads, suggesting that these proteins specifically interacted with LPA. On the other hand, actin (ACTB/ACTG) was detected to interact with control and LPA beads, but the interaction with the LPA beads was stronger and significantly different compared to the interaction with the control beads, suggesting that actin specifically interacted with LPA.

The detected proteins S100 calcium-binding protein A7 (S100A7), BPI fold-containing family B member 1 (BPIFB1), suprabasin (SBSN) and actin (ACTB/ACTG) have already been related to cancer. S100A7 was shown to increase breast cancer cells proliferation through inflammatory pathways (Nasser et al. 2012). More specifically, the study showed that overexpression of S100A7 in in vitro and in vivo models led to an increase in breast cancer cell growth, upregulation of proinflammatory molecules and enhancement of tumor growth (Nasser et al. 2012). More recently, S100A7 was also proposed as a potential biomarker to distinguish between malignant disorders and oral squamous cell carcinoma (Sood et al. 2022). Similar to S100A7, BPIFB1 was shown to enhance metastasis of breast cancer cells by activating macrophage M2 polarization (Hu et al. 2023). In contrast, Wei et. al reported that BPIFB1 was downregulated in nasopharyngeal carcinoma compared to a healthy nasopharynx and its low expression was associated with worse outcome in nasopharyngeal carcinoma patients (Wei et al. 2018). Additionally, overexpression of the *BPIFB1* gene in nasopharyngeal carcinoma cells led to their sensitization to radiation (Wei et al. 2018). Regarding SBSN, although its function is not known (Pribyl, Hodny, and Kubikova 2021), extensive research of SBSN related to cancer has been performed, linking the protein to different types of cancer, such as lung cancer (Glazer et al. 2009), esophageal squamous carcinoma (Jiang et al. 2018) or glioblastoma multiforme (Formolo et al. 2011). Finally, actin, a key cytoskeletal protein that forms cellular microfilaments, plays a key role in cell migration. Actin microfilaments form membrane protrusions such as lamellipodia or invadopodia, which are key cellular structures that facilitate cancer cell migration and invasion (Yamaguchi and Condeelis 2007). Additionally, the epithelial-to-mesenchymal transition (EMT) is fundamental for the develop-

ment of metastasis, which is dependent on the reorganization of cellular actin microfilaments structure (Izdebska et al. 2018). LPA may be directly related to the polymerization of actin microfilaments, as it was shown that LPA can interact with the complex between actin and the actin-binding protein gelsolin, and removes gelsolin at the actin microfilament ends of human platelets, which allows the polymerization of actin microfilaments (Davoudian et al. 2023; Meerschaert et al. 1998).

4.4 Future perspectives

Previous studies have used different mouse tumor models to study how silencing GPAM or inhibiting GPAM with the GPAT inhibitor FSG67 affected the development of the tumor (Irifune et al. 2023; Yao et al. 2023). Nonetheless, these studies were based on subcutaneous tumor models, which in general are not applicable to study metastasis (Stribbling and Ryan 2022). Using a peritoneal metastasis model this work is one of the first, which shows that targeting GPAM may be relevant in ovarian cancer metastasis. These initial studies were performed using stably transfected ovarian cancer cells. Additionally, the GPAT inhibitor FSG67 — a more relevant method for preclinical studies to inhibit GPAM — was shown to hinder cancer-relevant processes in vitro, which supports its applicability for subsequent in vivo studies. Moreover, the established LPA-pull down method with the subsequent SWATH-MS points to novel LPA-binding proteins that may provide insight into the mechanism of how GPAM influences cancer cell processes. Nonetheless, subsequent experiments must be performed to further confirm these results.

Internal organs of the cell line-derived xenograft (CDX) models were collected at the end of the experiment and snap frozen in liquid nitrogen for later analyses. RNA sequencing (RNA-seq), proteomics and metabolomics of the collected organs could be performed to detect differences between the control and the GPAM knockdown CDX organs. For example, the omentum is one of the most common sites of ovarian cancer metastasis (Dvoretsky et al. 1988; Reed et al. 2000) and ovarian cancer cells transform the site of metastasis to facilitate their proliferation (Lengyel 2010). Thus, the control and the GPAM knockdown CDX omenta could be compared with these omics methods to uncover differences in this site of metastasis due to the GPAM knockdown intervention. Nevertheless, although with a different pattern, the bioluminescence in the control and GPAM knockdown CDX models decreased in the last weeks of the experiment, what complicated the evaluation of the results. Several nonexclusive

approaches could be considered to address this situation. This PhD thesis used in vivo one out of three cell lines created with GPAM stably silenced, namely ES-2_luc shGPAM1. ES-2_luc shGPAM2 and ES-2_luc shGPAM3 might still be used to establish CDX models to study ovarian cancer metastasis. In another approach, the experiment could be extended for a longer time period in order to allow the cancer cells either to develop into growing tumors or to be completely extinguished. And finally, herein CD-1 nude mice were used to establish the CDX models. More immunodeficient mouse strains, such as the NOD scid gamma (NSG) or Rag2/IL2RG double knockout (R2G2) mouse strain could be used to increase the efficacy of metastasis formation.

Initial toxicology and pharmacokinetic studies of FSG67 in vivo revealed the compound to be safe for in vivo applications and reaching blood concentrations proven to be effective to hinder cancer-relevant cell processes in vitro. Thus, next the antitumor efficacy of the compound in a subcutaneous CDX model could be studied. Here, ovarian cancer cells would be injected subcutaneously into female immunodeficient mice and tumors would be allowed to grow until a specific predefined volume. Then, the subcutaneous CDX model mice would be treated intraperitoneally (IP) either with vehicle or 50 mg/kg FSG67 for two weeks, five days on and two days off, and tumor size would be monitored. Additionally, several studies have shown the efficacy of applying intraperitoneal chemotherapy in ovarian cancer patients (Alberts et al. 1996; Armstrong et al. 2006; Nagao et al. 2023). Thus, another interesting approach to study the antitumor efficacy of the compound in vivo would be an in vivo metastases study. In the mentioned study, luciferase-expressing ovarian cancers cells would be injected IP into female immunodeficient mice, and these IP CDX model mice would be treated IP either with vehicle or 50 mg/kg FSG67 for two weeks, five days on and two days off, and bioluminescence would be monitored.

The herein established LPA-pull down method and subsequent SWATH-MS pointed to the novel LPA-binding proteins S100 calcium-binding protein A7 (S100A7), BPI fold-containing family B member 1 (BPIFB1), suprabasin (SBSN) and actin (ACTB/ACTG). Results in this PhD thesis suggested that LPA might not be an autocrine and/or paracrine mediator since intracellular LPA was not exported to the extracellular environment. Based on these results, LPA was hypothesized to interact with intracellular proteins to mediate cancer-relevant processes, and thus the LPA-protein pull-down was used in order to identify these intracellular proteins. From the detected proteins, only actin is exclusively found in the intracellular space

under physiological conditions. S100A7 can be found both in the extracellular and in the intracellular space (Celis et al. 1996), BPIFB1 is secreted to the extracellular space (Li, Xu, et al. 2020) and SBSN is supposed to be secreted based on its protein sequence (Pribyl, Hodny, and Kubikova 2021). Therefore, actin would be the ideal candidate to confirm with following experiments. The LPA-pull down without the SWATH-MS would be performed, and then Western blot would be carried out to detect the presence of actin. The detection of actin in the mentioned Western blot would be further evidence that LPA directly interacts with actin. All in all, these series of experiments will expand our knowledge about the role of GPAM and its product LPA in ovarian cancer and thus provide new opportunities for the treatment of ovarian cancer patients.

5 References

Ahmed, N., and K. L. Stenvers. 2013. 'Getting to know ovarian cancer ascites: opportunities for targeted therapy-based translational research', *Front Oncol*, 3: 256.

Aikawa, S., T. Hashimoto, K. Kano, and J. Aoki. 2015. 'JB Special Review-Recent Progress in Lipid Mediators Lysophosphatidic acid as a lipid mediator with multiple biological actions', *Journal of Biochemistry*, 157: 81-89.

Alberts, D. S., P. Y. Liu, E. V. Hannigan, R. O'Toole, S. D. Williams, J. A. Young, E. W. Franklin, D. L. Clarke-Pearson, V. K. Malviya, and B. DuBeshter. 1996. 'Intraperitoneal cisplatin plus intravenous cyclophosphamide versus intravenous cisplatin plus intravenous cyclophosphamide for stage III ovarian cancer', *N Engl J Med*, 335: 1950-5.

Altman, M. K., V. Gopal, W. Jia, S. X. Yu, H. Hall, G. B. Mills, A. C. McGinnis, M. G. Bartlett, G. W. Jiang, D. Madan, G. D. Prestwich, Y. Xu, M. A. Davies, and M. M. Murph. 2010. 'Targeting melanoma growth and viability reveals dualistic functionality of the phosphonothionate analogue of carba cyclic phosphatidic acid', *Molecular Cancer*, 9: 14.

Annesley, T. M. 2003. 'Ion suppression in mass spectrometry', *Clin Chem*, 49: 1041-4.

Aoki, J., A. Inoue, and S. Okudaira. 2008. 'Two pathways for lysophosphatidic acid production', *Biochim Biophys Acta*, 1781: 513-8.

Armstrong, D. K., B. Bundy, L. Wenzel, H. Q. Huang, R. Baergen, S. Lele, L. J. Copeland, J. L. Walker, R. A. Burger, and Group Gynecologic Oncology. 2006. 'Intraperitoneal cisplatin and paclitaxel in ovarian cancer', *N Engl J Med*, 354: 34-43.

Assidi, M. 2022. 'High N-Cadherin Protein Expression in Ovarian Cancer Predicts Poor Survival and Triggers Cell Invasion', *Front Oncol*, 12: 870820.

Baker, R. R., and H. Y. Chang. 1999. 'Evidence for two distinct lysophospholipase activities that degrade lysophosphatidylcholine and lysophosphatidic acid in neuronal nuclei of cerebral cortex', *Biochim Biophys Acta*, 1438: 253-63.

Bandoh, K., J. Aoki, A. Taira, M. Tsujimoto, H. Arai, and K. Inoue. 2000. 'Lysophosphatidic acid (LPA) receptors of the EDG family are differentially activated by LPA species - Structure-activity relationship of cloned LPA receptors', *Febs Letters*, 478: 159-65.

Banz, C., U. Ungethuem, R. J. Kuban, K. Diedrich, E. Lengyel, and D. Hornung. 2010. 'The molecular signature of endometriosis-associated endometrioid ovarian cancer differs significantly from endometriosis-independent endometrioid ovarian cancer', *Fertil Steril*, 94: 1212-17.

Beigneux, A. P., L. Vergnes, X. Qiao, S. Quatela, R. Davis, S. M. Watkins, R. A. Coleman, R. L. Walzem, M. Philips, K. Reue, and S. G. Young. 2006. 'Agpat6 -: a novel lipid biosynthetic gene required for triacylglycerol production in mammary epithelium', *Journal of Lipid Research*, 47: 734-44.

Bence, K. K., and M. J. Birnbaum. 2021. 'Metabolic drivers of non-alcoholic fatty liver disease', *Mol Metab*, 50: 101143.

Berek, J. S., M. Renz, S. Kehoe, L. Kumar, and M. Friedlander. 2021. 'Cancer of the ovary, fallopian tube, and peritoneum: 2021 update', *Int J Gynaecol Obstet*, 155 Suppl 1: 61-85.

Bese, T., M. Barbaros, E. Baykara, O. Guralp, S. Cengiz, F. Demirkiran, C. Sanioglu, and M. Arvas. 2010. 'Comparison of total plasma lysophosphatidic acid and serum CA-125 as a tumor marker in the diagnosis and follow-up of patients with epithelial ovarian cancer', *Journal of Gynecologic Oncology*, 21: 248-54.

Bishop, W. R., and R. M. Bell. 1988. 'Assembly of phospholipids into cellular membranes: biosynthesis, transmembrane movement and intracellular translocation', *Annual Review of Cell Biology*, 4: 579-610.

Brockmöller, S. F., E. Bucher, B. M. Müller, J. Budczies, M. Hilvo, J. L. Griffin, M. Oresic, O. Kallioniemi, K. Iljin, S. Loibl, S. Darb-Esfahani, B. V. Sinn, F. Klauschen, J. Prinzler, N. Bangemann, F. Ismaeel, O. Fiehn, M. Dietel, and C. Denkert. 2012. 'Integration of Metabolomics and Expression of Glycerol-3-phosphate Acyltransferase (GPAM) in Breast Cancer-Link to Patient Survival, Hormone Receptor Status, and Metabolic Profiling', *Journal of Proteome Research*, 11: 850-60.

Burkhalter, R. J., S. D. Westfall, Y. Liu, and M. S. Stack. 2015. 'Lysophosphatidic Acid Initiates Epithelial to Mesenchymal Transition and Induces β-Catenin-mediated Transcription in Epithelial Ovarian Carcinoma', *J Biol Chem*, 290: 22143-54.

Bustin, S. A., V. Benes, T. Nolan, and M. W. Pfaffl. 2005. 'Quantitative real-time RT-PCR--a perspective', *J Mol Endocrinol*, 34: 597-601.

Cannistra, S. A., G. S. Kansas, J. Niloff, B. DeFranzo, Y. Kim, and C. Ottensmeier. 1993. 'Binding of ovarian cancer cells to peritoneal mesothelium in vitro is partly mediated by CD44H', *Cancer Res*, 53: 3830-8.

Cao, J. S., J. L. Li, D. M. Li, J. F. Tobin, and R. E. Gimeno. 2006. 'Molecular identification of microsomal acyl-CoA:glycerol-3-phosphate acyltransferase, a key enzyme in de novo triacylglycerol synthesis', *Proceedings of the National Academy of Sciences of the United States of America*, 103: 19695-700.

Cao, J. S., S. Perez, B. Goodwin, Q. C. Lin, H. B. Peng, A. Qadri, Y. J. Zhou, R. W. Clark, M. Perreault, J. F. Tobin, and R. E. Gimeno. 2014. 'Mice deleted for GPAT3 have reduced GPAT activity in white adipose tissue and altered energy and cholesterol homeostasis in diet-induced obesity', *American Journal of Physiology-Endocrinology and Metabolism*, 306: E1176-E87.

Cattaneo, E. R., M. Pellon-Maison, M. E. Rabassa, E. Lacunza, R. A. Coleman, and M. R. Gonzalez-Baro. 2012. 'Glycerol-3-Phosphate Acyltransferase-2 Is Expressed in Spermatic Germ Cells and Incorporates Arachidonic Acid into Triacylglycerols', *Plos One*, 7: 11.

Celis, J. E., H. H. Rasmussen, H. Vorum, P. Madsen, B. Honore, H. Wolf, and T. F. Orntoft. 1996. 'Bladder squamous cell carcinomas express psoriasin and externalize it to the urine', *J Urol*, 155: 2105-12.

Chemin, J., A. Patel, F. Duprat, M. Zanzouri, M. Lazdunski, and E. Honoré. 2005. 'Lysophosphatidic acid-operated K+ channels', *J Biol Chem*, 280: 4415-21.

Chen, Y. Q., M. S. Kuo, S. Y. Li, H. H. Bui, D. A. Peake, P. E. Sanders, S. J. Thibodeaux, S. Y. Chu, Y. W. Qian, Y. Zhao, D. S. Bredt, D. E. Moller, R. J. Konrad, A. P. Beigneux, S. G. Young, and G. Q. Cao. 2008. 'AGPAT6 is a novel microsomal glycerol-3-phosphate acyltransferase', *Journal of Biological Chemistry*, 283: 10048-57.

Choi, J. W., D. R. Herr, K. Noguchi, Y. C. Yung, C. W. Lee, T. Mutoh, M. E. Lin, S. T. Teo, K. E. Park, A. N. Mosley, and J. Chun. 2010. 'LPA Receptors: Subtypes and Biological Actions', *Annual Review of Pharmacology and Toxicology*, 50: 157-86.

Coleman, R. A., and D. G. Mashek. 2011. 'Mammalian Triacylglycerol Metabolism: Synthesis, Lipolysis, and Signaling', *Chemical Reviews*, 111: 6359-86.

Coleman, R. L., A. M. Oza, D. Lorusso, C. Aghajanian, A. Oaknin, A. Dean, N. Colombo, J. I. Weberpals, A. Clamp, G. Scambia, A. Leary, R. W. Holloway, M. A. Gancedo, P. C. Fong, J. C. Goh, D. M. O'Malley, D. K. Armstrong, J. Garcia-Donas, E. M. Swisher, A. Floquet, G. E. Konecny, I. A. McNeish, C. L. Scott, T. Cameron, L. Maloney, J. Isaacson, S. Goble, C. Grace, T. C. Harding, M. Raponi, J. Sun, K. K. Lin, H. Giordano, J. A. Ledermann, and Ariel investigators. 2017. 'Rucaparib maintenance treatment for recurrent ovarian carcinoma after response to platinum therapy (ARIEL3): a randomised, double-blind, placebo-controlled, phase 3 trial', *Lancet*, 390: 1949-61.

Corbet, C., E. Bastien, J. P. Santiago de Jesus, E. Dierge, R. Martherus, C. Vander Linden, B. Doix, C. Degavre, C. Guilbaud, L. Petit, C. Michiels, C. Dessy, Y. Larondelle, and O. Feron. 2020. 'TGFbeta2-induced formation of lipid droplets supports acidosis-driven EMT and the metastatic spreading of cancer cells', *Nat Commun*, 11: 454.

Curley, M. D., L. A. Garrett, J. O. Schorge, R. Foster, and B. R. Rueda. 2011. 'Evidence for cancer stem cells contributing to the pathogenesis of ovarian cancer', *Front Biosci (Landmark Ed)*, 16: 368-92.

Davoudian, K., S. Bhattacharya, D. Thompson, and M. Thompson. 2023. 'Coupled Electrostatic and Hydrophobic Destabilisation of the Gelsolin-Actin Complex Enables Facile Detection of Ovarian Cancer Biomarker Lysophosphatidic Acid', *Biomolecules*, 13.

de Wet, J. R., K. V. Wood, M. DeLuca, D. R. Helinski, and S. Subramani. 1987. 'Firefly luciferase gene: structure and expression in mammalian cells', *Mol Cell Biol*, 7: 725-37.

Dvoretsky, P. M., K. A. Richards, C. Angel, L. Rabinowitz, M. H. Stoler, J. B. Beecham, and T. A. Bonfiglio. 1988. 'Distribution of disease at autopsy in 100 women with ovarian cancer', *Hum Pathol*, 19: 57-63.

Egoshi, S., K. Dodo, and M. Sodeoka. 2022. 'Deuterium Raman imaging for lipid analysis', *Curr Opin Chem Biol*, 70: 102181.

Elias, K. M., J. Guo, and R. C. Bast, Jr. 2018. 'Early Detection of Ovarian Cancer', *Hematol Oncol Clin North Am*, 32: 903-14.

Ellis, J. M., D. S. Paul, M. A. DePetrillo, B. P. Singh, D. E. Malarkey, and R. A. Coleman. 2012. 'Mice Deficient in Glycerol-3-Phosphate Acyltransferase-1 Have a Reduced Susceptibility to Liver Cancer', *Toxicologic Pathology*, 40: 513-21.

Fan, G., Y. Li, Y. Zong, X. Suo, Y. Jia, M. Gao, and X. Yang. 2023. 'GPAT3 regulates the synthesis of lipid intermediate LPA and exacerbates Kupffer cell inflammation mediated by the ERK signaling pathway', *Cell Death Dis*, 14: 208.

Fang, X., S. Yu, R. C. Bast, S. Liu, H. J. Xu, S. X. Hu, R. LaPushin, F. X. Claret, B. B. Aggarwal, Y. Lu, and G. B. Mills. 2004. 'Mechanisms for lysophosphatidic acid-induced cytokine production in ovarian cancer cells', *J Biol Chem*, 279: 9653-61.

Formolo, C. A., R. Williams, H. Gordish-Dressman, T. J. MacDonald, N. H. Lee, and Y. Hathout. 2011. 'Secretome signature of invasive glioblastoma multiforme', *J Proteome Res*, 10: 3149-59.

Franken, N. A., H. M. Rodermond, J. Stap, J. Haveman, and C. van Bree. 2006. 'Clonogenic assay of cells in vitro', *Nat Protoc*, 1: 2315-9.

Fratta, E., S. Coral, A. Covre, G. Parisi, F. Colizzi, R. Danielli, H. J. M. Nicolay, L. Sigalotti, and M. Maio. 2011. 'The biology of cancer testis antigens: Putative function, regulation and therapeutic potential', *Molecular Oncology*, 5: 164-82.

Friedl, P., and K. Wolf. 2003. 'Tumour-cell invasion and migration: diversity and escape mechanisms', *Nat Rev Cancer*, 3: 362-74.

Frisch, S. M., and H. Francis. 1994. 'Disruption of epithelial cell-matrix interactions induces apoptosis', *J Cell Biol*, 124: 619-26.

Gadducci, A., S. Cosio, A. Fanucchi, and A. R. Genazzani. 2001. 'Malnutrition and cachexia in ovarian cancer patients: pathophysiology and management', *Anticancer Res*, 21: 2941-7.

Garcia-Fabiani, M. B., M. A. Montanaro, E. Lacunza, E. R. Cattaneo, R. A. Coleman, M. Pellon-Maison, and M. R. Gonzalez-Baro. 2015. 'Methylation of the Gpat2 promoter regulates transient expression during mouse spermatogenesis', *Biochemical Journal*, 471: 211-20.

Geraldo, L. H. M., Tcls Spohr, R. F. D. Amaral, Accd Fonseca, C. Garcia, F. A. Mendes, C. Freitas, M. F. dosSantos, and F. R. S. Lima. 2021. 'Role of lysophosphatidic acid and its receptors in health and disease: novel therapeutic strategies', *Signal Transduct Target Ther*, 6: 45.

Gilks, C. B., J. Irving, M. Kobel, C. Lee, N. Singh, N. Wilkinson, and W. G. McCluggage. 2015. 'Incidental nonuterine high-grade serous carcinomas arise in the fallopian tube in most cases: further evidence for the tubal origin of high-grade serous carcinomas', *Am J Surg Pathol*, 39: 357-64.

Glazer, C. A., I. M. Smith, M. F. Ochs, S. Begum, W. Westra, S. S. Chang, W. Sun, S. Bhan, Z. Khan, S. Ahrendt, and J. A. Califano. 2009. 'Integrative discovery of epigenetically derepressed cancer testis antigens in NSCLC', *Plos One*, 4: e8189.

Goetzl, E. J., H. Dolezalova, Y. Kong, Y. L. Hu, R. B. Jaffe, K. N. Kalli, and C. A. Conover. 1999. 'Distinctive expression and functions of the type 4 endothelial differentiation gene-encoded G protein-coupled receptor for lysophosphatidic acid in ovarian cancer', *Cancer Research*, 59: 5370-75.

Goldie, J. H., and A. J. Coldman. 1979. 'A mathematic model for relating the drug sensitivity of tumors to their spontaneous mutation rate', *Cancer Treat Rep*, 63: 1727-33.

Goldman, A., M. Mullokandov, Y. Zaltsman, L. Regev, S. Levin-Zaidman, and A. Gross. 2024. 'MTCH2 cooperates with MFN2 and lysophosphatidic acid synthesis to sustain mitochondrial fusion', *EMBO Rep*, 25: 45-67.

Gonscharow, A. 2025. 'Mitochondrial lysophosphatidic acid generating enzymes glycerol-3-phosphate acyltransferase 1 and acylglycerol kinase are associated with ovarian cancer cell migration.', Eldorado Repository PhD thesis, TU Dortmund University.

Gonzalez-Martin, A., B. Pothuri, I. Vergote, R. DePont Christensen, W. Graybill, M. R. Mirza, C. McCormick, D. Lorusso, P. Hoskins, G. Freyer, K. Baumann, K. Jardon, A. Redondo, R. G. Moore, C. Vulsteke, R. E. O'Cearbhaill, B. Lund, F. Backes, P. Barretina-Ginesta, A. F. Haggerty, M. J. Rubio-Perez, M. S. Shahin, G. Mangili, W. H. Bradley, I. Bruchim, K. Sun, I. A. Malinowska, Y. Li, D. Gupta, B. J. Monk, and Prima Engot-Ov Gog- Investigators. 2019. 'Niraparib in Patients with Newly Diagnosed Advanced Ovarian Cancer', *N Engl J Med*, 381: 2391-402.

Gubbels, J. A., J. Belisle, M. Onda, C. Rancourt, M. Migneault, M. Ho, T. K. Bera, J. Connor, B. K. Sathyanarayana, B. Lee, I. Pastan, and M. S. Patankar. 2006. 'Mesothelin-MUC16 binding is a high affinity, N-glycan dependent interaction that facilitates peritoneal metastasis of ovarian tumors', *Mol Cancer*, 5: 50.

Gustin, C., M. Van Steenbrugge, and M. Raes. 2008. 'LPA modulates monocyte migration directly and via LPA-stimulated endothelial cells', *American Journal of Physiology-Cell Physiology*, 295: C905-C14.

Ha, J. H., J. D. Ward, R. Radhakrishnan, M. Jayaraman, Y. S. Song, and D. N. Dhanasekaran. 2016. 'Lysophosphatidic acid stimulates epithelial to mesenchymal transition marker Slug/Snail2 in ovarian cancer cells via Gai2, Src, and HIF1α signaling nexus', *Oncotarget*, 7: 37664-79.

Hakim, A., M. Moll, J. Brancale, J. Liu, J. A. Lasky-Su, E. K. Silverman, S. Vilarinho, Z. G. Jiang, Y. H. Pita-Juarez, I. S. Vlachos, X. Zhang, F. Aberg, N. H. Afdhal, B. D. Hobbs, and M. H. Cho. 2021. 'Genetic Variation in the Mitochondrial Glycerol-3-Phosphate Acyltransferase Is Associated With Liver Injury', *Hepatology*, 74: 3394-408.

Hanahan, D., and R. A. Weinberg. 2011. 'Hallmarks of cancer: the next generation', *Cell*, 144: 646-74.

Hashimoto, S., S. Mikami, H. Sugino, A. Yoshikawa, A. Hashimoto, Y. Onodera, S. Furukawa, H. Handa, T. Oikawa, Y. Okada, M. Oya, and H. Sabe. 2016. 'Lysophosphatidic acid activates Arf6 to promote the mesenchymal malignancy of renal cancer', *Nature Communications*, 7: 11.

Haverty, P. M., L. S. Hon, J. S. Kaminker, J. Chant, and Z. Zhang. 2009. 'High-resolution analysis of copy number alterations and associated expression changes in ovarian tumors', *BMC Med Genomics*, 2: 21.

Hayashi, K., M. Takahashi, W. Nishida, K. Yoshida, Y. Ohkawa, A. Kitabatake, J. Aoki, H. Arai, and K. Sobue. 2001. 'Phenotypic modulation of vascular smooth muscle cells induced by unsaturated lysophosphatidic acids', *Circulation Research*, 89: 251-58.

Horwitz, R., and D. Webb. 2003. 'Cell migration', *Curr Biol*, 13: R756-9.

Hu, A., Y. Liu, H. Zhang, T. Wang, J. Zhang, W. Cheng, T. Yu, Y. Duan, J. Feng, Z. Chen, Y. Ding, Y. Li, M. Li, Z. Rong, Y. Shang, S. S. Shakila, Y. Zou, F. Ma, and B. Guo. 2023. 'BPIFB1 promotes metastasis of hormone receptor-positive breast cancer via inducing macrophage M2-like polarization', *Cancer Sci*, 114: 4157-71.

Hu, M., Y. Lan, A. Lu, X. Ma, and L. Zhang. 2019. 'Glycan-based biomarkers for diagnosis of cancers and other diseases: Past, present, and future', *Prog Mol Biol Transl Sci*, 162: 1-24.

Hu, Y. L., M. K. Tee, E. J. Goetzl, N. Auersperg, G. B. Mills, N. Ferrara, and R. B. Jaffe. 2001. 'Lysophosphatidic acid induction of vascular endothelial growth factor expression in human ovarian cancer cells', *J Natl Cancer Inst*, 93: 762-8.

Huber, M. A., N. Kraut, and H. Beug. 2005. 'Molecular requirements for epithelial-mesenchymal transition during tumor progression', *Curr Opin Cell Biol*, 17: 548-58.

Irifune, H., Y. Kochi, T. Miyamoto, T. Sakoda, K. Kato, Y. Kunisaki, K. Akashi, and Y. Kikushige. 2023. 'GPAM mediated lysophosphatidic acid synthesis regulates mitochondrial dynamics in acute myeloid leukemia', *Cancer Sci*, 114: 3247-58.

Izdebska, M., W. Zielinska, D. Grzanka, and M. Gagat. 2018. 'The Role of Actin Dynamics and Actin-Binding Proteins Expression in Epithelial-to-Mesenchymal Transition and Its Association with Cancer Progression and Evaluation of Possible Therapeutic Targets', *Biomed Res Int*, 2018: 4578373.

Jamialahmadi, O., R. M. Mancina, E. Ciociola, F. Tavaglione, P. K. Luukkonen, G. Baselli, F. Malvestiti, D. Thuillier, V. Raverdy, V. Mannisto, R. M. Pipitone, G. Pennisi, D. Prati, R. Spagnuolo, S. Petta, J. Pihlajamaki, F. Pattou, H. Yki-Jarvinen, L. Valenti, and S. Romeo. 2021. 'Exome-Wide Association Study on Alanine Aminotransferase Identifies Sequence Variants in the GPAM and APOE Associated With Fatty Liver Disease', *Gastroenterology*, 160: 1634-46 e7.

Jiang, S., Q. Zhang, Y. Su, and L. Pan. 2018. 'Network-Based Differential Analysis to Identify Molecular Features of Tumorigenesis for Esophageal Squamous Carcinoma', *Molecules*, 23.

Jones, R. R., D. C. Hooper, L. Zhang, D. Wolverson, and V. K. Valev. 2019. 'Raman Techniques: Fundamentals and Frontiers', *Nanoscale Res Lett*, 14: 231.

Kalluri, R., and R. A. Weinberg. 2009. 'The basics of epithelial-mesenchymal transition', *J Clin Invest*, 119: 1420-8.

Kaoutari, A. E., N. A. Fraunhoffer, O. Hoare, C. Teyssedou, P. Soubeyran, O. Gayet, J. Roques, G. Lomberk, R. Urrutia, N. Dusetti, and J. Iovanna. 2021. 'Metabolomic profiling of pancreatic adenocarcinoma reveals key features driving clinical outcome and drug resistance', *EBioMedicine*, 66: 103332.

Karasawa, K., K. Tanigawa, A. Harada, and A. Yamashita. 2019. 'Transcriptional Regulation of Acyl-CoA:Glycerol-sn-3-Phosphate Acyltransferases', *Int J Mol Sci*, 20.

Kato, K., K. Yoshikawa, E. Tanabe, M. Kitayoshi, R. Fukui, N. Fukushima, and T. Tsujiuchi. 2012. 'Opposite roles of LPA1 and LPA3 on cell motile and invasive activities of pancreatic cancer cells', *Tumor Biology*, 33: 1739-44.

Kienesberger, P. C., A. Lass, K. Preiss-Landl, H. Wolinski, S. D. Kohlwein, R. Zimmermann, and R. Zechner. 2008. 'Identification of an insulin-regulated lysophospholipase with homology to neuropathy target esterase', *J Biol Chem*, 283: 5908-17.

Kim, J. K., J. J. Fillmore, Y. Chen, C. Yu, I. K. Moore, M. Pypaert, E. P. Lutz, Y. Kako, W. Velez-Carrasco, I. J. Goldberg, J. L. Breslow, and G. I. Shulman. 2001. 'Tissue-specific overexpression of lipoprotein lipase causes tissue-specific insulin resistance', *Proc Natl Acad Sci U S A*, 98: 7522-7.

Kim, S., B. Kim, and Y. S. Song. 2016. 'Ascites modulates cancer cell behavior, contributing to tumor heterogeneity in ovarian cancer', *Cancer Sci*, 107: 1173-8.

Kindelberger, D. W., Y. Lee, A. Miron, M. S. Hirsch, C. Feltmate, F. Medeiros, M. J. Callahan, E. O. Garner, R. W. Gordon, C. Birch, R. S. Berkowitz, M. G. Muto, and C. P. Crum. 2007. 'Intraepithelial carcinoma of the fimbria and pelvic serous carcinoma: Evidence for a causal relationship', *Am J Surg Pathol*, 31: 161-9.

Kuhajda, F. P., S. Aja, Y. Tu, W. F. Han, S. M. Medghalchi, R. El Meskini, L. E. Landree, J. M. Peterson, K. Daniels, K. Wong, E. A. Wydysh, C. A. Townsend, and G. V. Ronnett. 2011. 'Pharmacological glycerol-3-phosphate acyltransferase inhibition decreases food intake and adiposity and increases insulin sensitivity in diet-induced obesity', *Am J Physiol Regul Integr Comp Physiol*, 301: R116-30.

Kuo, K. T., B. Guan, Y. Feng, T. L. Mao, X. Chen, N. Jinawath, Y. Wang, R. J. Kurman, M. Shih Ie, and T. L. Wang. 2009. 'Analysis of DNA copy number alterations in ovarian serous tumors identifies new molecular genetic changes in low-grade and high-grade carcinomas', *Cancer Res*, 69: 4036-42.

Labbé, K., S. Mookerjee, M. Le Vasseur, E. Gibbs, C. Lerner, and J. Nunnari. 2021. 'The modified mitochondrial outer membrane carrier MTCH2 links mitochondrial fusion to lipogenesis', *J Cell Biol*, 220.

Labidi-Galy, S. I., E. Papp, D. Hallberg, N. Niknafs, V. Adleff, M. Noe, R. Bhattacharya, M. Novak, S. Jones, J. Phallen, C. A. Hruban, M. S. Hirsch, D. I. Lin, L. Schwartz, C. L. Maire, J. C. Tille, M. Bowden, A. Ayhan, L. D. Wood, R. B. Scharpf, R. Kurman, T. L. Wang, I. M. Shih, R. Karchin, R. Drapkin, and V. E. Velculescu. 2017. 'High grade serous ovarian carcinomas originate in the fallopian tube', *Nat Commun*, 8: 1093.

Laemmli, U. K. 1970. 'Cleavage of structural proteins during the assembly of the head of bacteriophage T4', *Nature*, 227: 680-5.

Lee, J. H., D. Kim, Y. S. Oh, and H. S. Jun. 2019. 'Lysophosphatidic Acid Signaling in Diabetic Nephropathy', *Int J Mol Sci*, 20.

Lengyel, E. 2010. 'Ovarian cancer development and metastasis', *Am J Pathol*, 177: 1053-64.

Lewin, T. M., H. de Jong, N. J. M. Schwerbrock, L. E. Hammond, S. M. Watkins, T. P. Combs, and R. A. Coleman. 2008. 'Mice deficient in mitochondrial glycerol-3-phosphate acyltransferase-1 have diminished myocardial triacylglycerol accumulation during lipogenic diet and altered phospholipid fatty acid composition', *Biochimica Et Biophysica Acta-Molecular and Cell Biology of Lipids*, 1781: 352-58.

Li, J., P. Xu, L. Wang, M. Feng, D. Chen, X. Yu, and Y. Lu. 2020. 'Molecular biology of BPIFB1 and its advances in disease', *Ann Transl Med*, 8: 651.

Li, Nian-Sheng, Li Chen, Zuo-Xiu Xiao, Yu-Qi Yang, and Ke-Long Ai. 2020. 'Progress in Detection of Biomarker of Ovarian Cancer: Lysophosphatidic Acid', *Chinese Journal of Analytical Chemistry*, 48: 1597-606.

Li, T. T., M. Alemayehu, A. I. Aziziyeh, C. Pape, M. Pampillo, L. M. Postovit, G. B. Mills, A. V. Babwah, and M. Bhattacharya. 2009. 'β-Arrestin/Ral Signaling Regulates Lysophosphatidic Acid-Mediated Migration and Invasion of Human Breast Tumor Cells', *Molecular Cancer Research*, 7: 1064-77.

Livak, K. J., and T. D. Schmittgen. 2001. 'Analysis of relative gene expression data using real-time quantitative PCR and the 2(-Delta Delta C(T)) Method', *Methods*, 25: 402-8.

Ludwig, C., L. Gillet, G. Rosenberger, S. Amon, B. C. Collins, and R. Aebersold. 2018. 'Data-independent acquisition-based SWATH-MS for quantitative proteomics: a tutorial', *Mol Syst Biol*, 14: e8126.

Lynch, H. T., M. J. Casey, C. L. Snyder, C. Bewtra, J. F. Lynch, M. Butts, and A. K. Godwin. 2009. 'Hereditary ovarian carcinoma: heterogeneity, molecular genetics, pathology, and management', *Mol Oncol*, 3: 97-137.

Malander, S., M. Ridderheim, A. Masback, N. Loman, U. Kristoffersson, H. Olsson, M. Nilbert, and A. Borg. 2004. 'One in 10 ovarian cancer patients carry germ line BRCA1 or BRCA2 mutations: results of a prospective study in Southern Sweden', *Eur J Cancer*, 40: 422-8.

Marchan, Rosemarie, Bettina Büttner, Jörg Lambert, Karolina Edlund, Iris Glaeser, Meinolf Blaszkewicz, Gregor Leonhardt, Lisa Marienhoff, Darius Kaszta, Moritz Anft, Carsten Watzl, Katrin Madjar, Marianna Grinberg, Eugen Rempel, Roland Hergenröder, Silvia Selinski, Jörg Rahnenführer, Michaela S. Lesjak, Joanna D. Stewart, Cristina Cadenas, and Jan G. Hengstler. 2017. 'Glycerol-3-phosphate Acyltransferase 1 Promotes Tumor Cell Migration and Poor Survival in Ovarian Carcinoma', *Cancer Research*, 77: 4589-601.

Matulonis, U. A., A. K. Sood, L. Fallowfield, B. E. Howitt, J. Sehouli, and B. Y. Karlan. 2016. 'Ovarian cancer', *Nat Rev Dis Primers*, 2: 16061.

McCluggage, W. G. 2011. 'Morphological subtypes of ovarian carcinoma: a review with emphasis on new developments and pathogenesis', *Pathology*, 43: 420-32.

McFadden, J. W., S. Aja, Q. Li, V. V. Bandaru, E. K. Kim, N. J. Haughey, F. P. Kuhajda, and G. V. Ronnett. 2014. 'Increasing fatty acid oxidation remodels the hypothalamic neurometabolome to mitigate stress and inflammation', *Plos One*, 9: e115642.

McIntyre, T. M., A. V. Pontsler, A. R. Silva, A. St Hilaire, Y. Xu, J. C. Hinshaw, G. A. Zimmerman, K. Hama, J. Aoki, H. Arai, and G. D. Prestwich. 2003. 'Identification of an intracellular receptor for lysophosphatidic acid (LPA): LPA is a transcellular PPARgamma agonist', *Proc Natl Acad Sci U S A*, 100: 131-6.

Meerschaert, K., V. De Corte, Y. De Ville, J. Vandekerckhove, and J. Gettemans. 1998. 'Gelsolin and functionally similar actin-binding proteins are regulated by lysophosphatidic acid', *Embo Journal*, 17: 5923-32.

Meng, C., Y. Sun, and G. Liu. 2023. 'Establishment of a prognostic model for ovarian cancer based on mitochondrial metabolism-related genes', *Front Oncol*, 13: 1144430.

Moolenaar, W. H., L. A. van Meeteren, and B. N. Giepmans. 2004. 'The ins and outs of lysophosphatidic acid signaling', *Bioessays*, 26: 870-81.

Moore, K., N. Colombo, G. Scambia, B. G. Kim, A. Oaknin, M. Friedlander, A. Lisyanskaya, A. Floquet, A. Leary, G. S. Sonke, C. Gourley, S. Banerjee, A. Oza, A. Gonzalez-Martin, C. Aghajanian, W. Bradley, C. Mathews, J. Liu, E. S. Lowe, R. Bloomfield, and P. DiSilvestro. 2018. 'Maintenance Olaparib in Patients with Newly Diagnosed Advanced Ovarian Cancer', *N Engl J Med*, 379: 2495-505.

Moser, T. L., S. V. Pizzo, L. M. Bafetti, D. A. Fishman, and M. S. Stack. 1996. 'Evidence for preferential adhesion of ovarian epithelial carcinoma cells to type I collagen mediated by the alpha2beta1 integrin', *Int J Cancer*, 67: 695-701.

Mukherjee, A., Y. B. Ma, F. Yuan, Y. L. Gong, Z. Y. Fang, E. M. Mohamed, E. Berrios, H. J. Shao, and X. J. Fang. 2015. 'Lysophosphatidic Acid Up-Regulates Hexokinase II and Glycolysis to Promote Proliferation of Ovarian Cancer Cells', *Neoplasia*, 17: 723-34.

Nagao, S., K. Fujiwara, K. Yamamoto, H. Tanabe, A. Okamoto, K. Takehara, M. Saito, H. Fujiwara, D. S. P. Tan, S. Yamaguchi, S. Adachi, A. Kikuchi, T. Hirasawa, T. Yokoi, T. Nagai, T. Sato, S. Kamiura, A. Fujishita, W. W. Loong, K. Chan, P. Syks, A. Olawaye, S. Y. Ryu, H. Shigeta, E. Kondo, Y. Yokoyama, T. Matsumoto, K. Hasegawa, and T. Enomoto. 2023. 'Intraperitoneal Carboplatin for Ovarian Cancer - A Phase 2/3 Trial', *NEJM Evid*, 2: EVIDoa2200225.

Nagle, C. A., J. An, M. Shiota, T. P. Torres, G. W. Cline, Z. X. Liu, S. L. Wang, R. L. Catlin, G. I. Shulman, C. B. Newgard, and R. A. Coleman. 2007. 'Hepatic overexpression of glycerol-sn-3-phosphate acyltransferase 1 in rats causes insulin resistance', *Journal of Biological Chemistry*, 282: 14807-15.

Nasser, M. W., Z. Qamri, Y. S. Deol, J. Ravi, C. A. Powell, P. Trikha, R. A. Schwendener, X. F. Bai, K. Shilo, X. Zou, G. Leone, R. Wolf, S. H. Yuspa, and R. K. Ganju. 2012. 'S100A7 enhances mammary tumorigenesis through upregulation of inflammatory pathways', *Cancer Res*, 72: 604-15.

Ohba, Yohsuke, Takeshi Sakuragi, Eriko Kage-Nakadai, Naoko H Tomioka, Nozomu Kono, Rieko Imae, Asuka Inoue, Junken Aoki, Naotada Ishihara, Takao Inoue, Shohei Mitani, and Hiroyuki Arai. 2013. 'Mitochondria-type GPAT is required for mitochondrial fusion', *The EMBO Journal*, 32: 1265-79.

Ohshima, N., T. Kudo, Y. Yamashita, S. Mariggio, M. Araki, A. Honda, T. Nagano, C. Isaji, N. Kato, D. Corda, T. Izumi, and N. Yanaka. 2015. 'New members of the mammalian glycerophosphodiester phosphodiesterase family: GDE4 and GDE7 produce lysophosphatidic acid by lysophospholipase D activity', *J Biol Chem*, 290: 4260-71.

Pagès, C., M. F. Simon, P. Valet, and J. S. Saulnier-Blache. 2001. 'Lysophosphatidic acid synthesis and release', *Prostaglandins & Other Lipid Mediators*, 64: 1-10.

Parazzini, F., E. Negri, C. La Vecchia, C. Restelli, and S. Franceschi. 1992. 'Family history of reproductive cancers and ovarian cancer risk: an Italian case-control study', *Am J Epidemiol*, 135: 35-40.

Pellon-Maison, M., M. A. Montanaro, E. Lacunza, M. B. Garcia-Fabiani, M. C. Soler-Gerino, E. R. Cattaneo, I. Y. Quiroga, M. C. Abba, R. A. Coleman, and M. R. Gonzalez-Baro. 2014. 'Glycerol-3-Phosphate Acyltranferase-2 Behaves as a Cancer Testis Gene and Promotes Growth and Tumorigenicity of the Breast Cancer MDA-MB-231 Cell Line', *Plos One*, 9: 11.

Pribyl, M., Z. Hodny, and I. Kubikova. 2021. 'Suprabasin-A Review', *Genes (Basel)*, 12.

Prowse, A. H., S. Manek, R. Varma, J. Liu, A. K. Godwin, E. R. Maher, I. P. Tomlinson, and S. H. Kennedy. 2006. 'Molecular genetic evidence that endometriosis is a precursor of ovarian cancer', *Int J Cancer*, 119: 556-62.

Raman, C. V., and K. S. Krishnan. 1928. 'A New Type of Secondary Radiation', *Nature*, 121: 501-02.

Reed, E., C. S. Zerbe, O. W. Brawley, A. Bicher, and S. M. Steinberg. 2000. 'Analysis of autopsy evaluations of ovarian cancer patients treated at the National Cancer Institute, 1972-1988', *Am J Clin Oncol*, 23: 107-16.

Reid, B. M., J. B. Permuth, and T. A. Sellers. 2017. 'Epidemiology of ovarian cancer: a review', *Cancer Biol Med*, 14: 9-32.

Ren, J., Y. J. Xiao, L. S. Singh, X. Zhao, Z. Zhao, L. Feng, T. M. Rose, G. D. Prestwich, and Y. Xu. 2006. 'Lysophosphatidic acid is constitutively produced by human peritoneal mesothelial cells and enhances adhesion, migration, and invasion of ovarian cancer cells', *Cancer Res*, 66: 3006-14.

Rinella, M. E., J. V. Lazarus, V. Ratziu, S. M. Francque, A. J. Sanyal, F. Kanwal, D. Romero, M. F. Abdelmalek, Q. M. Anstee, J. P. Arab, M. Arrese, R. Bataller, U. Beuers, J. Boursier, E. Bugianesi, C. D. Byrne, G. E. Castro Narro, A. Chowdhury, H. Cortez-Pinto, D. R. Cryer, K. Cusi, M. El-Kassas, S. Klein, W. Eskridge, J. Fan, S. Gawrieh, C. D. Guy, S. A. Harrison, S. U. Kim, B. G. Koot, M. Korenjak, K. V. Kowdley, F. Lacaille, R. Loomba, R. Mitchell-Thain, T. R. Morgan, E. E. Powell, M. Roden, M. Romero-Gomez, M. Silva, S. P. Singh, S. C. Sookoian, C. W. Spearman, D. Tiniakos, L. Valenti, M. B. Vos, V. W. Wong, S. Xanthakos, Y. Yilmaz, Z. Younossi, A. Hobbs, M. Villota-Rivas, P. N. Newsome, and Nafld Nomenclature consensus group. 2023. 'A multisociety Delphi consensus statement on new fatty liver disease nomenclature', *Hepatology*, 78: 1966-86.

Rorth, P. 2009. 'Collective cell migration', *Annu Rev Cell Dev Biol*, 25: 407-29.

Sauter, D. R., C. E. Sorensen, M. Rapedius, A. Bruggemann, and I. Novak. 2016. 'pH-sensitive K(+) channel TREK-1 is a novel target in pancreatic cancer', *Biochim Biophys Acta*, 1862: 1994-2003.

Schwartz, B. M., G. Hong, B. H. Morrison, W. Wu, L. M. Baudhuin, Y. J. Xiao, S. C. Mok, and Y. Xu. 2001. 'Lysophospholipids increase interleukin-8 expression in ovarian cancer cells', *Gynecol Oncol*, 81: 291-300.

Shan, D. D., J. L. Li, L. Y. Wu, D. M. Li, J. Hurov, J. F. Tobin, R. E. Gimeno, and J. S. Cao. 2010. 'GPAT3 and GPAT4 are regulated by insulin-stimulated phosphorylation and play distinct roles in adipogenesis', *Journal of Lipid Research*, 51: 1971-81.

Shida, D., J. Kitayama, H. Yamaguchi, K. Hama, J. Aoki, H. Arai, H. Yamashita, K. Mori, A. Sako, T. Konishi, T. Watanabe, T. Sakai, R. Suzuki, H. Ohta, Y. Takuwa, and H. Nagawa. 2004. 'Dual mode regulation of migration by lysophosphatidic acid in human gastric cancer cells', *Experimental Cell Research*, 301: 168-78.

Shih Ie, M., and R. J. Kurman. 2004. 'Ovarian tumorigenesis: a proposed model based on morphological and molecular genetic analysis', *Am J Pathol*, 164: 1511-8.

Shin, O. S., T. Uddin, R. Citorik, J. P. Wang, P. Della Pelle, R. L. Kradin, C. D. Bingle, L. Bingle, A. Camilli, T. R. Bhuiyan, T. Shirin, E. T. Ryan, S. B. Calderwood, R. W. Finberg, F. Qadri, R. C. Larocque, and J. B. Harris. 2011. 'LPLUNC1 modulates innate immune responses to Vibrio cholerae', *J Infect Dis*, 204: 1349-57.

Si, J. G., Y. Y. Su, Y. F. Wang, Y. L. Yan, and Y. L. Tang. 2015. 'Expressions of lysophosphatidic acid receptors in the development of human ovarian carcinoma', *International Journal of Clinical and Experimental Medicine*, 8: 17880-90.

Simic, P., W. Kim, W. Zhou, K. A. Pierce, W. Chang, D. B. Sykes, N. B. Aziz, S. Elmariah, D. Ngo, P. D. Pajevic, N. Govea, B. R. Kestenbaum, I. H. de Boer, Z. Cheng, M. Christov, J. Chun, D. E. Leaf, S. S. Waikar, A. M. Tager, R. E. Gerszten, R. I. Thadhani, C. B. Clish, H. Juppner, M. N. Wein, and E. P. Rhee. 2020. 'Glycerol-3-phosphate is an FGF23 regulator derived from the injured kidney', *J Clin Invest*, 130: 1513-26.

Smith, K. R., W. Wang, M. R. Miller, M. Boucher, J. E. Reynold, N. A. Daurio, D. Li, D. Hirenallur-Shanthappa, Y. Ahn, D. A. Beebe, K. L. Kelly, T. T. Ross, K. K. Bence, and M. Wan. 2024. 'GPAT1 Deficiency in Mice Modulates NASH Progression in a Model-Dependent Manner', *Cell Mol Gastroenterol Hepatol*, 17: 279-91.

Smith, P. K., R. I. Krohn, G. T. Hermanson, A. K. Mallia, F. H. Gartner, M. D. Provenzano, E. K. Fujimoto, N. M. Goeke, B. J. Olson, and D. C. Klenk. 1985. 'Measurement of protein using bicinchoninic acid', *Anal Biochem*, 150: 76-85.

So, J., J. Navari, F. Q. Wang, and D. A. Fishman. 2004. 'Lysophosphatidic acid enhances epithelial ovarian carcinoma invasion through the increased expression of interleukin-8', *Gynecol Oncol*, 95: 314-22.

Sood, A., D. Mishra, O. P. Kharbanda, S. S. Chauhan, S. D. Gupta, S. S. V. Deo, R. Yadav, R. Ralhan, R. Kumawat, and H. Kaur. 2022. 'Role of S100 A7 as a diagnostic biomarker in oral potentially malignant disorders and oral cancer', *J Oral Maxillofac Pathol*, 26: 166-72.

Stapleton, C. M., D. G. Mashek, S. Wang, C. A. Nagle, G. W. Cline, P. Thuillier, L. M. Leesnitzer, L. O. Li, J. B. Stimmel, G. I. Shulman, and R. A. Coleman. 2011. 'Lysophosphatidic acid activates peroxisome proliferator activated receptor-gamma in CHO cells that over-express glycerol 3-phosphate acyltransferase-1', *Plos One*, 6: e18932.

Stewart, S. A., D. M. Dykxhoorn, D. Palliser, H. Mizuno, E. Y. Yu, D. S. An, D. M. Sabatini, I. S. Chen, W. C. Hahn, P. A. Sharp, R. A. Weinberg, and C. D. Novina. 2003. 'Lentivirus-delivered stable gene silencing by RNAi in primary cells', *Rna*, 9: 493-501.

Stoddard, N. C., and J. Chun. 2015. 'Promising Pharmacological Directions in the World of Lysophosphatidic Acid Signaling', *Biomolecules & Therapeutics*, 23: 1-11.

Stratton, J. F., P. Pharoah, S. K. Smith, D. Easton, and B. A. Ponder. 1998. 'A systematic review and meta-analysis of family history and risk of ovarian cancer', *Br J Obstet Gynaecol*, 105: 493-9.

Stribbling, S. M., and A. J. Ryan. 2022. 'The cell-line-derived subcutaneous tumor model in preclinical cancer research', *Nat Protoc*, 17: 2108-28.

Strobel, T., L. Swanson, and S. A. Cannistra. 1997. 'In vivo inhibition of CD44 limits intra-abdominal spread of a human ovarian cancer xenograft in nude mice: a novel role for CD44 in the process of peritoneal implantation', *Cancer Res*, 57: 1228-32.

Sukumaran, S., R. I. Barnes, A. Garg, and A. K. Agarwal. 2009. 'Functional characterization of the human 1-acylglycerol-3-phosphate-O-acyltransferase isoform 10/glycerol-3-phosphate acyltransferase isoform 3', *Journal of Molecular Endocrinology*, 42: 469-78.

Taddei, M. L., E. Giannoni, T. Fiaschi, and P. Chiarugi. 2012. 'Anoikis: an emerging hallmark in health and diseases', *J Pathol*, 226: 380-93.

Takahashi, K., K. Fukushima, Y. Onishi, K. Inui, Y. Node, N. Fukushima, K. Honoki, and T. Tsujiuchi. 2017. 'Lysophosphatidic acid (LPA) signaling via LPA4 and LPA6 negatively regulates cell motile activities of colon cancer cells', *Biochemical and Biophysical Research Communications*, 483: 652-57.

Takeuchi, K., and K. Reue. 2009. 'Biochemistry, physiology, and genetics of GPAT, AGPAT, and lipin enzymes in triglyceride synthesis', *American Journal of Physiology-Endocrinology and Metabolism*, 296: E1195-E209.

Thompson, F. J., and M. A. Clark. 1994. 'Purification of a lysophosphatidic acid-hydrolysing lysophospholipase from rat brain', *Biochemical Journal*, 300: 457-61.

Tokumura, A. 2004. 'Metabolic pathways and physiological and pathological significances of lysolipid phosphate mediators', *Journal of Cellular Biochemistry*, 92: 869-81.

Tomar, A., S. P. George, S. Mathew, and S. Khurana. 2009. 'Differential effects of lysophosphatidic acid and phosphatidylinositol 4,5-bisphosphate on actin dynamics by direct association with the actin-binding protein villin', *J Biol Chem*, 284: 35278-82.

Trimbos, J. B., I. Vergote, G. Bolis, J. B. Vermorken, C. Mangioni, C. Madronal, M. Franchi, S. Tateo, G. Zanetta, G. Scarfone, L. Giurgea, P. Timmers, C. Coens, S. Pecorelli, Eortc-Action collaborators. European Organisation for Research, and Neoplasm Treatment of Cancer-Adjuvant ChemoTherapy in Ovarian. 2003. 'Impact of adjuvant chemotherapy and surgical staging in early-stage ovarian carcinoma: European Organisation for Research and Treatment of Cancer-Adjuvant ChemoTherapy in Ovarian Neoplasm trial', *J Natl Cancer Inst*, 95: 113-25.

Tserendavga, B., N. Ohshima, C. Fujita, K. Yuzawa, M. Ohshima, N. Yanaka, Y. A. Minamishima, and T. Izumi. 2022. 'Characterization of recombinant murine GDE4 and GDE7, enzymes producing lysophosphatidic acid and/or cyclic phosphatidic acid', *J Biochem*, 170: 713-27.

Valdés-Rives, S. A., and A. González-Arenas. 2017. 'Autotaxin-Lysophosphatidic Acid: From Inflammation to Cancer Development', *Mediators of Inflammation*, 2017: 15.

Vancura, A., and D. Haldar. 1994. 'Purification and characterization of glycerophosphate acyltransferase from rat liver mitochondria', *J Biol Chem*, 269: 27209-15.

Vanderbend, R. L., J. Dewidt, E. J. Vancorven, W. H. Moolenaar, and W. J. Vanblitterswijk. 1992. 'Metabolic conversion of the biologically active phospholipid, lysophosphatidic acid, in fibroblasts', *Biochimica Et Biophysica Acta*, 1125: 110-12.

Veatch, A. L., L. F. Carson, and S. Ramakrishnan. 1994. 'Differential expression of the cell-cell adhesion molecule E-cadherin in ascites and solid human ovarian tumor cells', *Int J Cancer*, 58: 393-9.

Wang, S., D. P. Lee, N. Gong, N. M. J. Schwerbrock, D. G. Mashek, M. R. Gonzalez-Baró, C. Stapleton, L. O. Li, T. M. Lewin, and R. A. Coleman. 2007. 'Cloning and functional characterization of a novel mitochondrial N-ethylmaleimide-sensitive glycerol-3-phosphate acyltransferase (GPAT2)', *Archives of Biochemistry and Biophysics*, 465: 347-58.

Wang, Y., C. Xu, X. Yang, X. Liu, Z. Guo, X. Lin, L. Li, and Z. Huang. 2024. 'Glycerol-3-phosphate acyltransferase 3-mediated lipid droplets accumulation confers chemoresistance of colorectal cancer', *MedComm (2020)*, 5: e486.

Wei, F., L. Tang, Y. He, Y. Wu, L. Shi, F. Xiong, Z. Gong, C. Guo, X. Li, Q. Liao, W. Zhang, Q. Ni, J. Luo, X. Li, Y. Li, C. Peng, X. Chen, G. Li, W. Xiong, and Z. Zeng. 2018. 'BPIFB1 (LPLUNC1) inhibits radioresistance in nasopharyngeal carcinoma by inhibiting VTN expression', *Cell Death Dis*, 9: 432.

Wendel, A. A., T. M. Lewin, and R. A. Coleman. 2009. 'Glycerol-3-phosphate acyltransferases: Rate limiting enzymes of triacylglycerol biosynthesis', *Biochimica Et Biophysica Acta-Molecular and Cell Biology of Lipids*, 1791: 501-06.

Wilfling, F., H. J. Wang, J. T. Haas, N. Krahmer, T. J. Gould, A. Uchida, J. X. Cheng, M. Graham, R. Christiano, F. Fröhlich, X. R. Liu, K. K. Buhman, R. A. Coleman, J. Bewersdorf, R. V. Farese, and T. C. Walther. 2013. 'Triacylglycerol Synthesis Enzymes Mediate Lipid Droplet Growth by Relocalizing from the ER to Lipid Droplets', *Developmental Cell*, 24: 384-99.

Wydysh, E. A., S. M. Medghalchi, A. Vadlamudi, and C. A. Townsend. 2009. 'Design and synthesis of small molecule glycerol 3-phosphate acyltransferase inhibitors', *J Med Chem*, 52: 3317-27.

Wydysh, E. A., A. Vadlamudi, S. M. Medghalchi, and C. A. Townsend. 2010. 'Design, synthesis, and biological evaluation of conformationally constrained glycerol 3-phosphate acyltransferase inhibitors', *Bioorg Med Chem*, 18: 6470-9.

Xie, Yuhuan, Terra C. Gibbs, and Kathryn E. Meier. 2002. 'Lysophosphatidic acid as an autocrine and paracrine mediator', *Biochimica et Biophysica Acta (BBA) - Molecular and Cell Biology of Lipids*, 1582: 270-81.

Xu, Yan, Zhongzhou Shen, Donald W. Wiper, Minzhi Wu, Richard E. Morton, Paul Elson, Alexander W. Kennedy, Jerome Belinson, Maurie Markman, and Graham Casey. 1998. 'Lysophosphatidic Acid as a Potential Biomarker for Ovarian and Other Gynecologic Cancers', *JAMA*, 280: 719-23.

Yamaguchi, H., and J. Condeelis. 2007. 'Regulation of the actin cytoskeleton in cancer cell migration and invasion', *Biochim Biophys Acta*, 1773: 642-52.

Yamashita, A., Y. Hayashi, N. Matsumoto, Y. Nemoto-Sasaki, S. Oka, T. Tanikawa, and T. Sugiura. 2014. 'Glycerophosphate/Acylglycerophosphate acyltransferases', *Biology (Basel)*, 3: 801-30.

Yamashita, A., Y. Hayashi, Y. Nemoto-Sasaki, M. Ito, S. Oka, T. Tanikawa, K. Waku, and T. Sugiura. 2014. 'Acyltransferases and transacylases that determine the fatty acid composition of glycerolipids and the metabolism of bioactive lipid mediators in mammalian cells and model organisms', *Prog Lipid Res*, 53: 18-81.

Yao, C. H., J. S. Park, K. Kurmi, S. H. Hu, G. Notarangelo, J. Crowley, H. Jacobson, S. Hui, A. H. Sharpe, and M. C. Haigis. 2023. 'Uncoupled glycerol-3-phosphate shuttle in kidney cancer reveals that cytosolic GPD is essential to support lipid synthesis', *Mol Cell*, 83: 1340-49 e7.

Ying, F., J. Guo, X. Gao, L. Huang, L. Gao, J. Cai, and Z. Wang. 2023. 'Establishment of highly metastatic ovarian cancer model with omental tropism via in vivo selection', *iScience*, 26: 106719.

Younis, S., and S. Rashid. 2017. 'Alpha conotoxin-BuIA globular isomer is a competitive antagonist for oleoyl-L-alpha-lysophosphatidic acid binding to LPAR6; A molecular dynamics study', *Plos One*, 12: 18.

Yu, J., K. Loh, Z. Y. Song, H. Q. Yang, Y. Zhang, and S. Lin. 2018. 'Update on glycerol-3-phosphate acyltransferases: the roles in the development of insulin resistance', *Nutr Diabetes*, 8: 34.

Yu, S. X., M. M. Murph, Y. L. Lu, S. Y. Liu, H. S. Hall, J. S. Liu, C. Stephens, X. J. Fang, and G. B. Mills. 2008. 'Lysophosphatidic Acid Receptors Determine Tumorigenicity and Aggressiveness of Ovarian Cancer Cells', *Jnci-Journal of the National Cancer Institute*, 100: 1630-42.

Yung, Y. C., N. C. Stoddard, and J. Chun. 2014. 'LPA receptor signaling: pharmacology, physiology, and pathophysiology', *J Lipid Res*, 55: 1192-214.

Zanetta, G., S. Chiari, S. Rota, G. Bratina, A. Maneo, V. Torri, and C. Mangioni. 1997. 'Conservative surgery for stage I ovarian carcinoma in women of childbearing age', *Br J Obstet Gynaecol*, 104: 1030-5.

Zhang, C. B., D. E. Cooper, T. J. Grevengoed, L. O. Li, E. L. Klett, J. M. Eaton, T. E. Harris, and R. A. Coleman. 2014. 'Glycerol-3-phosphate acyltransferase-4-deficient mice are protected from diet-induced insulin resistance by the enhanced association of mTOR and rictor', *American Journal of Physiology-Endocrinology and Metabolism*, 307: E305-E15.

Zhang, C. B., A. A. Wendel, M. R. Keogh, T. E. Harris, J. Chen, and R. A. Coleman. 2012. 'Glycerolipid signals alter mTOR complex 2 (mTORC2) to diminish insulin signaling', *Proceedings of the National Academy of Sciences of the United States of America*, 109: 1667-72.

Zhang, C., M. Steadman, H. P. Santos, Jr., S. R. Shaikh, and R. M. Xavier. 2024. 'GPAT1 Activity and Abundant Palmitic Acid Impair Insulin Suppression of Hepatic Glucose Production in Primary Mouse Hepatocytes', *J Nutr*, 154: 1109-18.

Zhang, L., D. Ma, F. Li, G. Qiu, D. Sun, and Z. Zeng. 2022. 'Lnc-PKD2-2-3/miR-328/GPAM ceRNA Network Induces Cholangiocarcinoma Proliferation, Invasion and 5-FU Chemoresistance', *Front Oncol*, 12: 871281.

Zhang, S., C. Balch, M. W. Chan, H. C. Lai, D. Matei, J. M. Schilder, P. S. Yan, T. H. Huang, and K. P. Nephew. 2008. 'Identification and characterization of ovarian cancer-initiating cells from primary human tumors', *Cancer Res*, 68: 4311-20.

Zhi, D., Y. Bai, J. Yang, S. Cui, Y. Zhao, H. Chen, and S. Zhang. 2018. 'A review on cationic lipids with different linkers for gene delivery', *Adv Colloid Interface Sci*, 253: 117-40.

Zhou, Y., H. Zhao, R. Ren, M. Zhou, J. Zhang, Z. Wu, Y. Chen, J. Lei, Y. Chen, Y. Yu, and Y. Li. 2024. 'GPAT3 is a potential therapeutic target to overcome sorafenib resistance in hepatocellular carcinoma', *Theranostics*, 14: 3470-85.

Supplemental material

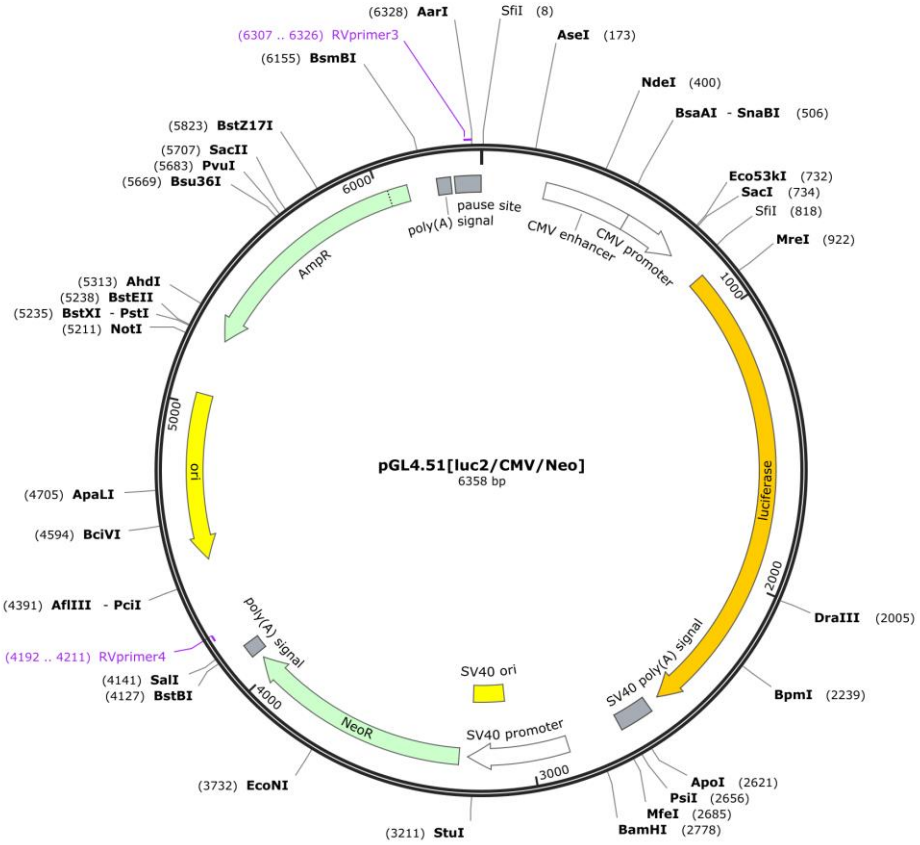

Figure S1 Map of the plasmid pGL4.51[luc2/CMV/Neo] (Promega) used to generate luciferase expressing ES-2 cells. Main elements of the plasmid and restriction sites are depicted.

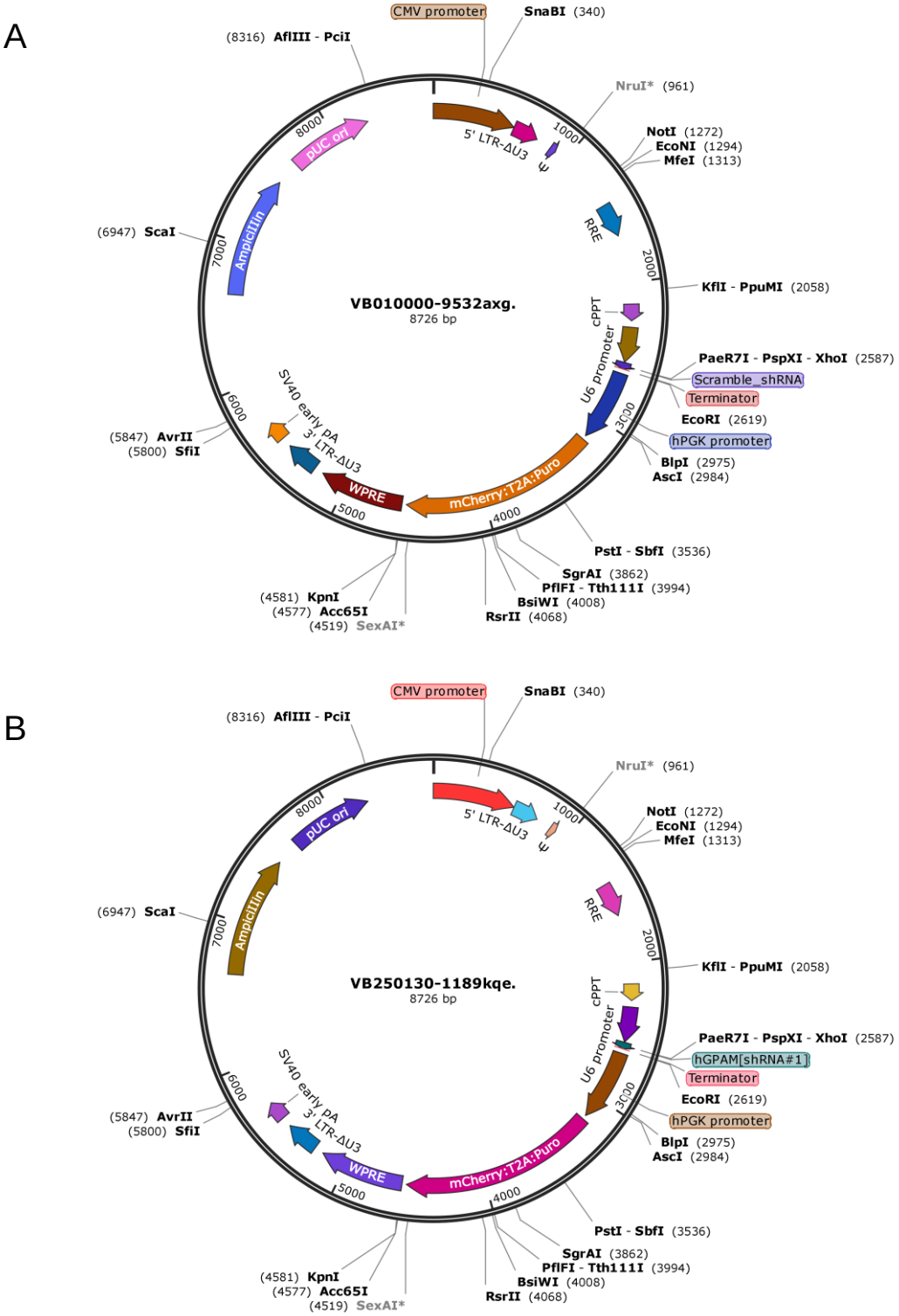

Figure S2 Map of the vectors LVC(VB010000-9532axg)-b (A), LVS(VB250130-1189kqe (B), LVS(VB250130-1186yet) (C) and LVS(VB250130-1187fxy) (D) used in the transduction of ES-2_luc cells (VectorBuilder). Main elements of the vectors and restrictions sites are shown.

C

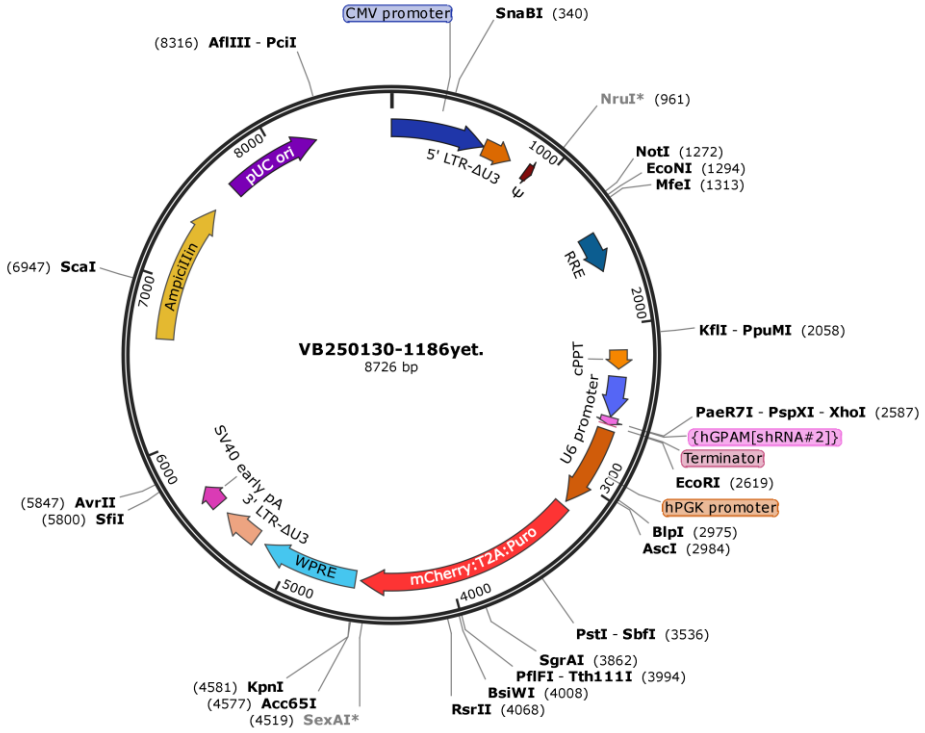

D

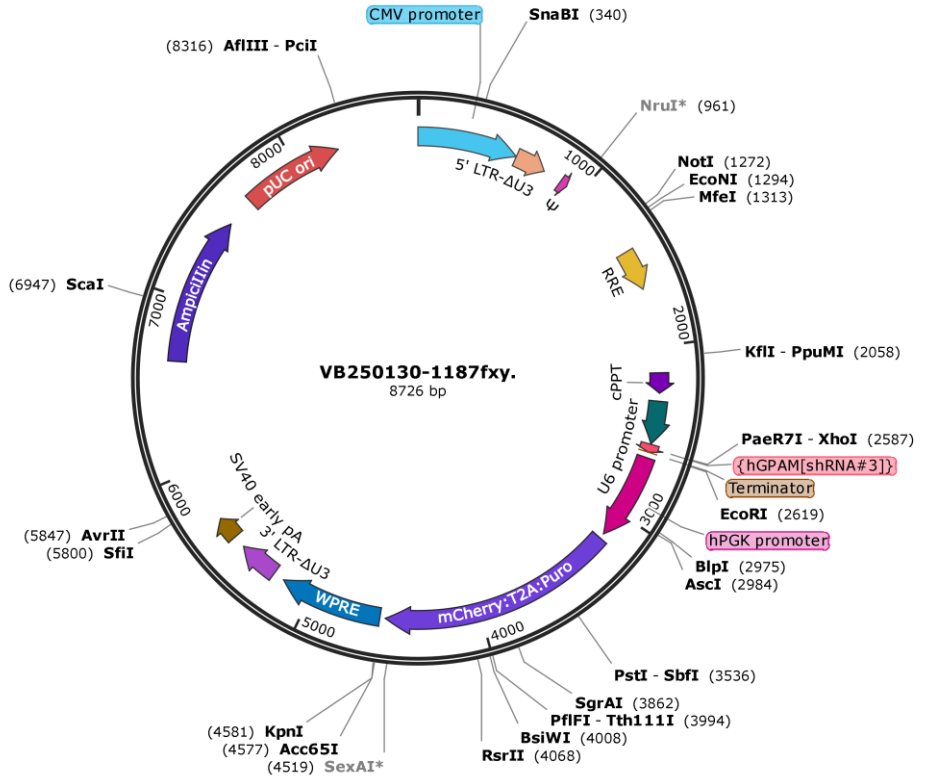

Figure S2 Continued from page II.

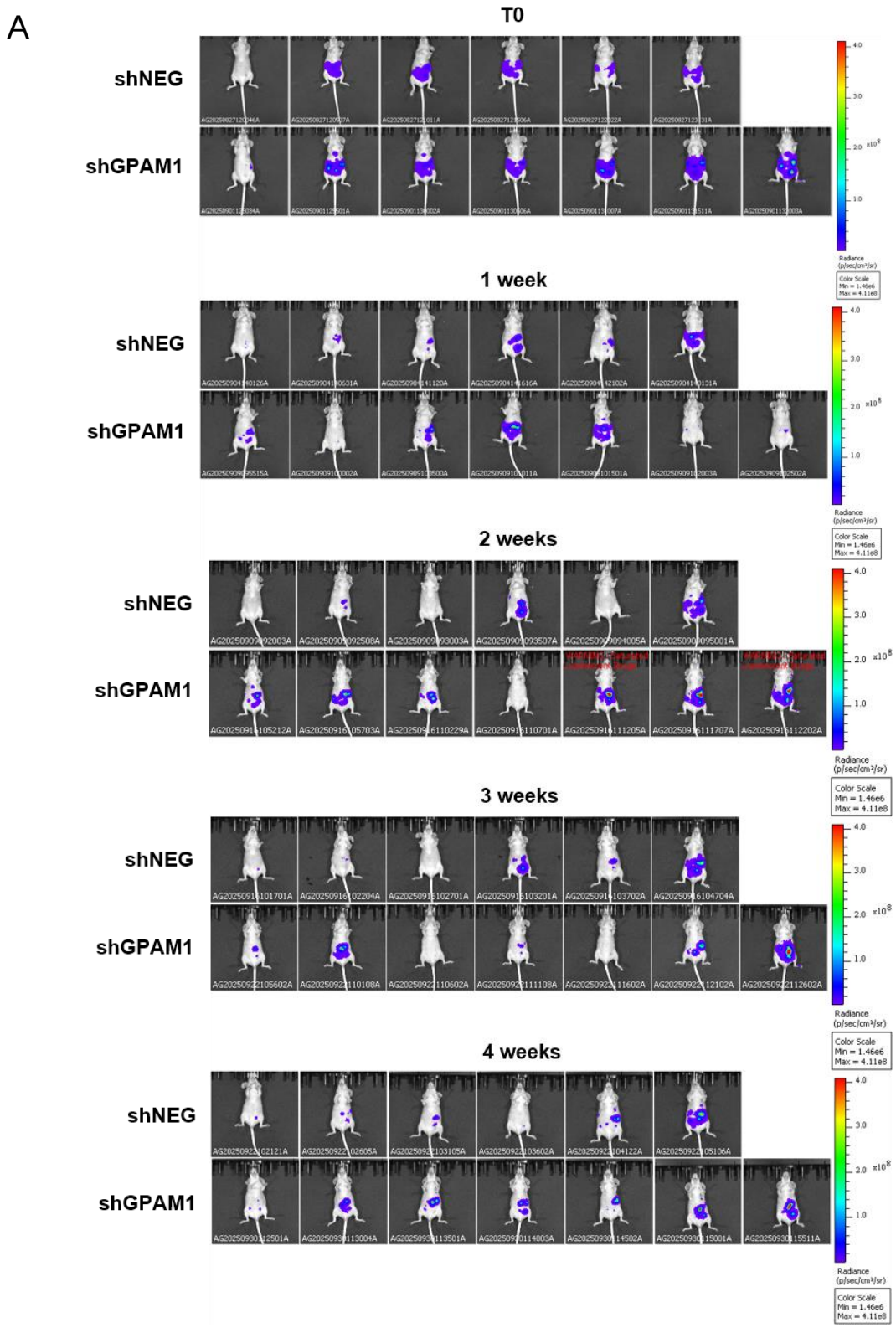

Figure S3 Imaging of the ovarian cancer cell-line xenograft (CDX) models using the IVIS Spectrum in vivo imaging system. A) In vivo imaging of individual mice injected with ES-2_luc shNEG (shNEG) or ES-2_luc shGPAM1 cells (shGPAM1) directly after the intraperitoneal injection of $5 \cdot 10^6$ cells (time 0 (T0)) and once a week over eight weeks. B) Ex vivo imaging of the collected peritoneal organs (liver, kidney, spleen, diaphragm, stomach, intestines, fat pad, omentum, lungs and pancreas) of the mice at the end of the experiment — eight weeks after injection of the cells.

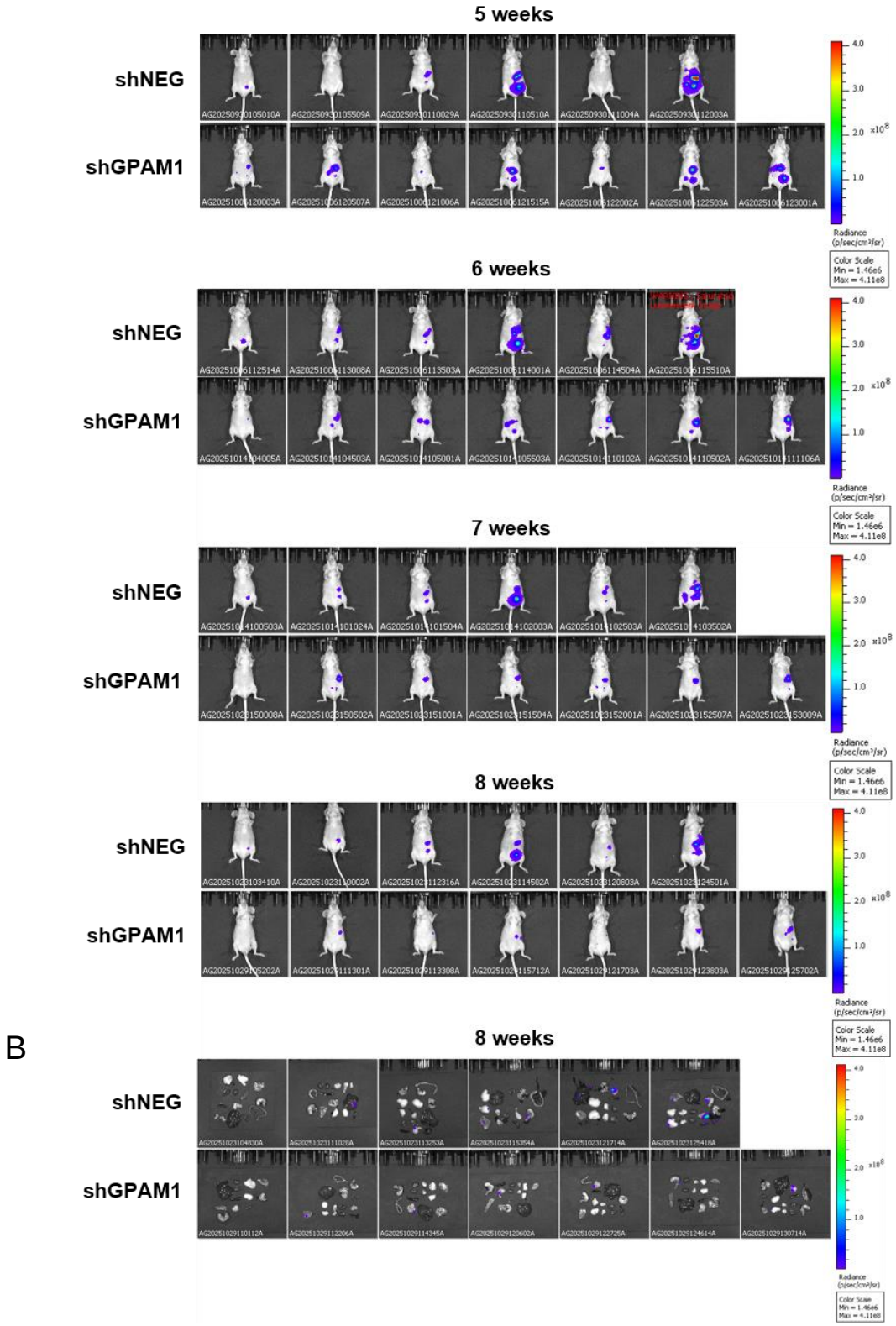

Figure S3 Continued from page IV.

The LPA-protein pull-down and peptide fragmentation fingerprinting

The first experiments failed to detect any pulled-down protein on the SDS-PAGE gel (Figure S4). Nevertheless, these experiments were useful as they provided information that could be used to optimize the conditions for subsequent experiments. On the one hand, the protein concentration of the cell lysates could be increased, since increasing protein concentration was shown to increase the intensity of the bands (Figure S4, compare lanes 0.2 cl, 0.3 cl and 0.5 cl, containing respectively 0.2, 0.3 and 0.5 µg/µl cell lysate). One the other hand, a more sensitive protein gel staining could be used. In these first experiments the SimplyBlue™ SafeStain (Thermo Fisher Scientific) was employed, which revealed no bands in the lanes in which the pulled-down samples were loaded. A more sensitive protein gel staining was found in the Pierce™ Silver Stain for Mass Spectrometry (Thermo Fisher Scientific).

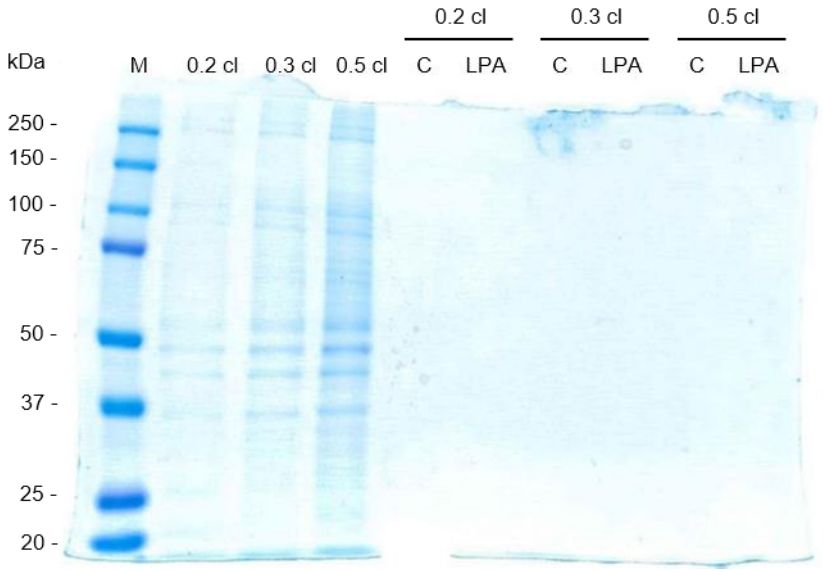

Figure S4 The preliminary experiments to establish an LPA-protein pull-down failed to detect any pulled-down protein. An SDS-PAGE was performed adding the Precision Plus Protein™ Dual Colour Standard (M) and 20 µl of different concentrations (0.2, 0.3 and 0.5 µg/µl) of cell lysate (cl), either directly into the gel (lanes 0.2 cl, 0.3 cl and 0.5 cl) or after being subjected to the LPA-protein pull-down with control agarose beads (C) and LPA-coated agarose beads (LPA) (the remaining lanes). The staining of the gel was performed with the SimplyBlue™ SafeStain.

Previously considered hints were evaluated in a new series of experiments. For this purpose, a 1 µg/µl cell lysate control and the Pierce™ Silver Stain for Mass Spectrometry were used to ensure the proteins were visualized on the gel, as well as the mouse anti-LPA antibody (Z-P200, Echelon Biosciences) in a solution to be pulled down to have a control of the LPA-protein pull-down. With this new setup, the LPA-protein pull-down was able to detect the

interaction of LPA and the anti-LPA antibody (Figure S5). With the silver stain, both the cell lysate (Figure S5, cl), as well as pulled-down proteins (Figure S5, Ab C and Ab LPA) were visualized on the gel. To validate that the visualized pulled-down proteins were indeed anti-LPA antibody, the most prominent band of the pulled-down proteins (Figure S5, rectangle 2) together with its control (Figure S5, rectangle 1) were analyzed by peptide fragmentation fingerprinting. The peptide fragmentation fingerprinting revealed the presence of a mouse antibody in both bands. More specifically, the detected protein was the immunoglobulin heavy constant gamma 2B from mouse (accession sp|P01867|IGG2B_MOUSE). This protein has a molecular weight of 44 kDa (accession sp|P01867|IGG2B_MOUSE), matching with the apparent molecular weight observed on the gel (Figure S5, rectangles 1 and 2). Although the protein was detected in the control band and the LPA band, the intensity of the control band was much lower than the intensity of the LPA band (Figure S5, compare rectangles 1 and 2), which suggests that the antibody specifically interacted with LPA. Thus, these results suggest that the LPA-protein pull-down identified the interaction of LPA with the anti-LPA antibody.

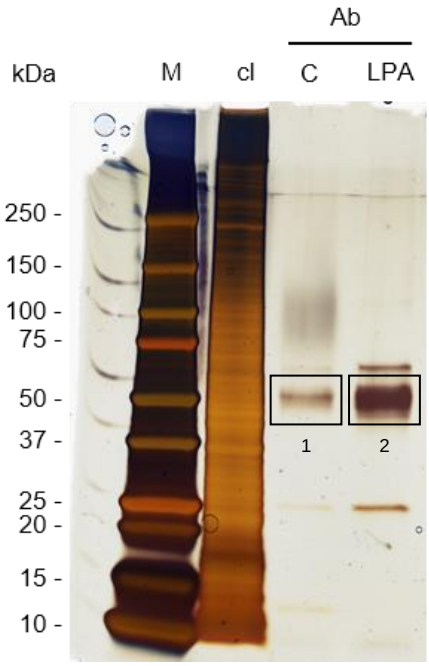

Figure S5 The LPA-protein pull-down identified specific LPA-protein interactions. Representative SDS-PAGE of three independent experiments containing the Precision Plus Protein™ Dual Colour Standard (M) and 20 µl of 1 µg/µl cell lysate (cl). An anti-LPA antibody solution (Ab) was subjected to the LPA-protein pull-down with control agarose beads (C) and LPA-coated agarose beads (LPA). The numbered rectangles mark the bands analyzed by peptide fragmentation fingerprinting. The staining of the gel was performed with the Pierce™ Silver Stain for Mass Spectrometry.

Nevertheless, the MS protein identification method presented two limitations. First, the identification of specific LPA-protein interactions was based on a ‘naked-eye’ evaluation of intensities of the bands, so if the analyzed bands had very similar intensities, a specific LPA-protein interaction would be more difficult to detect. Second, during the analysis of the peptide fragmentation fingerprint data, high levels of keratin contamination were detected, and therefore extra data curation phases were required. The most probable source of this contamination was the gel of the SDS-PAGE. Thus, the peptide fragmentation fingerprinting was not further employed.